



HAL
open science

Modulation of brain activity with low intensity focused ultrasound

Charlotte Constans

► **To cite this version:**

Charlotte Constans. Modulation of brain activity with low intensity focused ultrasound. Acoustics [physics.class-ph]. Université Sorbonne Paris Cité, 2018. English. NNT: 2018USPCC006. tel-02015339

HAL Id: tel-02015339

<https://theses.hal.science/tel-02015339>

Submitted on 12 Feb 2019

HAL is a multi-disciplinary open access archive for the deposit and dissemination of scientific research documents, whether they are published or not. The documents may come from teaching and research institutions in France or abroad, or from public or private research centers.

L'archive ouverte pluridisciplinaire **HAL**, est destinée au dépôt et à la diffusion de documents scientifiques de niveau recherche, publiés ou non, émanant des établissements d'enseignement et de recherche français ou étrangers, des laboratoires publics ou privés.



U-S-PC
Université Sorbonne
Paris Cité

ESPCI PARIS
EDUCATION SCIENCE INNOVATION

Institut Langevin
ONDES ET IMAGES

université
PARIS
DIDEROT

Inserm

Thèse de Doctorat

De l'Université Sorbonne Paris Cité

Préparée à l'Université Paris Diderot - Spécialité Acoustique Physique

Ecole doctorale 564 : Physique en Ile de France

Laboratoire : Institut Langevin

MODULATION OF BRAIN ACTIVITY WITH LOW INTENSITY FOCUSED ULTRASOUND

Présentée et soutenue publiquement le 21 septembre 2018 par

Charlotte Constans

Dirigée par Jean-François Aubry

Pr. Atef ASNACIOS, Université Paris Diderot

Dr. Jean-François AUBRY, Institut Langevin

Dr. Ayache BOUAKAZ, Université de Tours

Dr. Lori BRIDAL, LIB

Dr. Thomas DEFFIEUX, Institut Langevin

Dr. Chrit MOONEN, UMC Utrecht

Dr. Pierre POUGET, ICM

Président du jury

Directeur de thèse

Examinateur

Rapporteur

Co-encadrant

Rapporteur

Co-encadrant

Remerciements

A mon directeur de thèse, Jean-François Aubry. La qualité de ton encadrement et ta disponibilité ont largement contribué au bon déroulement de ces trois ans de thèse. Tes explications scientifiques et tes conseils, toujours pédagogiques et précis, ont été extrêmement précieux, que ce soit en physique ou en surf, et ta patience a surmonté mes nombreuses étourderies. En plus de ton investissement scientifique, tes qualités humaines et ta sympathie me laisseront un souvenir chaleureux de cette période. Je retiendrai tout particulièrement ta fierté après la rafle du trophée de babyfoot aux Houches et la séance de travail Matlab transformée en session planche à voile pendant le séminaire de labo.

Un grand merci à mon co-encadrant Pierre Pouget avec qui j'ai travaillé et discuté avec tout autant de plaisir. Il n'est pas toujours facile de garder espoir après une série de manip infructueuses, mais ton optimisme face à la jungle de données récoltées au cours de notre dernier projet restera pour moi un modèle de détermination.

Merci à Thomas pour ton aide et les conseils prodigués pour les simulations, ainsi que pour ta relecture attentive du manuscrit.

Merci à Harry, avec qui j'ai partagé les émotions des expériences sur les singes, et aux collaborateurs IRM Mathieu et Cécile.

Merci à Alexandre pour la conception des pièces mécaniques ainsi que Philippe pour l'électronique et les réparations de matériel.

Je remercie les rapporteurs Lori Bridal et Chrit Moonen pour leur relecture et leurs précieux commentaires ainsi que les examinateurs Atef Asnacios et Ayache Bouakaz.

Je retiendrai de ces trois années à Langevin une stimulation intellectuelle exceptionnelle, grâce

à la qualité de l'ensemble des travaux menés par l'équipe, mais aussi une cohésion inégalable. Merci Mickaël pour ta gestion paternelle de la famille Langevin et l'énergie que tu dépenses pour maintenir la bonne ambiance du labo.

Justine, après t'avoir copiée pour la thèse en thérapie, le virus de l'escalade, la tentative ratée du swing, je crois que le temps du sevrage est venu. Pour cette raison, je n'irai pas en Suisse ou je ne sais plus quel bled paumé en Allemagne, mais je compte sur une continuation de nos aventures festives, terrestres, alpines et marines.

Line, pour les discussions philosophiques et politiques, les retraites en abbaye, le mois sans sucre, les conférences d'histoire, les soirées tisane-tricot, les astuces de cuisine, les footings effrénés et les T-shirts à message d'amour.

Jérôme, l'étendue de tes pouvoirs dépasse toute concurrence. Pour les expéditions catacombes, le baby-flasque, les anecdotes végétales, les réparations de vélo, les anecdotes animales, les tips de geek, l'accent marseillais, ta performance à la dernière soirée Beldi III, l'accent antillais, le port du calchemise, la capacité calorifique éléphantique et encore bien d'autres talents: tu es vraiment un brave gars.

Mafalda, j'ai peur en entamant ce paragraphe de m'attirer la foudre par une phrase maladroite. En espérant donc que tu ne lises pas ces lignes, je tiens à souligner la force de ton caractère (ah bon) heureusement relevée d'un sens de l'humour et d'une gentillesse qui font de toi la Maf tant aimée et crainte simultanément, bref le soleil impitoyable du labo.

Claire, je m'incline devant la cohérence entre tes capacités festives et sportives, ton franc-parler indétronable et tes rouleaux de printemps. Mention spéciale aux week-end de trail à Chamonix, aux rhums arrangés et à tes nombreuses perles de franchise.

A Elliott, pour toutes ces discussions sportives, métaboliques et culinaires, les sessions d'escalade, et l'espoir de te voir un jour échouer dans une discipline.

Charlie, même si tu es permanent et papa, c'est quand même cool de traîner avec toi.

A Antoine et son top 3, Mai et sa patience au swing, Alexandre et ses extraterrestres odorants.

A mes co-bureau: Guillaume M., qui m'a aidée avec patience sur bon nombre de questions pratiques et numériques, Guillaume G. pour ses fous rires spontanés, Clémentine pour avoir altéré le sérieux de la pièce, Elodie la super maman. Et Olivier, tu sais en tant que médecin qu'avoir fait face sans broncher à tes posters de foot dans le bureau est une preuve d'affection en soi.

Merci à Hicham, dont la gentillesse se traduit dans toutes les attentions possibles, les cadeaux, les chocolats, mais surtout le temps dédié aux autres. Je pense notamment à ces séances de calibration à l'interféromètre, pendant lesquelles ton aide providentielle m'a sauvée d'une crise de nerf certaine.

Parce que ces trois années ont été également riches en activités et émotions en dehors du labo: merci à l'incorrigible bande de Stan, ces amis indéfectibles toujours capables des 400 coups et avec qui je partage tout. A ceux de l'X, qui au fil des soirées, vacances, colocs, considèrent mes lubies avec bienveillance derrière leurs sarcasmes. A mes amis grimpeurs, à qui je dois de merveilleuses évasions, un coaching sportif même (ou presque) pas condescendant, des pleurs et un fou-rire au pic d'une course d'alpi, une réputation de hippie et un chat temporaire.

Enfin merci à toute ma famille, en particulier mes parents, Sophie et Sibylle qui ont toujours fait l'admirable effort de lire et critiquer mes résumés scientifiques.

Abstract

The objective of this manuscript is to investigate the potential of focused ultrasound (FUS) for neuromodulation. Considering the extent of neurodegenerative diseases consequences on the society and individuals, focused ultrasound therapies appear as promising techniques combining non-invasiveness, millimetric spatial accuracy and ability to reach deep brain structures. However, efforts still need to be made to (i) amplify the effects of FUS neuromodulation by optimizing the ultrasonic parameters, (ii) understand its mechanism and (iii) control the safety of the technique. In this work, we first studied the ultrasound propagation inside the brain of rodents and non human primates with numerical tools. In addition to estimating the maximum pressure and intensity in the brain, the model gives some insight into the wave behavior in the skull cavity, exhibiting the formation of interferences and the importance of the skull geometry at several ultrasound frequencies. The ultrasonic intensity was then injected in a thermal model to estimate the thermal rise. Analyzing retrospectively published FUS studies on rodents, we show that the thermal rise is negligible in almost all cases but may reach several degrees when the duty cycle is too high. Our thermal model will therefore be a useful tool for safety control in the design of animal experiments. Understanding the mechanism underlying ultrasound neurostimulation is the key to potential treatment of brain pathologies. To evaluate physiologically the ultrasound effects at the cellular level, the activity of individual neurons was measured on macaques performing a task during ultrasonic neuromodulation. Significant alterations of the spike frequencies were measured in about 40% of the recorded neurons when ultrasonic stimulation was applied. The effect typically lasted for a few hundreds of milliseconds.

One current limitation of ultrasound neuromodulation is the duration of its effects, which had never been observed for more than 10 minutes [223] . To further increase the modulation time, new ul-

trasonic parameters were tested: by extending the sonication time with a repetitive transcranial ultrasound stimulation (rTUS), the reaction time of macaques performing a task was significantly reduced for up to 25 minutes. To image the brain activity, functional MRI was then performed after rTUS and highlighted connectivity changes between distant cerebral regions and the stimulated area. This work could have a major impact in connectomics, by non-invasively stimulating a defined region and mapping the correlation of its activity with the entire brain.

Finally, the advantages of ultrasound neurostimulation were combined with the efficiency of a neuroactive agent. Using microbubbles and ultrasound, the blood brain barrier was opened locally and reversibly in the visual cortex of anesthetized macaques to allow the permeation of an inhibitory neurotransmitter (GABA, γ -Aminobutyric acid) in the brain. The amplitude of the EEG response of the visual cortex to stimuli (white flashes) decreased after GABA injection, demonstrating the feasibility of delivering drugs non-invasively and locally to any brain region.

Overall, ultrasound parameters were optimized with both numerical tools and *in vivo* experiments to amplify neuromodulation effects while controlling the safety, with the goal of therapeutic applications and new tools for connectivity studies.

Keywords: Ultrasound, neuromodulation, neurostimulation, blood-brain barrier opening, inhibition, GABA, numerical simulations, k-wave.

Résumé

L'objectif de cette thèse est d'évaluer le potentiel des ultrasons focalisés pour neuromoduler. Etant donné l'impact des maladies neurodégénératives sur la société, les thérapies par ultrasons focalisés apparaissent comme des techniques prometteuses combinant non invasivité, précision spatiale millimétrique et capacité d'atteindre les structures profondes du cerveau. Cependant, des travaux sont encore nécessaires pour (i) amplifier les effets de la neuromodulation en optimisant les paramètres ultrasonores, (ii) comprendre le mécanisme sous-jacent et (iii) contrôler la sûreté de la technique. La propagation des ultrasons dans le cerveau de rongeurs et de primates non humains a tout d'abord été étudiée numériquement. Le modèle estime non seulement la pression et l'intensité acoustique maximale dans le cerveau, mais aussi la répartition spatiale des ondes dans la boîte crânienne, mettant ainsi en évidence la formation d'interférences et l'importance de la géométrie du crâne aux différentes fréquences ultrasonores utilisées. Les cartes d'intensité ultrasonore sont ensuite injectées dans un code thermique pour estimer l'élévation de température. En analysant rétrospectivement des études de neurostimulation par ultrasons chez les rongeurs publiées précédemment, nous montrons que l'échauffement est négligeable dans la plupart des cas mais peut atteindre plusieurs degrés si le rapport cyclique est trop élevé. Le code thermique sera ainsi un outil utile pour le contrôle de sûreté lors de la conception d'expérimentations animales.

Comprendre les mécanismes en jeu dans la neurostimulation par ultrasons est la clé qui permettra l'élaboration de traitements des pathologies du cerveau. Afin d'évaluer physiologiquement les effets des ultrasons à l'échelle cellulaire, l'activité de neurones individuels a été mesurée sur des macaques exécutant une tâche visuelle pendant une neuromodulation ultrasonore. Des altérations significatives de la fréquence de décharge neuronale ont été observées dans environ 40% des neurones enregistrés lorsque la stimulation ultrasonore était appliquée. L'effet dure pendant quelques

centaines de millisecondes.

A l'heure actuelle, une des limitations de la neuromodulation par ultrasons est la durée des effets, qui n'avaient jamais été observés pendant plus de 10 minutes [223] . Pour augmenter le temps de modulation, de nouveaux paramètres ultrasonores ont été testés: en allongeant le temps de tir avec une stimulation transcranienne répétée, le temps de réaction des macaques exécutant une tâche a été modifié significativement, jusqu'à 25 minutes après la stimulation. Afin d'imager l'activité du cerveau, l'IRM fonctionnelle a été ensuite employée, faisant ressortir les changements de connectivité entre des régions du cerveau éloignées et l'aire stimulée. Ce travail pourrait avoir un impact majeur en connectomique, par la stimulation non invasive d'une région définie et la cartographie de la corrélation de son activité avec le reste du cerveau.

Enfin, les avantages de la neurostimulation par ultrasons ont été combinés avec l'efficacité d'un agent neuroactif. En utilisant des microbulles et les ultrasons, la barrière hémato-encéphalique a été ouverte localement et réversiblement dans le cortex visuel de macaques anesthésiés pour permettre le passage d'un neurotransmetteur inhibiteur (GABA, acide γ -Aminobutyrique) dans le cerveau. L'amplitude des réponses EEG du cortex visuel à des stimuli (flashes lumineux) diminue après l'injection de GABA, démontrant la faisabilité de la délivrance locale et non invasive de neuromodulateurs dans toute région du cerveau.

Ainsi, les paramètres ultrasonores ont été optimisés grâce aux simulations numériques et à des expériences *in vivo* pour amplifier les effets de neuromodulation tout en contrôlant les effets indésirables, avec l'objectif de se diriger vers des applications thérapeutiques et proposer de nouveaux outils pour des études de connectivité cérébrale.

Mots clés: Ultrasons, neuromodulation, neurostimulation, ouverture de barrière hémato-encéphalique, inhibition, GABA, simulations numériques, k-wave.

Contents

List of Figures	15
List of Tables	19
Acronyms	21
1 General Introduction	25
1.1 Focused Ultrasound Neuromodulation	25
1.1.1 Mechanism Hypothesis	26
1.2 Potential applications: neurodegenerative diseases and neurological disorders . . .	27
1.2.1 Global health issue	27
1.2.2 Most frequent diseases and current treatments	28
1.2.3 Current and potential treatments with ultrasound	29
1.2.4 Deep Brain Stimulation	32
1.2.5 Transcranial Magnetic Stimulation	33
1.2.6 Transcranial Direct Current Stimulation	33
1.2.7 Competitive Edges of Focused Ultrasound Neuromodulation	33
1.3 Conclusion and thesis objectives	34
2 Numerical estimation of temperature elevation during ultrasonic neurostimulation	35
2.1 Introduction	35
2.2 Methods	36
2.2.1 Simulations	36

2.2.2	Model validation	40
2.2.3	Measurements of temperature rise in mouse	42
2.3	Results	43
2.3.1	Simulations	43
2.3.2	Measurements of temperature rise in mouse	45
2.4	Discussion	46
2.5	Conclusion	51
3	Towards a multifrequency ultrasonic neurostimulation	53
3.1	Introduction	53
3.2	Materials and methods	54
3.2.1	Transducer	54
3.2.2	Numerical simulations	55
3.3	Results	57
3.4	Discussion	62
3.5	Conclusion	65
4	Transcranial ultrasonic stimulation modulates single-neuron discharge in macaques performing an antisaccade task	67
4.1	Introduction	67
4.2	Materials and methods	68
4.3	Results	74
4.4	Discussion and conclusion	79
5	Repetitive Transcranial Focused Ultrasound Stimulation	83
5.1	Introduction	83
5.2	Materials and Methods	84
5.3	Results	88
5.4	Discussion	91
5.5	Conclusion	91

6 Spatially specific and non-specific effects of focused ultrasound neuromodulation on BOLD responses in primates	93
6.1 Introduction	93
6.2 Materials and Methods	94
6.3 Results	97
6.4 Discussion and conclusion	99
7 GABA-induced neuromodulation in non-human primates	101
7.1 Introduction	101
7.2 Materials and methods	102
7.3 Results	105
7.4 Discussion	111
7.5 Conclusion	114
8 Conclusion and perspectives	117
Bibliography	119
Résumé de thèse	143
Scientific output	163

List of Figures

1.1	A schematic diagram of the endothelial cells that form the blood brain barrier (BBB) and their associations with the perivascular endfeet of astrocytes.	31
1.2	DBS implantation surgery	32
2.1	Coronal view of absorption maps at 500 kHz and 1.4 MHz	37
2.2	Model validation: pressure profile and temperature rise with k-Wave and HIFU simulator	41
2.3	Simulated peak pressure fields in rat brain at 0.32 kHz and 1.9 MHz.	44
2.4	Estimated temperature rise at 320 kHz	45
2.5	Estimated temperature rise at 1.9 MHz	45
2.6	Temperature measured in a mouse head skin with a thermocouple during two different sequences of ultrasonic neuromodulation	46
2.7	Temperature at the end of a 20s sonication at 1.9 MHz	47
2.8	Estimated temperature rise at 1.9 MHz, with the same parameters as in Kamimura et al, except for the duty cycles	50
3.1	Schematic review of maximum pressures applied in brain to achieve neuromodulation.	54
3.2	Frequency analysis for the transducer.	58
3.3	Peak negative pressure and peak positive pressure measured behind a monkey skull flap with respect to output voltage for one of the five tested positions.	58
3.4	Maximum positive pressure over time in rat head and in free water at every frequency, in decibels.	59

3.5	Sound speed field for simulations in monkey skull flap and comparison between measured and simulated transmission as a function of frequency	60
3.6	Maximum positive pressure over time in female monkey L, male monkey Y and free water.	62
3.7	Schematic review of maximum pressures applied in brain to achieve neuromodulation.	63
4.1	FUS and electrophysiological recording set-up	72
4.2	Peak negative pressure (MPa) in the brains of monkey Y and L from simulations .	75
4.3	Average recorded spikes per seconds with or without single pulse FUS.	76
4.4	Modulation while comparing FUS and control trials ($p < 0.01$) in the population of recorded neurons in the two animals.	78
4.5	Spike waveforms with and without FUS.	80
4.6	Height/Width ratio of spike waveforms with and without FUS for all neurons recorded in monkey L and monkey Y respectively.	81
5.1	rTUS set-up	85
5.2	rTUS stimulation sites and neuronavigation.	86
5.3	Mean saccadic latencies (in ms), separately for FEF and SEF conditions and direction of eye movement (ipsilateral and contralateral movement).	89
5.4	Mean saccadic latencies (in ms) for antisaccades, separately for control regions conditions (visual or motor cortex) and direction of eye movement (ipsilateral and contralateral movement).	90
5.5	Thermal rise during rTUS	91
6.1	Functional connectivity to preSMA after preSMA stimulation	97
6.2	Functional connectivity to V1 after preSMA stimulation	98
7.1	MRI assessment of BBB opening.	106
7.2	Timeline of the experiments.	107
7.3	Mean VEP recordings for each run for several sessions.	108
7.4	Comparison between the visual response before and after neuromodulation by BBB opening and GABA injection for the two animals with a 4 mg/kg GABA dose. . .	109

7.5	VEPs decrease of amplitude	110
7.6	Harmonics and broadband level during BBB opening, session with monkey A at 5 mg/kg.	111
7.7	Spectral UCA response before and after UCA injection, session Monkey A 5mg/kg.	112
7.8	Proportion of the inhibitory effects due to neuromodulation (ultrasound only), BBB opening (ultrasound + UCA) and GABA (after BBB opening and GABA injection).	115
8.1	Les principales maladies neurodégénératives en France	144
8.2	Estimation de l'élévation de température à 1.9 MHz	149
8.3	Mesure de température dans la peau d'une souris au niveau du crâne durant deux séquences ultrasonores différentes: stimulation forte (Kamimura et al) et faible (Ye et al)	150
8.4	Résultats de simulations chez le rat, le singe mâle et le singe femelle	152
8.5	Fréquence de décharge neuronale avec ou sans simulation ultrasonore.	153
8.6	Moyenne des temps de latence (en ms), dans les conditions SEF et FEF et en fonction de la direction du mouvement (ipsilatéral et contralatéral)	155
8.7	Carte de connectivité par rapport à la preSMA	156
8.8	Moyenne des réponses visuelles aux différents instants de la session: référence, ultrasons seuls, ultrasons + ACU, ouverture de BHE et injection de GABA.	158
8.9	Décroissance de l'amplitude des réponses visuelles.	159

List of Tables

2.1	Parameters and results in brain and at the focal spot.	37
2.2	Estimated pressures in water based on the reported data.	39
2.3	Tissue properties for simulations	41
2.4	Validation of the numerical model with a comparison with HIFU simulator in the 0.5 – 2 MHz range: results.	41
2.5	Parameters and results of thermal simulations.	43
2.6	Estimated and measured thermal rise in the mouse skin head	46
2.7	Results for temperature and thermal dose with varied duty cycles, at 1.9 MHz, 1.6 MPa in the brain	50
2.8	Reported threshold values of thermal dose for thermal necrosis.	50
3.1	Measured and numerical results for peak positive pressures and pressure gains in rat and monkey	57
3.2	Volume of brain affected by ultrasound and standing wave ratio	59
3.3	Optimal acoustic parameters	61
3.4	Measured and simulated transmission values	61
4.1	Acoustic parameters	73
4.2	CT parameters	73
4.3	Estimations of peak pressure in monkeys' brains	74
7.1	Maximum relative augmentation and time above the efficiency threshold for the subharmonic.	112

8.1 Paramètres et résultats dans le cerveau et au point focal. 149

Acronyms

I_{SPPA} Intensity Spatial Peak Pulse Average. 104

I_{SPTA} Intensity Spatial Peak Time Average. 104

μ **CT** micro-computed tomography. 36, 55

AD Alzheimer's disease. 27

AS antisaccade. 88

BBB blood brain barrier. 15, 29, 31, 101

BLS Bilayer Sonophore. 26

BOLD blood-oxygen-level dependent. 93

CEM Cumulative equivalent minutes at 43°C. 48

CI confidence interval. 76

CNS Central Nervous System. 27, 29

CT computed tomography. 55

DBS deep brain stimulation. 28, 31

ET essential tremor. 27

FDA Food and Drug Administration. 28, 31

fMRI functional Magnetic Resonance Imaging. 91, 93

FUS Focused Ultrasound. 33

GABA γ -Aminobutyric acid. 101

Gd Gadolinium. 104

GPI globus pallidus internus. 31

HH Hodgkin-Huxley. 26

HIFU High Intensity Focused Ultrasound. 40

KZK Khokhlov-Zabolotskaya-Kuznetsov. 40

MI mechanical index. 84

MRCA MR contrast agent. 104

NICE Neuronal intramembrane cavitation excitation. 26

OCD Obsessive-compulsive disorder. 27, 31

PCD passive cavitation detector. 103

PD Parkinson's disease. 27, 31

PNP peak negative pressure. 68

PRF pulse repetition frequency. 84

ROI region of interest. 95

rTMS repetitive transcranial magnetic stimulation. 90

rTUS repetitive transcranial ultrasonic stimulation. 83

SCN suprachiasmatic nucleus. 48

SOA stimulus onset asynchrony. 106

SSEP somatosensory evoked potential. 33

STN subthalamic nucleus. 31

TD thermal dose. 49

tDCS Transcranial Direct Current Stimulation. 29, 33

TMS Transcranial Magnetic Stimulation. 28, 32

UCA Ultrasound Contrast Agent. 101

V_{PP} peak to peak voltage. 68

VEP visual evoked potentials. 104, 105

Chapter 1

General Introduction

1.1 Focused Ultrasound Neuromodulation

Ultrasound has been found to interact with neuronal tissues relatively recently. We know now that above a certain intensity threshold that depends on the cells type and the ultrasound frequency, ultrasonic waves are able to induce neuronal discharge [206]. In the 50s and 60s, Fry et al [57, 11, 54, 58, 59, 61] were pioneers in inducing reversible changes on nervous structures: they altered the activity of an excised crayfish ventral nerve cord and the visual nervous system of a cat. Lele et al [116] induced similar effects on peripheral nerves of cat, monkey and humans. More recently, reversible effects on animals' central nervous system were elicited with reduced ultrasound dosages, giving a new momentum to ultrasonic neuromodulation. Tyler and his group [114, 206] were the first to elicit movements in anesthetized rodents, with reported pressure amplitudes as low as 50 kPa in the brain, without observing any adverse effect on the stimulated tissue [204]. In 2012, Yang et al [221] demonstrated that low intensity focused ultrasound reduced extracellular γ -Aminobutyric acid (GABA) levels in rats. In 2013, Younan et al [227] reproduced Tyler's motor elicitation results and reported a pressure threshold below which no elicitation could be seen. Trials were also broadened to larger species. Yoo et al. stimulated the somatosensory and visual areas of anesthetized rabbit [224] and sheep [111] under MRI guidance, with electrophysiological recordings. Pouget and colleagues reported behavioral changes [36] and single neuron discharges [215] during antisaccade tasks after transcranial ultrasound application in the frontal eye field of

awake monkeys. In human volunteers, somatosensory sensations were modulated by Legon et al [114] and elicited by Lee et al [108].

1.1.1 Mechanism Hypothesis

The exact mechanism for neuronal ultrasonic stimulation remains unknown, however several models have been proposed to explain the ultrasonic neuromodulation effects and are explained in detail in Sassaroli *et al.* review [183]. They build on the Hodgkin-Huxley (HH) model [75], commonly accepted for the description of nerve pulses. Today, it is generally thought that thermal effects are unlikely to play a role in the process when compared with the mechanical effects such as radiation pressure and cavitation [114, 109]. Furthermore, the role of ionic channels was experimentally assessed: the activation of voltage-gated sodium and calcium channels by low-intensity, low-frequency ultrasound was demonstrated experimentally by Tyler et al [207]. In parallel, Ibsen et al [85] highlighted experimentally the role of mechanotransduction channels in the response of *C. elegans* to ultrasound stimulation.

Soliton model The soliton model [74] considers the action potential as a propagating density pulse (soliton). It is based on thermodynamics and phase behavior of the lipids in the cell membrane, which are not taken into account in the HH model despite evidence of mechanical forces and isentropic behavior of the nerve pulse (reversible temperature changes during the voltage change). As the elastic constants are subject to modulation under mechanical constraints, this model explains how external mechanical forces could in principle initiate an action potential.

Flexoelectric model The flexoelectric model [164] hypothesizes that the mechanical bending induced by the ultrasound on the membrane leads to a change in its electric potential proportional to the change of curvature dC : $dV_{flexo} = \frac{f_{flexo}^D}{\epsilon_0} dC$ where f_{flexo}^D is the direct flexoelectric coefficient. The reverse effect (a voltage variation induces a change of curvature) may qualitatively explain the mechanical effects observed during an action potential propagation. However, no equation can yet predict the generation and propagation of the action potential by sole changing of the local membrane curvature through the direct flexoelectric effect.

Neuronal intramembrane cavitation excitation (NICE) Plaksin *et al.* [168] proposed an intramembrane cavitation model, based on the HH model and the Bilayer Sonophore (BLS) model [103]. The BLS model predicts that under ultrasound, the intramembrane space between the two leaflets of the lipid membrane undergoes expansions and contractions. At sufficient high intensity and low frequency, dissolved gas accumulates in hydrophobic parts, leading to the formation of nanobubbles (intramembrane cavitation). These nanobubbles oscillations cause changes in the local curvature of the membrane, generating an alternative current flowing across the lipid membrane. With this additional term, the HH equation admits solutions describing generation of the action potential by ultrasound.

Finding the mechanism underlying ultrasound-induced neuronal discharge is still a key axis of research in the field of neuromodulation. Besides, different types of neurons are reported to respond differently to the wave [167], the duty cycle being the selective parameter. Such a property could be used in the future to activate specifically excitatory or inhibitory neurons in the brain.

1.2 Potential applications: neurodegenerative diseases and neurological disorders

1.2.1 Global health issue

Neuronal pathologies are numerous and have a wide prevalence. They encompass neurodegenerative diseases, psychiatric disorders and epilepsy. Neurodegenerative diseases are characterized by the premature and progressive death of neurons in different regions of the Central Nervous System (CNS). For the most part, their causes are unknown, although some genetic and environmental risk factors have been identified. These debilitating diseases concern an increasing number of people due to population aging: 16% of European population is over 65 today, but the proportion is expected to reach 25% by 2030. Today in France, more than 1 million people are impacted: 850.000 individuals suffer from Alzheimer's disease (AD) type dementia, 300.000 from essential tremor (ET), 150.000 from Parkinson's disease (PD) and 85.000 from multiple sclerosis. More generally, neurological and psychiatric disorders affect almost a billion people world-wide, concerning all ages. Epilepsy, characterized by the occurrence of recurrent seizures (excessive activity

of a group of neurons) affects 0.5% to 1% of the world's population, and about 430.000 people in France. Depression, the most common mental illness, concerns 5 to 15% of the French population [39]. Obsessive-compulsive disorder (OCD), which manifests itself in obsessions and repeated behaviours, affect 2 to 3% of the population [40].

1.2.2 Most frequent diseases and current treatments

Alzheimer's disease AD is characterized by the abnormal accumulation of β -amyloid peptides outside nerve cells, forming amyloid plaques. In parallel, TAU proteins accumulate in neurons and cause their degeneration. There is actually no cure for AD, although some drugs can slow down the progression by regulating the neurotransmitters activity (five drugs have been approved by the Food and Drug Administration (FDA)). Understanding AD cause is a key research axis to find a cure or prevent the disease.

Parkinson's disease In PD, a protein called α -synuclein accumulates and forms Lewis bodies in the substantia nigra, located in the midbrain. These bodies cause the degeneration of dopaminergic neurons, leading to a lack of dopamine. By the time symptoms (mainly motor disorders) appear, about 80% of these neurons have already died. Similarly to AD, the cause of PD is not known although genetic and environmental risk factors have been identified. Medication (dopamine supply) help compensate the symptoms, but there is no cure for PD. Neuromodulation can also improve the patient condition: although its mechanism is not understood, thalamic deep brain stimulation (DBS) reduces the motor symptoms [18, 119]. However, given the procedure's invasiveness, DBS is used only in severe cases where drugs are ineffective.

Essential Tremor ET is the most common motor disorder, affecting 1 person out of 200 of all ages with a large genetic contribution. ET is not a deadly disease but is strongly invalidating. Its symptoms (head and hands shaking) resemble those of PD although the mechanisms are different: ET appears to result from a cerebellum dysfunction [125], however little is known about the disease's pathophysiology. Drugs, such as beta-blockers and anti-epileptics, were discovered to reduce some of the symptoms in some patients. Neuromodulation (DBS [102], Transcranial Magnetic Stimulation (TMS) [66]) was also found to reduce the symptoms [119].

Epilepsy Epilepsy can be symptomatic (caused by structural disorders due to injury or abnormal cortex organization) or idiopathic (caused by genetic singularities). Anti-epileptic drugs help prevent seizures by decreasing neuronal activity in about 70% of cases, but they are not curative. Surgical removal of the epileptic area can also be considered, when it does not come with major neurological complications. Neurostimulation (DBS [51], TMS [199]) has been shown to reduce the amount of seizures in some patients. DBS and TMS techniques will be described in more details in the next section.

Depression Depression is strongly correlated to environmental and genetic factors. Its mechanism implies neurotransmitters imbalance [97] and particularly an overproduction of cortisol, the stress hormone [106]. Psychotherapy can be efficient for moderate to severe (in association with antidepressants) cases [177]. Antidepressants unfortunately come with strong adverse effects (nausea, insomnia, somnolence, fatigue, sexual dysfunction, weight gain) [158]. Finally, electroconvulsive therapy [10, 163] and neurostimulation (DBS [136], TMS [65], Transcranial Direct Current Stimulation (tDCS) [53]) are used for treatment-resistant depression.

Obsessive-compulsive disorders Some OCD syndromes suggest a cortico-striatal-thalamic-cortical dysfunction and impaired inhibition, consistently with structural imaging findings (decreased volume or increased grey matter density in the mentioned region [196]). Some other regions might also be involved in OCD, such as temporal cortex and amygdala [78, 198]. Currently, cognitive-behavioural psychotherapy treatments [180], and / or serotonergic antidepressants [89] can improve two-thirds of patients, but the severe forms are resistant to these treatments. Neurostimulation (DBS [155], TMS [68], tDCS [13]) can then be used to treat OCD patients.

1.2.3 Current and potential treatments with ultrasound

Thermal ablation With sufficient power, ultrasound can be transcranially applied to the brain to thermally ablate tissue [60]. The technique is already used clinically in the case of ET disease, where the nerve cells that cause the tremor, located in the thalamus, are targeted under MRI-guidance [46, 121, 49]. Patients are awake, allowing real-time feedback control through clinical assessments during the procedure.

Drug delivery across the blood brain barrier The BBB is a semi-permeable membrane that separates the circulating blood from the CNS [2, 144, 73]. It naturally prevents large molecules (more than 400-500 Da) from diffusing through the capillary walls of the brain. Endothelial cells play the role of filtering agents via their tight junctions around the brain vasculature walls. More specifically, the BBB blocks hydrophilic molecules while allowing the passage of water, some gases and small lipophilic particles via passive diffusion. Elements that are necessary to the brain function such as glucose and amino-acids are also selectively transported across the BBB. Some other lipophilic substrates, unwanted in the brain, are broken down by specific enzymes in the endothelial cells (endogenous substrates such as hormones and neurotransmitters, or exogenous substrates such as drugs and neurotoxic compounds).

Thus, while protecting the brain from numerous toxic agents, it also prevents potential medication for brain diseases to being administered through the blood [7]. To avoid the invasiveness of intracerebral injection, several chemical solutions were found to deliver drugs to the CNS: adding hydrophobic groups to molecules (e.g.: the lipophilic form of morphine is heroin) or creating amino-acids or glucose-like drugs (e.g.: the anticancer agent melphalan is a nitrogen-mustard derivate of phenylalanine). These methods, however, are limited to molecules smaller than 450 Da [159, 1]. It has been found that some endogenous chemicals (neurotransmitters, hormones and inflammatory mediators) can induce a brief opening of the tight junctions in the BBB [70]. Consequently, it was assumed that the brain tolerates well transient BBB opening. Researchers therefore explored ways of deliberately opening the BBB to deliver drugs that could not be chemically modified. Osmotic opening, induced by injecting a hypertonic solution such as mannitol in the carotid artery, has been proven successful in increasing the size threshold for passive diffusion by shrinking the endothelial cells and opening the tight junctions [71]. Another method, biochemical BBB disruption, consists in injecting leukotriene C4 instead of a hypertonic solution [27]. Only the brain tumor capillaries are sensitive to this vasoactive agent, allowing a selective opening of the tight junctions of tumoral areas while leaving healthy tissue intact. Although these chemical methods show efficiency in some cases, they either require developing new permeable agents, which is not always possible or desirable, or they induce a global BBB opening for several hours under general anesthesia related with adverse effects. In most cases, the drug is not only delivered in the area that is concerned with the treatment, but in the entire brain. Ultrasound-induced BBB opening is a relatively new

technique [84] that offers the potential of non-invasive, targeted, reversible delivery of all types of molecules. The main research axes are currently applications for AD [92, 115], PD [120], depression [210], OCD [94], and glioblastoma [123, 220].

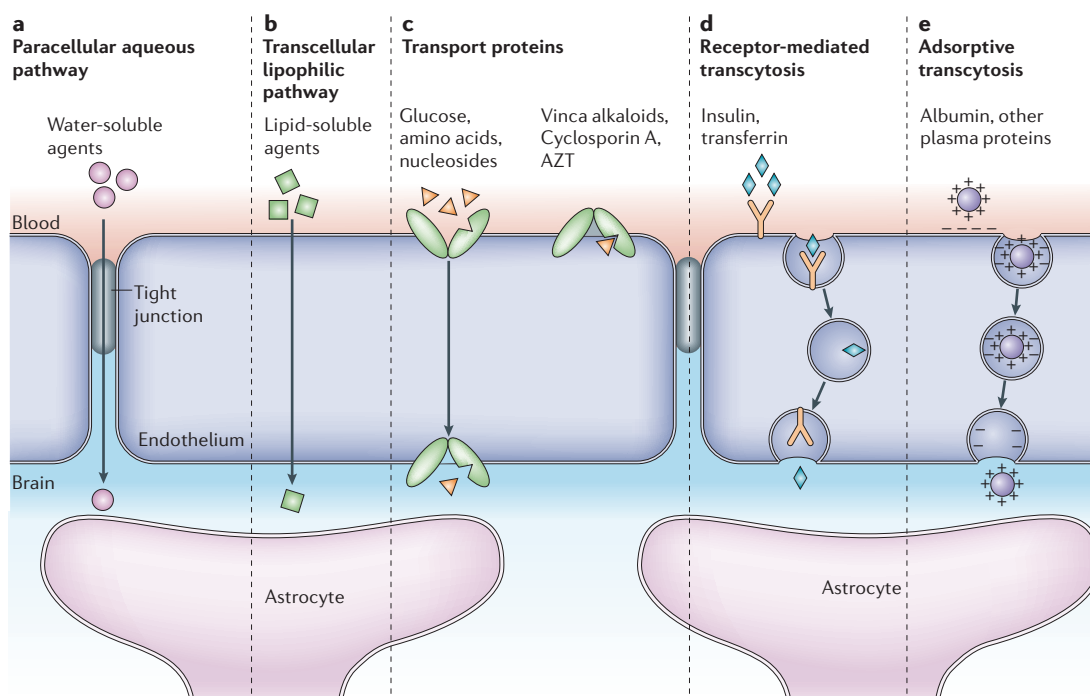


Figure 1.1: A schematic diagram of the endothelial cells that form the BBB and their associations with the perivascular endfeet of astrocytes. The main routes for molecular traffic across the BBB are shown. a — Normally, the tight junctions severely restrict penetration of water-soluble compounds, including polar drugs. b — However, the large surface area of the lipid membranes of the endothelium offers an effective diffusive route for lipid-soluble agents. c — The endothelium contains transport proteins (carriers) for glucose, amino acids, purine bases, nucleosides, choline and other substances. Some transporters are energy-dependent (for example, P-glycoprotein) and act as efflux transporters. AZT, azidothymidine. d — Certain proteins, such as insulin and transferrin, are taken up by specific receptor-mediated endocytosis and transcytosis. e — Native plasma proteins such as albumin are poorly transported, but cationization can increase their uptake by adsorptive-mediated endocytosis and transcytosis. Drug delivery across the brain endothelium depends on making use of pathways b–e; most CNS drugs enter via route b. Taken from Abbott *et al.* [3]

1.2.4 Deep Brain Stimulation

DBS relies on electrical impulses sent by the electrodes of a neurostimulator directly implanted in specific targets of the brain. This invasive treatment requires a neurosurgical procedure to place the system in the body. Electrode leads are implanted in one or two nuclei of the brain. They are linked to the implanted pulse generator, subcutaneously placed below the clavicle, via extension wires tunneled underneath the skin. A ~ 14 mm-diameter hole is drilled into the skull and the electrodes are inserted stereotactically (figure 1.2). The placement is optimized using feedback from the patient under local anesthesia, or with MRI guidance under general anesthesia [69]. Despite the invasiveness of the technique, the treatment has been applied for decades on a number of neurodegenerative diseases. The US FDA approved thalamic DBS in 1997 for essential tremor and PD-related tremor [14, 179]. In 2003, subthalamic nucleus (STN) and globus pallidus internus (GPI) DBS for PD were authorized. DBS has also proved successful in cases of ET [102], epilepsy [51], segmental dystonia, OCD, Tourette syndrome, depression, epilepsy, headache, pain, vegetative state, addiction, obesity, dementia, and stroke recovery [76, 51, 90, 188]. The mechanism underlying its therapeutic efficacy remains unclear, although a possible explanation is the inhibition of the basal ganglia overactivity in PD case, leading to a decrease of the motor symptoms [8]. Risks include intracranial hemorrhage (0%-10%), stroke (0%-2%), infection (0%-



Figure 1.2: DBS implantation surgery (*from Wikipedia*)

15%), lead erosion without infection (1%-2.5%), lead fracture (0%-15%), lead migration (0%-19%), and death (0%-4.4%) [18]. Hardware infection is the most common reported serious surgical complication.

1.2.5 Transcranial Magnetic Stimulation

During TMS, a coil near the patient’s head generates a changing magnetic field that induces an electric current in the brain via electromagnetic induction. High frequency repetitive TMS (10 - 20 Hz) is used for the treatment of depression [63] (FDA approval was granted in 2008) and studied for other brain diseases such as pain, movement disorders, stroke, amyotrophic lateral sclerosis, multiple sclerosis, epilepsy, consciousness disorders, tinnitus, depression, anxiety disorders, obsessive-compulsive disorder, schizophrenia, craving/addiction, and conversion [113, 135, 124]. For depression treatment, the target is often the dorsolateral prefrontal cortex (DPC). Activation of the DPC by TMS leads to the suppression of hypothalamic overactivity [41]. Adverse effects are limited and related to the discomfort of the procedure (pain, syncope, transient cognitive effects).

1.2.6 Transcranial Direct Current Stimulation

tDCS consists in the application of constant low intensity electric current to cortical areas via electrodes placed on the head. As opposed to TMS and DBS, it does not induce neuronal firing but rather modulates spontaneous neuronal network activity [20, 154, 173]. Its application is investigated for depression [157], headache, craving, PD [154]. Safety concerns are limited to skin irritation and tissue heating.

1.2.7 Competitive Edges of Focused Ultrasound Neuromodulation

Today, tDCS, TMS and DBS are the most often employed techniques to treat neurological diseases. These methods come with major drawbacks: the low spatial resolution of tDCS [20, 153], and TMS [124, 212, 214], which are therefore limited to superficial and large targets [20, 124], and the invasiveness of DBS [104]. As a non-invasive technique that can accurately target deep regions in the brain, Focused Ultrasound (FUS) is a promising method for provision of cheaper, easier and safer clinical applications. Millimetric spatial resolution of transcranial focused ultrasound has been demonstrated in vitro [26, 9, 28, 29, 130, 176], in vivo [82, 129] and in clinics [148, 25, 45, 122, 134] thanks to aberration correction techniques.

1.3 Conclusion and thesis objectives

Considering the extent of neurodegenerative diseases consequences on the society and individuals, focused ultrasound therapies appear as promising techniques combining non-invasiveness, spatial accuracy and ability to reach deep brain structures. However, efforts still need to be made to amplify the effects of FUS neuromodulation by optimizing the ultrasonic parameters, to understand its mechanism and to control the technique safety. Indeed, the observed effects are so far limited to a few minutes [33, 223] and the temperature rise can lead to tissue lesions [112], especially when increasing the pressure amplitude to reach higher success rates [96, 101]. Neuromodulation effects can be observed on behavioral protocols [36] like visual tasks, or physiological observations [110] such as somatosensory evoked potential (SSEP). Likewise, drug delivery through blood brain barrier opening holds great promises for brain therapies, but its feasibility and safety need to be assessed on primates. In this thesis, the temperature rise associated with ultrasound neurostimulation in previous studies was estimated with a numerical code and ex vivo measurements (chapter 2). The frequency dependency was investigated with numerical simulations and in vitro experiments (chapter 3), evaluating the balance between little absorbed low frequency, but subject to interferences we cannot control, and more focused high frequency, harder to transmit through the skull. To evaluate physiologically the ultrasound effects at the lowest level, the activity of individual neurons was measured on macaques performing a task during ultrasonic neuromodulation (chapter 4). To increase the duration of neuromodulation effects, which were limited to less than 10 minutes in previous studies, a 20 second-long ultrasound sequence was tested on macaques performing a visual task. The stimulation led to a significant modulation of the visual activity up to 25 minutes after the sonication (chapter 5). To prove the feasibility of studying brain connectivity with ultrasound, functional MRI was used after neurostimulation of different brain regions of anesthetized macaques (chapter 6). Finally, the visual activity of macaques was modified through FUS-induced BBB-opening and delivery of an inhibitory neurotransmitter, proving the feasibility of delivering drugs non-invasively to targets regions of large animals brain, with a real time safety control (chapter 7).

Chapter 2

Numerical estimation of temperature elevation during ultrasonic neurostimulation

2.1 Introduction

Neuromodulation efficiency is closely related to ultrasound pressure amplitude: minimum thresholds have been reported for movement elicitation in rodents, and the success rate generally increases with the intensity [101, 227]. However, increasing the pressure raises safety issues due to the heat generated through ultrasound absorption by the tissue. Interestingly, some of the the earliest studies highlighted the dependence of the results on temperature [59, 116]: Lele et al [116] found the threshold dose for ultrasound-induced activity on peripheral nerves to be inversely proportional to ambient temperature. They additionally thermally induced activity in nerves by local application of heat, with similar or better results than ultrasonic radiation, demonstrating the existence of a temperature-mediated mechanism for neurostimulation. However, the predominance of non-thermal effects was demonstrated as early as 1950 [61] by showing an ultrasound induced reduction of activity in a crayfish ventral abdominal nerve cord while the modest temperature rise, estimated to $1^{\circ}C$ by the authors, had been shown to increase the firing frequency of this type of

neurons [174]. More recently, reversible effects on animals' central nervous system were elicited with reduced ultrasound dosages, giving a new momentum to ultrasonic neuromodulation. Tyler and his group [114, 206] were the first to elicit movements in anesthetized rodents, with pressure amplitudes as low as 50 kPa in the brain. In 2012, Yang et al [221] demonstrated that low intensity focused ultrasound reduced extracellular GABA levels in rats. In 2013, Younan et al [227] reproduced Tyler's motor elicitation results and reported a pressure threshold below which no elicitation could be seen. Based on these low (sub-MHz) frequency results, some groups proposed to increase the frequency so as to reach a better accuracy: King et al [101] and Ye et al [222] investigated the frequency dependence of neurostimulation in mice up to 2.9 MHz, Li et al [118] moved forward along this path with 5 MHz sonications on mice and more recently Kamimura et al [96] showed cortical and subcortical neuromodulation at 1.9 MHz on mice.

In this study, we analyze retrospectively a selection of recent studies performed in rodents only in order to estimate the thermal rise in the central nervous system and the skull. Younan et al [227], Ye et al [222], Li et al [118], Yang et al [221] and Kamimura et al [96] were selected in order to cover a large range of frequencies (320 kHz, 500 kHz, 650 kHz, 1 MHz, 1.4 MHz, 1.9 MHz and 5 MHz). 3D simulations using a K-space pseudo spectral method [32] were performed in order to simulate the ultrasonic field in the head, based on the respective parameters and transducer shape and location reported in the studies. Thermal rise was then simulated by solving the bioheat equation. Additionally, we experimentally measured the thermal rise during sonication on a mouse head, using the ultrasound parameters of two different setups for which the simulations highlighted a significant difference in thermal rise.

2.2 Methods

2.2.1 Simulations

Acoustic propagation The acoustic propagation of focused ultrasound was simulated in an entire rat head in order to investigate the pressure amplitude and spatial distribution. The simulations were performed with k-Wave [32], a k-space pseudospectral method-based solver. 3D maps of the skull, brain, and tissues were extracted from a rat micro-computed tomography (μ CT) scan (80 μ m resolution). Brain and tissues were assumed to have the same sound-speed and den-

sity as water ($\rho_{water} = 1000kg/m^3$ and $c_{water} = 1500m/s$) and the transducer was modeled according to each study’s materials (Table 2.1). Absorption was taken into account in the skull ($\alpha = 2.7dB/cm/MHz^{-1.18}$) and in the brain ($\alpha = 0.21 dB/cm/MHz^{-1.18}$) with a 1.18 power law of frequency [67] (Figure 2.1). To determine the time-step in the numerical simulation, the Courant–Friedrichs–Lewy number was set to 0.2.

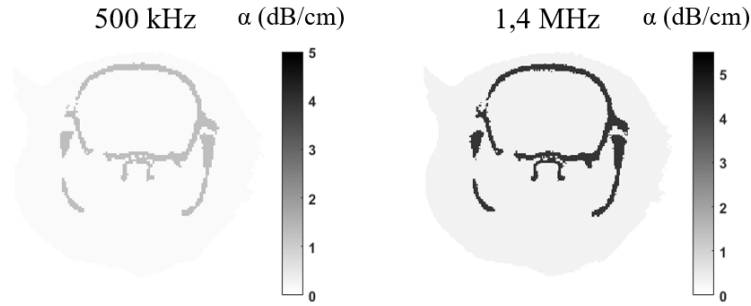


Figure 2.1: Coronal view of absorption maps at 500 kHz (left) and 1.4 MHz (right)

Table 2.1: Parameters and results in brain and at the focal spot.

Setup #	Group	Animal	f_0	Duty cycle	Pulse length (ms)	Total sonication time / number of pulses	Transducer diameter (mm)	Focal length (mm)	Spatial Sampling ($\lambda = \lambda_{tissue}$)
1	Younan et al	Rat	320 kHz	50%	0.23	250ms/500 pulses	64	62.6	0.24mm = $\lambda/20$
2			500 kHz				25.4	31.8	0.24mm = $\lambda/13$
3	Ye et al	Mice	1.4 MHz	100%	80	80ms/1 pulse	19	25.4	0.16mm = $\lambda/7$
4			1.9 MHz				19	25.4	0.16mm = $\lambda/5$
5	Li et al	Mice	1 MHz	50%	0.5	300ms/300 pulses	19	38	0.16mm = $\lambda/9$
6		Mice	5 MHz						0.08mm = $\lambda/4$
7	Yang et al	Rat	650 kHz	5%	0.5	20min/120.000 pulses	60	70	0.24mm = $\lambda/10$
8	Kamimura et al	Mice	1.9 MHz	50%	0.5	20s (1s on, 1s off)/10.000 pulses	70	60	0.16mm = $\lambda/5$

The geometry of the transducer was reproduced according to the materials and methods of each study. The transducer frequency, diameter and focal length are summarized in Table 2.1, together with the duty cycle, pulse length, and total sonication time. The spatial samplings of the simulations are also provided in Table 2.1. It was assumed for all simulation a perfect coupling between the transducer and the rat head by filling a coupling cone with water. The geometrical focal point is located inside the brain, according to the description found in the papers.

For setups #1, 4, 5, 6, 7, we first calculated the pressure at the focal spot in water based on the data provided by each study materials and methods (Table 2.2). In Younan et al case (setup #1) [227], the pressure at focus in water was directly reported. Li et al (setup #4 and 5) [118] reported the estimated I_{SPPA} in the brain and the transmission coefficients used for that calculation, so we could calculate back the pressure in water based on that information. Similarly, Yang et al (setup #6) [221] and Kamimura et al (setup #7) [96] provided the estimated peak pressure in the brain and the transmission coefficients, allowing to recover the pressure value in water. For Ye et al study (setup #2 and 3) [222], the article did not report the calibrated value of pressure in water or transmission but they provided their own estimation of the peak pressure in brain. We used it to rescale the pressure field obtained with our simulations. Amongst all the experiments performed by Ye et al, we selected the ones achieved with a reported $3W/cm^2$ I_{SPPA} at focus (corresponding to success rates of 0.5 at 500 kHz and 0.2 at 1.4 MHz), corresponding to a 0.3 MPa pressure in the brain. We also selected their 1.9MHz experiment at the highest I_{SPPA} ($90W/cm^2$) to establish a comparison with setup #8 and reproduce the procedure on a mouse while monitoring the temperature. The simulations were first performed in water to determine the acoustic intensity to apply on the simulated transducer surface in order to produce the same pressure amplitude at focus in water. The same acoustic power was then applied on the surface of the transducer for the simulation of the propagation in the rat head. The peak negative pressure in the rat head was extracted from the simulation and thus takes into account reflections and absorption effects.

Thermal simulation The simulations were first performed in water to determine the acoustic intensity to apply on the simulated transducer surface in order to produce the same pressure amplitude at focus in water. The same acoustic power was then applied on the surface of the transducer for the simulation of the propagation in the rat head. The peak negative pressure in the rat head was extracted from the simulation and thus takes into account reflections and

Table 2.2: Estimated pressures in water based on the reported data.

Setup #	Group	f_0	Reported value for I_{sppa} or pressure in brain	Reported value for peak pressure in brain	Reported Transmission used for the in situ estimation	Reported pressure at focus in water	Calculated pressure at focus in water	Simulated pressure at focus in water
1	Younan et al	320 kHz	-	-	-	0.68 MPa	-	0.68 MPa
2	Ye et al	500 kHz	$3W/cm^2$	-	-	-	-	0.3 MPa
3		1.4 MHz	$3W/cm^2$	-	-	-	-	0.3 MPa
4		1.9 MHz	$90W/cm^2$	-	-	-	-	1.6 MPa
5	Li et al	1 MHz	$210 mW/cm^2$	-	89%	-	0.12 MPa	0.12 MPa
6		5 MHz	-	-	38%	-	0.19 MPa	0.19 MPa
7	Yang et al	650 kHz	-	0.49 MPa	87%	-	0.56 MPa	0.56 MPa
8	Kamimura et al	1.9 MHz	-	1.79 MPa	68%	-	2.6 MPa	2.6 MPa

absorption effects. The thermal modeling is based on the bio-heat equation [161]:

$$\rho C \frac{\partial T}{\partial t} = \kappa \nabla^2 T + q + w \rho_b C_b (T - T_a)$$

where T, ρ, C, κ and q are the temperature, density, specific heat, thermal conductivity and rate of heat production defined as $q = \alpha \frac{PPP^2}{2\rho c}$, α being the absorption and PPP the peak positive pressure. The last term corresponds to the perfusion process, w, ρ_b, C_b and T_a being the blood perfusion rate, blood density, blood specific heat and blood ambient temperature respectively. These parameters are taken homogeneous over the brain, although a more detailed description of the brain cooling processes can be found in the literature [213]. The bioheat equation is solved by using a finite-difference scheme in Matlab (Mathwork, Natick, USA) with Dirichlet boundary conditions ($T = 37^\circ C$ on boundaries).

Thermal simulations were run over the entire sonication time for each setup except for setup #7 for which the memory requirement were too high for a 20 min sonication. Computation lasted for 200s only for setup #8, which was enough to reach the steady state (see results). The cooling time was adjusted to allow the temperature to go back to baseline (less than $0.02^\circ C$ above baseline for all setups, except for setup #8 for which the temperature was still $0.1^\circ C$ above baseline 10s after the last sonication).

The thermal dose was introduced to estimate tissue damage under thermal stress [38]. It is given by

$$TD = \int R^{43-T} dt$$

where $R = 0.25$ if $T < 43$ and $R = 0.5$ if $T > 43$. Its unit is CEM (cumulative equivalent minutes at $43^\circ C$).

2.2.2 Model validation

We compared the temperature rise estimated with our code and with the FDA High Intensity Focused Ultrasound (HIFU) simulator [195] for the propagation of $0.5 MHz$, $1 MHz$ and $1.5 MHz$ ultrasound continuous waves by a single-element transducer with a 1.25 cm diameter and 4 cm focusing in homogeneous tissue with HIFU simulator default absorption value ($5.8 dB/cm/MHz^{-1.1}$). The tissue properties are summarized in Table 2.3. The perfusion parameters are taken from Pulkkinen et al [176]: $w = 0.008 s^{-1}$, $\rho_b = 1030 kg/m^3$, $C_b = 3620 J/kg/K$ and $T_a = 37^\circ C$. The FDA HIFU simulator solves the Khokhlov-Zabolotskaya-Kuznetsov (KZK) equation. As the KZK equation is valid for angles smaller than 20° [107], the FDA HIFU simulator recommends using an f-number higher than 1.37. Therefore the transducer geometry was designed with an f-number higher than twice this recommended value. For each frequency the power was adjusted so that the temperature rise would be about $10^\circ C$ after 3 seconds of sonication. The space step used in k-wave was set to the one defined by HIFU simulator. The pressure field from k-Wave propagation was then rescaled so that the maximum pressure amplitude matches the one from HIFU simulator, and the thermal parts were run separately to compare the maximum temperatures. The main parameters and results of the simulations are listed in Table 2.4. The deviation between the thermal results remains below 9% for all frequencies and is partly due to the difference of pressure field after propagation, that is itself a consequence of the difference between the models (HIFU simulator solves the KZK equation, k-wave uses a k-space pseudo-spectral solver). The pressure profiles in the axial direction as well as the temperature rise for 2 MHz are plotted in Figure 2.2.

Table 2.3: Tissue properties for simulations

	Density (kg/m^3)	Sound speed (m/s)	Absorption ($Np/m/MHz^{-1.18}$)	Specific heat ($J/kg/K$)	Thermal conductivity ($W/m/K$)
Bone	1850	2400	31 [166]	1300 [42]	0.4 [42]
Tissue	1000	1500	2.4 [67]	3600 [42]	0.528 [42]

Table 2.4: Validation of the numerical model with a comparison with HIFU simulator in the 0.5 – 2 MHz range: results.

Frequency	Power	Space step (mm)	Pmax	T (3s),k-wave + bioheat solver	T (3s), HIFU simulator	Deviation (%)
0.5 MHz	50W	0.252	2.8 MPa	47, 7°C	47, 2°C	4.6
1MHz	12 W	0.126	2.1 MPa	47, 3°C	46, 7°C	6.0
1.5 MHz	7 W	0.086	1.9 MPa	48, 3°C	47, 6°C	6.1
2 MHz	4 W	0.063	1.6 MPa	45, 9°C	45, 3°C	8.1

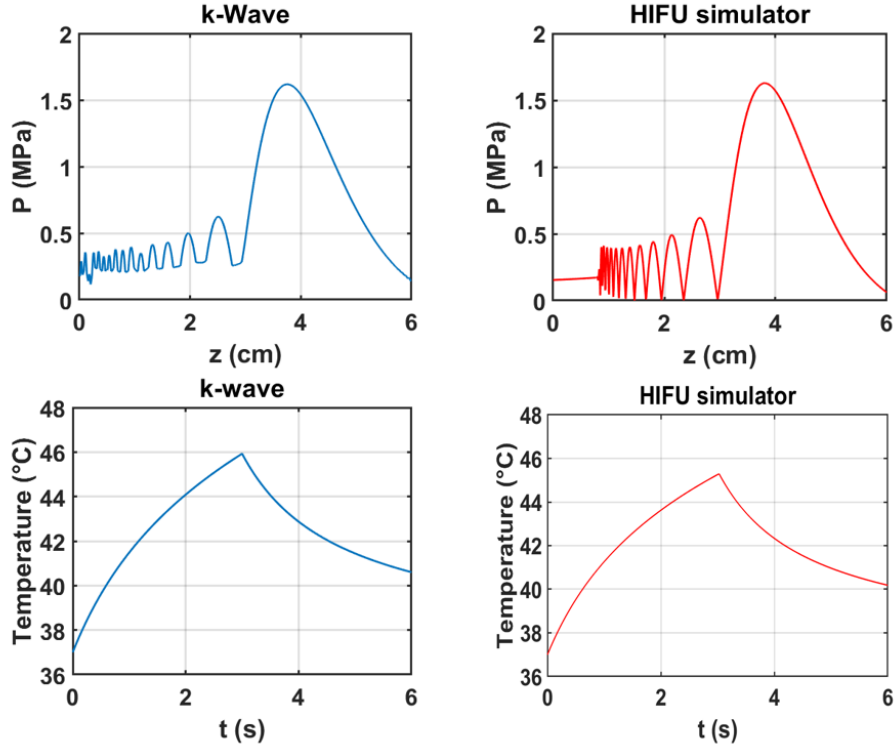


Figure 2.2: Model validation: pressure profile (up) and temperature rise (bottom) with k-Wave [32] (left) and HIFU simulator [195] (right)

2.2.3 Measurements of temperature rise in mouse

Ex-vivo measurements were performed on a mouse enrolled in the project "Study of cerebral plasticity in the adult brain, associated with two animal models of psychiatric/neurologic disorders" validated by the Comité d’Ethique en Expérimentation Animale n°59 under the reference 2015-23. Since this protocol ends with euthanasia, we could perform the neurostimulation sequence and temperature measurements immediately after sacrifice. The mouse (c57Bl/6JRj, 3 months old, 34g) was anesthetized with ketamine (80mg/kg) and xylazine (20 mg/kg) and sacrificed with pentobarbital (800 mg/kg). The injections were intraperitoneal. The measurements were performed right after sacrifice and lasted less than an hour. We used a single element transducer (center frequency: 2.25MHz, focal length: 2cm, diameter: 2.2cm, Imasonic, Voray sur L’Ognon, France) at the frequency of 2 MHz, identical to the one used previously in [37]. The transducer was mounted with a 50 μ m thick latex membrane (Durex, Reckitt Benckiser, Slough, United Kingdom), in front of the active piezoelectric material. The cavity between the transducer and the membrane was filled with degassed water. The animal’s head was shaved with a depilatory cream (Klorane, France). The signal was generated with a digital function generator (Handyscope HS5, TiePie engineering, Sneek, The Netherlands) and amplified with a 75-Watts amplifier (75A250A, Amplifier Research, Souderton, PA). The output voltage was monitored with an oscilloscope (DPO 3034, Tektronix, France). The transducer was previously calibrated on a custom-built heterodyne interferometer (compact heterodyne probe of the Mach-Zehnder type described previously [178]) leading to a direct relation between the voltage and the pressure at focus in water. Temperature was monitored by a Copper-Constantan thermocouple (Type T, 0.010 in diameter, Omega, Stamford, CT) subcutaneously introduced in the mouse head skin above the skull, using a 18G needle. Recording was achieved by an acquisition board (TC-08, Pico Technology, Cambridgeshire, UK) connected to a PC. The transducer was positioned with a mechanical gantry to target the brain, with the thermocouple at the center of the ultrasonic wave axis. We aimed at reproducing the ultrasound sonications of setups #4 [222] (1.9 MHz, 1.6 MPa in the brain, 80 ms single pulse) and #8 [96] (1.9MHz, 1.9MPa in the brain, 50% duty cycle for 1s followed by 1s of cooling, total sonication time 20 s). However, as the transducer could not deliver enough power at 1.9 MHz, we set the frequency to 2 MHz (closer to the center frequency, 2.25MHz). We assumed a transmission coefficient of 68% through the mouse skull, so the input voltages were set to 34V and 38V, corre-

sponding to 2.3 MPa and 2.6 MPa pressure amplitude in water, for setups #4 (Kamimura et al) and #8 (Ye et al) respectively.

2.3 Results

2.3.1 Simulations

3D pressure fields were obtained for all simulations. Figure 2.3 shows a typical low frequency (320 kHz, top) and high frequency (1.9 MHz, bottom) pressure field. The maximal pressure amplitude in the brain is 0.95 MPa at 320 kHz and 1.86 MPa at 1.9 MHz. According to the experimental setup, the target was located in the left hemisphere for the 1.9 MHz sonication [96].

Table 2.5: Parameters (frequency, duty cycle, pulse length, total sonication time) taken from the literature and results (maximum pressure, temperature in brain and at the focal spot) obtained from the simulations. Baseline temperature is assumed to be $37^{\circ}C$.

Setup #	Group	f_0	Duty cycle	Pulse length (ms)	Total sonication time	Maximum pressure in brain (MPa)	Temperature at focal spot (Temperature rise $\Delta T(^{\circ}C)$)	Max Temperature in brain (Temperature rise $\Delta T(^{\circ}C)$)
1	Younan et al	320 kHz	50 %	0.23	250ms	0.95	37.01 ($\Delta T = 0.01$)	37.06 ($\Delta T = 0.06$)
2		500 kHz				0.3	37.001 ($\Delta T = 0.001$)	37.007 ($\Delta T = 0.007$)
3	Ye et al	1.4 MHz	100%	80	80ms	0.3	37.002 ($\Delta T = 0.002$)	37.02 ($\Delta T = 0.02$)
4		1.9 MHz				1.6	37.07 ($\Delta T = 0.07$)	37.8 ($\Delta T = 0.8$)
5	Li et al	1 MHz	50%	0.5	300ms	0.12	37.0005 ($\Delta T = 0.0005$)	37.006 ($\Delta T = 0.006$)
6		5 MHz				0.16	37.003 ($\Delta T = 0.003$)	37.07 ($\Delta T = 0.07$)
7	Yang et al	650 kHz	5%	0.5	20min	0.45	37.03 ($\Delta T = 0.03$)	37.07 ($\Delta T = 0.07$)
8	Kamimura et al	1.9 MHz	50%	0.5	20s 1s on, 1s off	1.9	38.3 ($\Delta T = 1.3$)	44 ($\Delta T = 7.0$)

Table 2.5 summarizes the sonication parameters (duty cycle, pulse length, sonication time, and transducer characteristics) and the result of the simulations: peak pressure in the brain, maximum temperature in the brain and at focal spot. In all cases but setups #4 and #8, the maximum

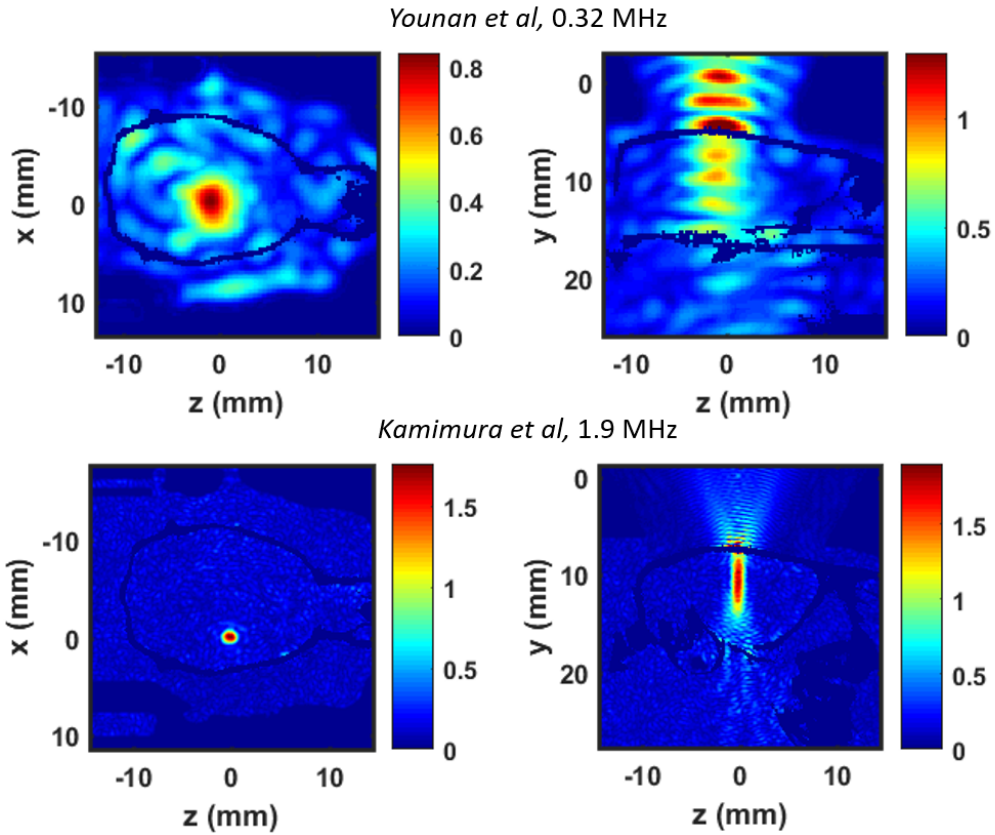


Figure 2.3: Peak pressure fields in rat brain at 0.32kHz (up) and 1.9MHz (bottom), based on Younan et al [227] and Kamimura et al [96] parameters, respectively. Axial planes (left) and sagittal planes (right) are presented. In sagittal plane, the transducer is located above the head, on the top of the image.

pressure in the brain is below 1 MPa.

Temperature rise estimated for setup #1 [227] and setup #8 [96] are plotted on Figure 2.4 and 2.5 respectively at the focal spot (left) and at the most heated point in the brain (right), with a zoom on individual bursts.

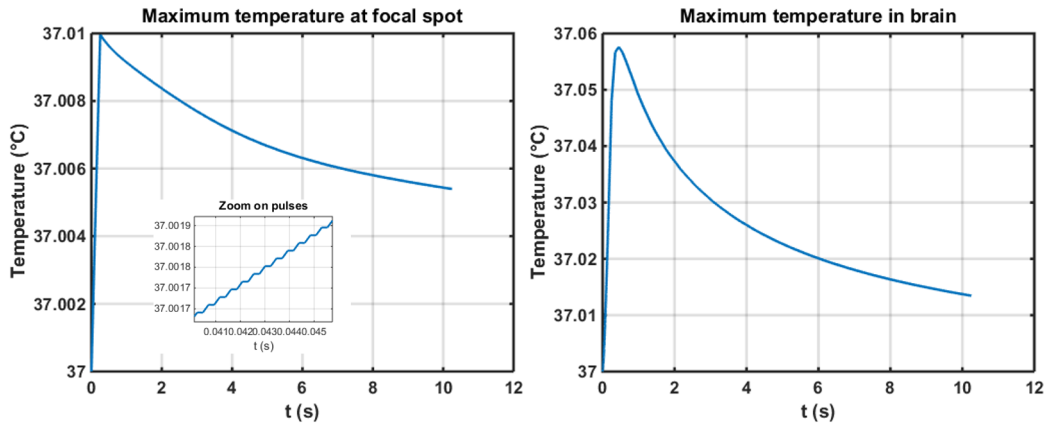


Figure 2.4: Estimated temperature rise at 320kHz [227]. The zoom (left onset) is taken from the range [41 ms - 45 ms].

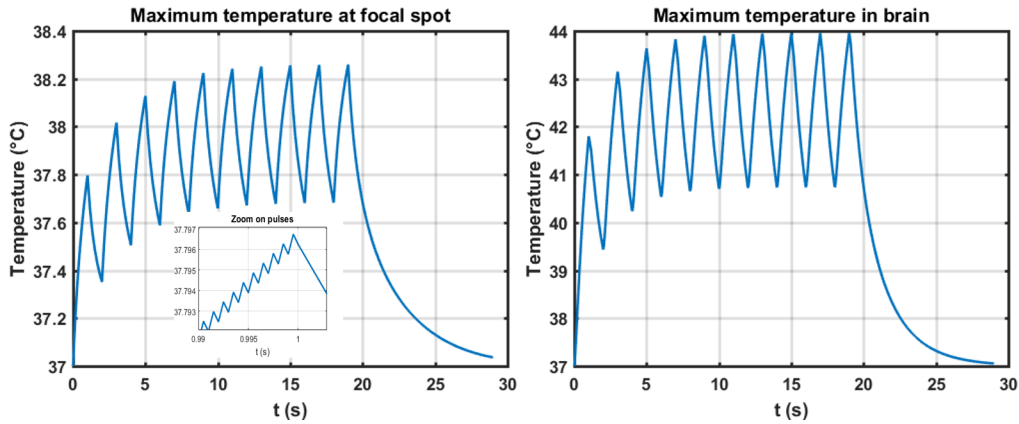


Figure 2.5: Estimated temperature rise at 1.9MHz [96]. The zoom (left onset) is taken from the end of the first second of sonication.

2.3.2 Measurements of temperature rise in mouse

Figure 2.6 displays the temperature measurements during the sonications: one “setup #8” type sequence followed by four successive “setup #4” type sequences. This value of thermal rise (4.3°C for setup #8 (Kamimura et al) type sonication and 0.3°C for setup #4 (Ye et al) type sonication) was found for two different positions, while the other positions that we tested would give a lower temperature rise. To compare experimental and numerical results, we report in Table 2.6 the thermal rise calculated in the skin from simulations. The first column displays the maximum value, which was reached in a single point adjacent to the skull in both cases, and the second column presents the mean value in a $1 \times 1\text{mm}$ range in the lateral direction and 0.5mm range in the

Table 2.6: Estimated and measured thermal rise in the mouse skin head

	Maximum thermal rise in the skin from simulations	Mean thermal rise on a 1x1x0.5mm area in the skin next to the skull centered on the propagation axis, from simulations	Measured thermal rise in the skin (mean of the four maximal values measured on two different positions)
Setup #4	1.1°C	0.27°C	$0.29 \pm 0.02^\circ\text{C}$
Setup #8	8.9°C	4.1°C	$4.3 \pm 0.1^\circ\text{C}$

axial direction, in the cutaneous area next to the skull centered on the propagation axis, excluding the skull region.

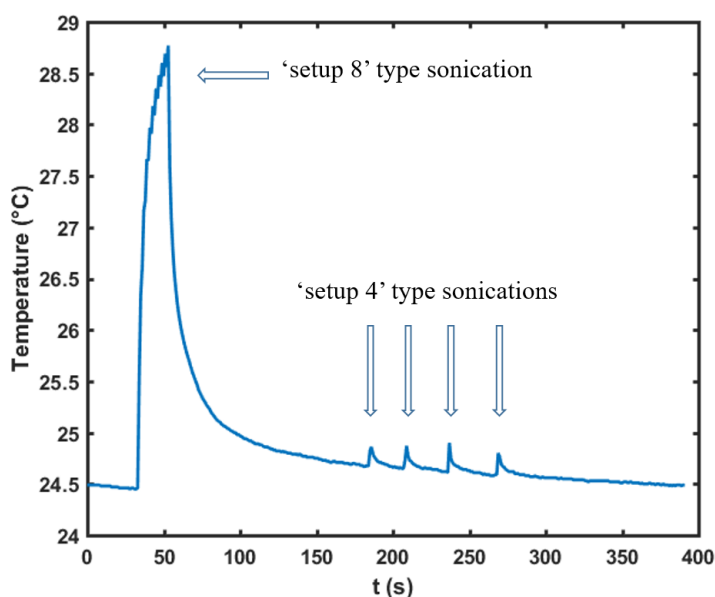


Figure 2.6: Temperature measured in a mouse head skin with a thermocouple during two different sequences of ultrasonic neuromodulation

2.4 Discussion

For each study we report both the temperature at target location and the maximum temperature overall in the rat brain. This location of the maximum temperature elevation is distinct from the target location. The temperature rise is indeed higher in the skull than in brain tissue due to their difference in thermal parameters : in setup #8 [96], we estimate a maximum temperature of 49.0°C in the skull and 43.15°C in the brain after 3 seconds. By diffusion effects, tissues near the skull

heat more than those deeper inside (Figure 2.7 a) [83, 88]. This also explains the unusual relaxation time that can be observed (Figure 2.4, right as opposed to Figure 2.4, left): the temperature of tissue near the skull does not drop immediately at the end of the sonication. They keep being heated by the skull for about 0.1s. This effect is also observed on the pulses timescale: Figure 2.7 b) c) displays the temperature during the last pulses of the sonication in Kamimura et al study [96]. The focal spot, far from the bone, undergoes a thermal rise during the pulses and cools down between them. The point of maximal temperature, on the contrary, keeps heating between the pulses: as it is located close to the bone that has reached a higher temperature, it is subject to thermal diffusion. It can also be noticed on Fig 7 that thermal rise and decay do not exhibit an exponential trend: the curve appears to be almost linear, even when further decreasing the time step of the simulation. The typical diffusion time for one pixel ($\lambda = \frac{dx^2}{\kappa} \rho C$) is indeed 0.17 s, much larger than the 5ms duration of the bursts. A higher thermal rise in the bone than in the brain was also reported [149] in a numerical study on ultrasonic neurostimulation with a layer model of human skull/cerebrospinal fluid/white matter/gray matter.

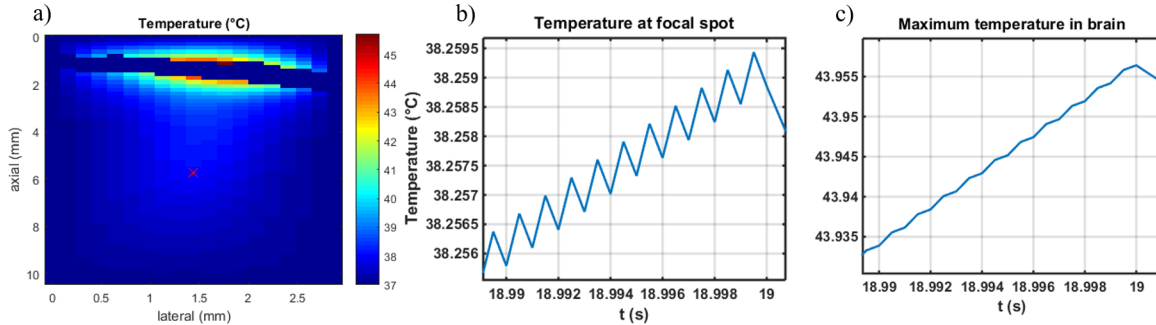


Figure 2.7: Temperature at the end of a 20s sonication at 1.9 MHz. a) The red cross represents the focal spot. The temperature reaches 45.7°C in the skin.

In setups #1, 2, 3, 5, 6 and 7, the temperature rise remains below 0.01°C , confirming that thermal effects are expected to be negligible in the neuromodulation results. Ye et al [222] measured a thermal rise of 0.01°C with setup #2 and 3, in good agreement with our results (the estimated thermal rise was between 0.007 and 0.2 0.01°C , Table 2.5). Surprisingly, Li et al [118] used a lower acoustic power and a lower duty cycle than Ye et al [222] but reported a temperature rise of 0.2°C at 1 MHz and 1.6°C at 5 MHz at $230\text{mW}/\text{cm}^2$, whereas our simulations predict a thermal rise

of only 0.006°C and 0.07°C respectively. It should be noted that a rat CT-scan was used for all simulations, whereas three of the five studies [118, 96, 222] were performed on mice. However, the numerical results are in good agreements with the experimental measurements of thermal rise in mice.

The experimental thermal rise measurements have been performed at a frequency (2 MHz) as close as possible to the one used in Kamimura et al (1.9 MHz, 1.9 MPa in the brain, 50% duty cycle, total sonication time: 20s) and Ye et al (1.9 MHz, 1.6 MPa in the brain, 80ms single pulse). It must be noted here that experiments have been performed on a euthanized mice, so that perfusion is not cooling down the tissue in contrast to the in vivo neuromodulation studies at 1.9 MHz. Nevertheless, the relative impact of the acoustic intensity and duty cycle can be assessed. Our ex vivo measurements show that maximum temperature elevation is 15 times higher when using Kamimura et al parameters as compared to Ye et al. For comparison our simulations predict the maximum temperature elevation (respectively mean temperature over a 0.5mm^3 volume) to be 8 times (respectively 15 times) higher when using Kamimura et al parameters as compared to Ye et al. In Kamimura et al. study [96] at 1.9 MHz, we estimate that temperature rises from 37 to 44°C in the brain in 20 seconds. Thermal rise is not negligible: 10 seconds after the sonication, the temperature is still higher than the maximal value, spatially and temporally, simulated in every other study. However, our thermal dose estimation (15 Cumulative equivalent minutes at 43°C (CEM) in the brain) is still compatible with the absence of lesion that Kamimura et al observed after performing histopathology at the target location. While it is commonly admitted that neuromodulation results from a mechanical phenomenon, temperature might influence its effects. Diverging studies exist on the influence of temperature on neuronal activity: it has been shown that for some neurons in the hypothalamic suprachiasmatic nucleus (SCN) [22] temperature rise increases the firing rate by a coefficient of 1.1 impulses /s / $^{\circ}\text{C}$. 12 to 22% of warm-sensitive neurons and 48 to 62% moderately temperature-sensitive neurons have been reported in the SCN, depending on the regions. Even though the SCN is located deep in the brain and is not likely to undergo the highest thermal variations, this sensitivity to temperature might also concern neurons located in path of the ultrasound. On the contrary, other groups [203, 208] observed a thermal inhibition of sciatic nerves using focused ultrasound. As the neurons concerned by neuromodulation in the simulated experiments are not located in the SCN nor in sciatic nerves, it is impossible to

predict whether their reaction to thermal rise is an activation or an inhibition.

The concept of thermal dose (TD) was introduced to quantify the heating energy brought to tissues and evaluate the risk of ultrasound induced damages [38]. It takes into account the temperature rise and the time of sonication: 1 CEM is equivalent to one second of 43°C heating. Typically, a 240 CEM thermal dose corresponds to a total necrosis of any type of tissue [38] and 17.5 CEM [139] is the threshold for a 50% probability of brain damages (Table 2.8). We calculated the thermal doses in each of the five studies: in setups #1 to 6 [227, 118, 222] thermal doses values are below 0.1 CEM in the skull, brain and skin. Setup #7 [221] exhibits a slightly higher TD (0.1 CEM) because of the longer sonication time, but this value remains much below any reported damage threshold. However in Kamimura et al. study (setup #8) [96] at 1.9 MHz, TD reaches 15 CEM in the brain (close to the bone), 42.9 CEM in the skin, and 0.75 CEM at the focal spot. The highest thermal dose was observed close to the bone. The heating of the bone has long hampered ultrasonic brain surgery as was reported in pioneering work about previous primate studies [82], and is still of concern during current clinical treatments [88]. The thermal dose on target (0.75 CEM) agrees with the absence of visible damage in the histology reported by Kamimura et al in the central part of the brain (Figure 9) in the article's supplementary material [96]). Thermal effects can be used on purpose to enhance the neuromodulation effects of ultrasound. In this context, acoustic parameter must be chosen with extreme care in order to avoid thermal damage. Our results show that most superficial parts of the brain (close to the skull) are at most thermal risk. According to our simulations, Kamimura et al successfully capped their maximum power: the thermal doses in the outer surface of the brain and in the skin reaches higher values than at the target but remain slightly below the thresholds reported [139, 38, 47] for tissue lesions (Table 2.7 and 2.8).

Thermal effects can be significantly reduced by lowering the duty cycle. In that case, tissues have more time to cool down between the pulses but mechanical effect are kept the same if the peak pressure remains unchanged. To illustrate this, we ran two simulations based on the same sonication parameters than Kamimura et al, but changing the duty cycle from 50% to 25% and 5%. Figure 2.8 shows the maximum temperature at the target (left) and the maximum temperature (right) for the three duty cycles. Results are listed in Table 2.7 for the maximum temperature in the brain and in the skin near the skull. Compared to a 50% duty cycle, a 25% duty cycle divides the thermal dose by a factor of 7 (in the brain) to 13 (in the skin) and a 5% duty cycle by a factor

Table 2.7: Results for temperature and thermal dose with varied duty cycles, at 1.9 MHz, 1.6 MPa in the brain

Duty cycle	Temperature at focal spot ($^{\circ}\text{C}$)	Max Temperature in brain ($^{\circ}\text{C}$)	Thermal dose in the brain (CEM)	Thermal dose in the skin (CEM)
5%	37.1	37.7	0.012	0.014
25%	37.6	40.5	2.2	3.4
50%	38.3	44.0	15	42.9

Table 2.8: Reported threshold values of thermal dose for thermal necrosis.

Reported thermal dose threshold for brain damages	Reported thermal dose threshold for skin damages	Reported thermal dose threshold for muscle damages
17.5 CEM (50% probability) [139] 25 CEM [38]	210 CEM [38]	240 CEM [38]

of 1250 (brain) to 3000 (skin).

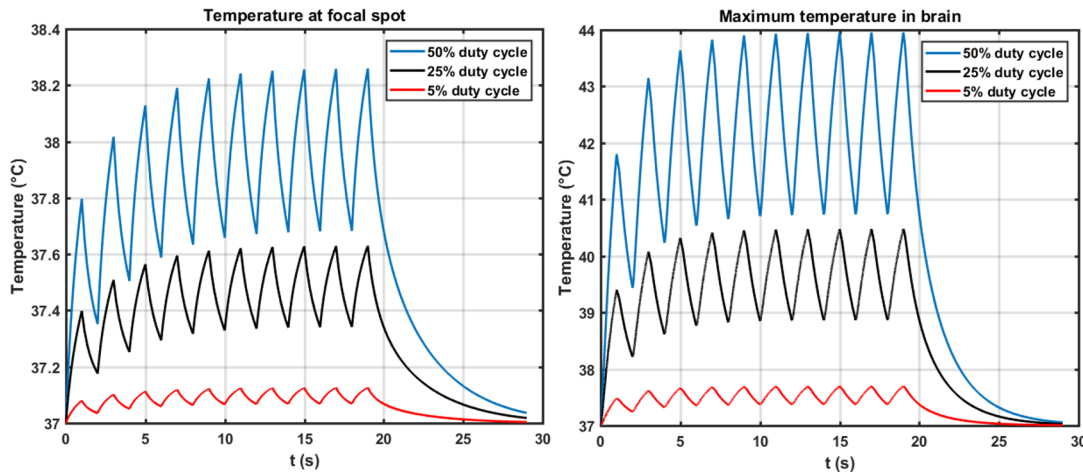


Figure 2.8: Estimated temperature rise at 1.9 MHz, with the same parameters as in Kamimura et al [96], except for the duty cycles.

The temperature measurements performed on a mouse support our simulations results. For setups #4 and 8, the maximum temperature in the skin at the end of the sonication is predicted to be 38.1°C ($dT = 1.1^{\circ}\text{C}$) and 45.9°C ($dT = 8.9^{\circ}\text{C}$), respectively, in our simulations (Table 2.6). The fact that we did not observe as high temperature increases as calculated is not surprising: given the small size of the focal spot at 1.9 MHz, it is very hard to target it. Besides, the most heated point from simulations was, in both cases, right next to the skull; this position could not be

reached with the thermocouple subcutaneously introduced into the skin. Therefore we calculated the mean value of ΔT in a small area (1x1x0.5mm) around this point to estimate a more realistic value of the temperature that can be measured experimentally (Table 2.6). They compare well with the experimental measures: for setup #4 [101], the mean value from simulations matches the measured thermal rise (0.2°C) and for setup #8 [96], the values of thermal rise from simulations and experiments are close (respectively 4.1°C and 4.3°C).

2.5 Conclusion

Our retrospective analysis shows that thermal effects can be neglected in almost all the simulated neuromodulation experiments. For setups #1 to 7 [221, 227, 118, 222], corresponding to a frequency range of 320 kHz to 5 MHz and a total sonication time ranging from 80 ms to 20 min, the maximum temperature elevation in the rodent brain is indeed lower than 1°C. In the case of setup #8 [96], for a 20 seconds total sonication time, the thermal rise reaches 1.3°C at the target and 7°C near the skull. In that case, both thermal and mechanical effects could plausibly contribute to the neuromodulatory effect of ultrasound, which can be accepted as long as the thermal dose does not exceed the threshold of tissue damage. The simulations presented in this chapter highlighted the impact of the frequency and the size of the transducer on the spot size. It would be useful to compare the efficiency of ultrasonic neuromodulation at different carrying frequencies with the same transducer located at one given target in the brain. In the next chapter, we present a multifrequency transducer which delivers enough energy to achieve neuromodulation in the brain of rodents and primates at four different frequencies ranging from 200kHz to 1380kHz.

Chapter 3

Towards a multifrequency ultrasonic neurostimulation

3.1 Introduction

Focused ultrasound neurostimulation has been proven effective between 320 kHz and 1.9 MHz. Multiple frequencies have been used in this range [36, 56, 95, 99, 114, 143, 206, 207, 221, 224, 227] but in most studies, only one frequency is tested. King *et al.* achieved significant ultrasonic neuromodulation between 250 kHz and 500 kHz, within the limited bandwidth of a single element planar transducer [101] (figure 3.1). Recently, it has been demonstrated that FUS could be effective at frequencies up to 2.9 MHz [222] and 5 MHz [118], provided that the sonication intensity could be increased sufficiently. There is a balance to be found between low frequency waves, efficiently transmitted through the brain but providing poor resolution ($\lambda = 7.5\text{mm}$ in water at 200 kHz), and high frequency waves, which can give a sharper beam ($\lambda = 1\text{mm}$ in water at 1400 kHz) but are dramatically affected by attenuation in the skull. Plaksin *et al.* [168] proposed a theoretical model which predicted that the intensity activation threshold for action potentials generation does not depend on the frequency, suggesting that precise focusing compensates for attenuation at higher frequencies. Until now, the fact that most studies have been performed at a single frequency makes verification of this prediction difficult. Moreover, the comparison of neuromodulation studies performed at varying frequencies with different transducers is very challenging. There is a real need

to perform multi frequency studies at a fixed location, preferably with a unique transducer capable of sonicating at different frequencies, so that all other parameters are kept constant (aperture, focal distance, location of the target, area of skull intercepting the beam). We propose the use of a

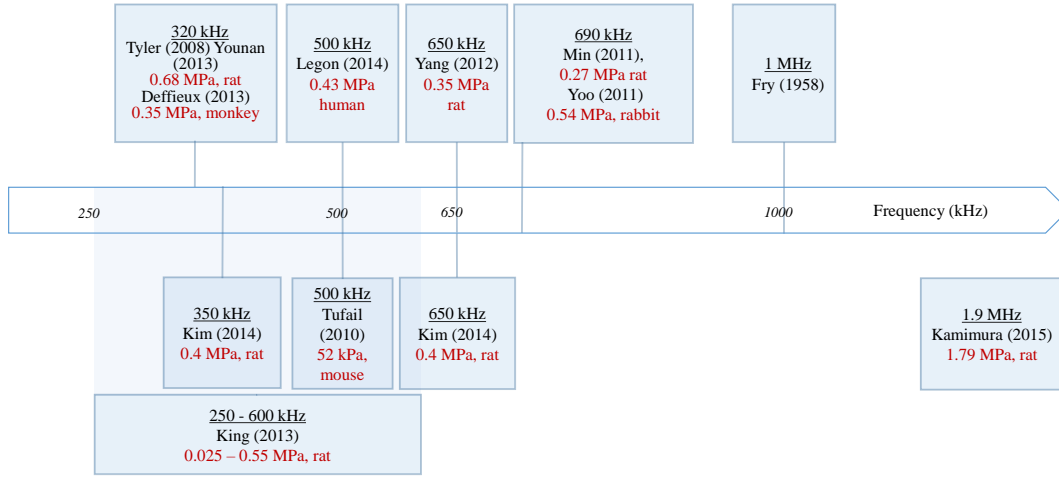


Figure 3.1: Schematic review of maximum pressures applied in brain to achieve neuromodulation.

quadri-band transducer to perform such measurements on a larger frequency range. Additionally, we have built a numerical model based on μ -computed tomography (μ CT)-scans of a rat, and two CT-scans of macaques, to predict the pressure field in the brain of rodents or primates for the four frequencies involved. The model takes into account skull heterogeneities, absorption and source apodization.

3.2 Materials and methods

3.2.1 Transducer

A single-element transducer (H115, Sonic Concepts, Bothel, USA, radius of curvature: 63mm, active diameter: 64mm) was used at its resonance frequencies: 200 kHz, 320 kHz, 850 kHz and 1380 kHz. It was characterized using a network analyzer (Rohde Schwarz, Munich, Germany) between 100 kHz and 1.5 MHz. A cone filled with water was attached to it in order to allow

acoustic coupling with water in contact with the animal head. The transducer was calibrated using a heterodyne interferometer (compact heterodyne probe of the Mach-Zehnder type described previously [178] in water, and after transmission through a monkey skull. The pressure in the focal plane after transmission through pure degassed water was measured for each frequency using powers ranging from 18 to 75 electrical watts. Electrical power was generated by a function generator (Handyscope HS5, Tiepie Engineering, Sneek, The Netherlands) connected to a 75 W amplifier (75A250A, Amplifier Research) and input voltage and current applied to the transducer were monitored on the Handyscope channels. No matching circuit was used. The monkey skull was put in water and degassed for 2 days ($P < 2$ mbar, pump from Fisher Scientific, Waltham, USA) before the measurements. Several positions were tested, and for each position and frequency, the maximum pressure was found by scanning the area in 3 dimensions.

3.2.2 Numerical simulations

The propagation of focused ultrasound was simulated in an entire rat head, and in two monkey heads, in order to investigate the pressure amplitude and spatial distribution as a function of frequency. To get some insight into the transmission through a monkey skull and get the absorption parameters, we also simulated the propagation of ultrasound through a monkey skull flap, after measuring the transmission through the same piece of skull with the heterodyne interferometer.

The simulations were performed using a k-space pseudospectral method-based solver, k-Wave [32]. 3D maps of the skull, brain, and information on the morphology of tissues were extracted from a rat μ CT scan ($80\mu\text{m}$ resolution), monkey computed tomography (CT) scans (respectively 0.14 mm and 0.36 mm resolutions for female (monkey L) and male (monkey Y)) and dry monkey skull CT scan (0.1 mm resolution). The simulations were first performed in pure water and compared with the amplitude measured experimentally. For each frequency, a scaling factor was used as a correction factor in order to estimate the absolute pressure in the head or behind the skull flap.

Simulations through a monkey skull flap The bone flap (29mm x 31mm) was salvaged after a craniotomy from the left parietal region of a macaque skull (*macaca fascicularis*), performed at the Institut du Cerveau et de la Moëlle in 2014. As the skull's heterogeneities are pronounced and may be bigger in size than the wavelength, a linear relationship was used between the Hounsfield Units (HU) from the CT scan and sound speed and density (figure 3.5a)):

The power law model for attenuation is $abs = \alpha\Phi^\beta$ where the porosity Φ is defined by $\Phi = \frac{\rho_{max} - \rho}{\rho_{max} - \rho_{water}}$ in the skull [9], where ρ is the density in the skull extracted from the CT scans. The absorption coefficient α depends on the frequency: $\alpha = \alpha_0 f^b$. A series of simulations was performed at four different frequencies to determine the parameters $\rho_{max}, c_{max}, \beta$ and b that gave the best match with measurements in terms of frequency-dependent transmission. The simulated signal was a 20 period-long pulse. The pixel size was smaller than $\lambda/9.5$ for each frequency (200, 320, 850 and 1380 kHz), where λ is the wavelength in water. Although 3 points per wavelength are sufficient for a stable k-space simulation in heterogeneous media [32], we increased the number of points up to 23 per wavelength at low frequencies in order to preserve the quality of the maps, given the small size of the heterogeneities, and the porous qualities of the skull flap. Several positions were tested by laterally translating the transducer using small lateral shifts with respect to the flap (to positions (0,0), (0,-0.5), (1,0), (-1,0) mm).

Parameters for simulations in monkey head Using the acoustic parameters determined previously from a monkey skull flap (table 3.3), we simulated the propagation of ultrasound through two entire monkey heads. Tissues were assumed to be homogeneous, with acoustic values close to those of water ($\rho_{tissue} = 1010kg/m^3, c_{tissue} = 1560m/s$). The relationship between the Hounsfield Units (HU) from the CT scan and density and sound speed was:

$$\rho = \rho_{tissue} + \frac{HU - HU_{tissue}}{HU_{max} - HU_{tissue}}(\rho_{max} - \rho_{tissue})$$

where ρ is the local density and ρ_{max} is the maximal density in the entire head. HU_{max} was determined from each map as the maximal value in the skull and HU_{tissue} as the mean value of HU in the brain, muscle and skin. The spatial step was smaller than $\lambda/4$ at all frequencies. The CT-scans were obtained from two monkeys (female monkey L and male monkey Y). Simulations were performed for both monkeys at 200 kHz, 320 kHz, 850 kHz and 1380 kHz, with a $150\mu s$ -long pulse signal (enough to reach a steady state at all frequencies). The transducer was modeled as a spherical section of given radius of curvature and active diameter. The simulated pulses were spatially apodized ($r = 0.35$) on the spherical section. The target was the Frontal Eye Field. Ultrasound propagates first through a water-filled cone before entering the head, since the geometrical focal point is located a few millimeters below the surface, inside the brain.

Table 3.1: Measured and numerical results for peak positive pressures and pressure gains in rat and monkey

	200 kHz	320 kHz	850 kHz	1380 kHz
Maximum pressure measured in water	1.1 MPa	1.0 MPa	6.0 MPa	8.5 MPa
Maximum pressure measured behind a monkey skull flap	0.83 MPa	0.79 MPa	1.9 MPa	1.6 MPa
Estimated maximum pressure in rat brain	1.8 MPa	0.89 MPa	4.0 MPa	7.0 MPa
Estimated maximum pressure in monkey L brain	0.86 MPa	0.72 MPa	3.8 MPa	5.2 MPa
Estimated maximum pressure in monkey Y brain	0.60 MPa	0.52 MPa	2.0 MPa	1.1 MPa
Estimated pressure gain in rat brain	160 %	89 %	67 %	83 %
Estimated pressure gain in monkey L brain	78 %	72 %	63 %	61 %
Estimated pressure gain in monkey Y brain	55 %	52 %	28 %	13 %

Parameters for simulations in rat head Brain and tissues were assumed to have the sound speed and density of water, and the transducer was modeled as described above for the monkey head. The spatial step was always smaller than the wavelength in water divided by 6.8. Absorption was taken into account in the skull (2.7 dB/cm/MHz) and in the brain (0.37 dB/cm/MHz) with a 1.1 power law of frequency [42]. A 230 μ s long pulse, spatially apodized ($r=0.35$) on the spherical section, was simulated, since this had previously been used in vivo with the same transducer [227]. The geometrical focal point is located about 7 mm deep below the surface, inside the rat brain. For each frequency, the area affected by ultrasound $V=SL$ was calculated, where L is the length of focal spot (in y direction) and S its surface area at the geometric focus so that $P > P_{max}/2$ (-3dB) or $P^2 > P_{max}^2/2$ (-6dB), where P_{max} is the maximum pressure inside the brain. The standing wave ratio is defined as the maximum of an anti-nodal peak pressure divided by an adjacent nodal peak pressure along the propagation axis.

3.3 Results

Transducer calibration All measured values and those estimated from numerical simulations are listed in Table 3.1. Pressure gains are defined as the ratio of maximum pressure estimated in brain in steady state to the maximum pressure in pure water, for the same signal. All measured values reported in Table 3.1 have been obtained with the amplifier operated with its maximum power. Figure 3.2 shows the transducer's impedance as a function of frequency. We note four peaks at 200 kHz, 320 kHz, 850 kHz and 1380 kHz We were able to obtain at least 1 MPa in water and 0.8 MPa behind a monkey skull flap immersed in water for each of the four frequencies (Table 3.1, 1st and 2nd rows). The pressure amplitude was limited by the amplifier, and the reported values

are the peak positive pressures (PPP) obtained at its maximum power. Figure 3.3 shows peak negative pressure (PNP) and peak positive pressure behind a monkey skull flap as a function of the output voltage, at the four frequencies, for one of the five tested positions. At each frequency, the transmission factor was calculated based on a linear fit on the six measurements reported in figure 3.3.

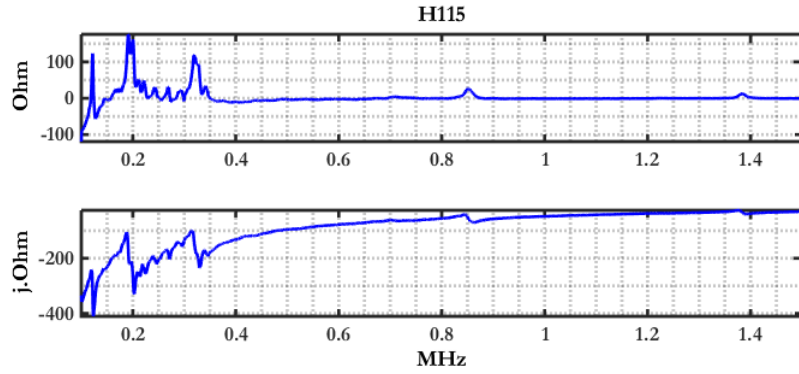


Figure 3.2: Frequency analysis for the transducer.

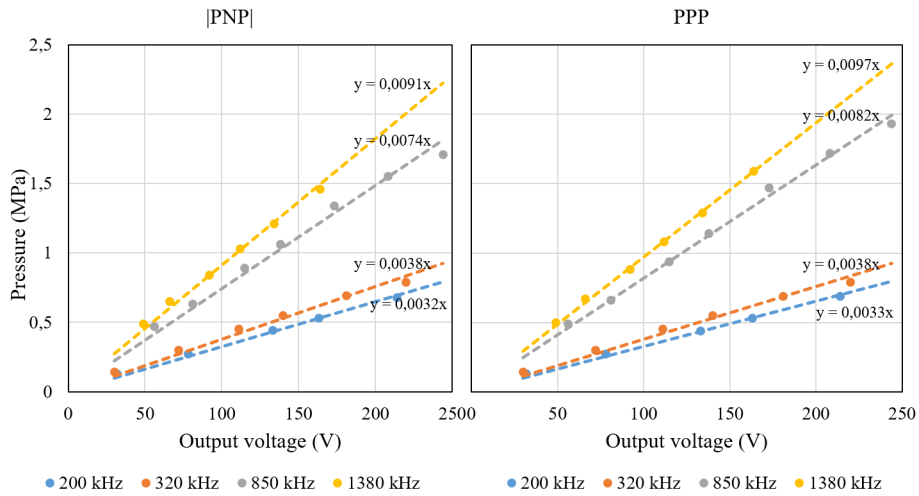


Figure 3.3: Peak negative pressure (left) and peak positive pressure (right) measured behind a monkey skull flap with respect to output voltage for one of the five tested positions.

Simulations in rat brain The normalized maximum pressure over time after ultrasound propagation is displayed, in decibels, in figure 3.4 in the focal (transversal) (1st line) and sagittal planes (2nd line), and in free water (3rd line) at all frequencies. We calculated, from calibration in water

Table 3.2: Volume of brain affected by ultrasound and standing wave ratio

	200 kHz	320 kHz	850 kHz	1380 kHz
Estimated volume for half maximum pressure (-3dB)	960 mm ³	250 mm ³	70 mm ³	23 mm ³
Estimated volume for half maximum intensity (-6dB)	540 mm ³	120 mm ³	28 mm ³	8.0 mm ³
Standing wave ratio	3.67	2.09	1.19	1.04

and the simulations in free field, a scaling factor that was used to estimate the maximum pressure inside the rat brain when the transducer is driven at maximum power (Table 3.1). The pressure gain (Table 3.1 line 6) is the ratio between the maximum pressure in rat head and in water at the same voltage (considering peak positive pressures for a linear model). Table 3.2 lists the volumes of the focal region in rat brain and the standing wave ratio for each frequency.

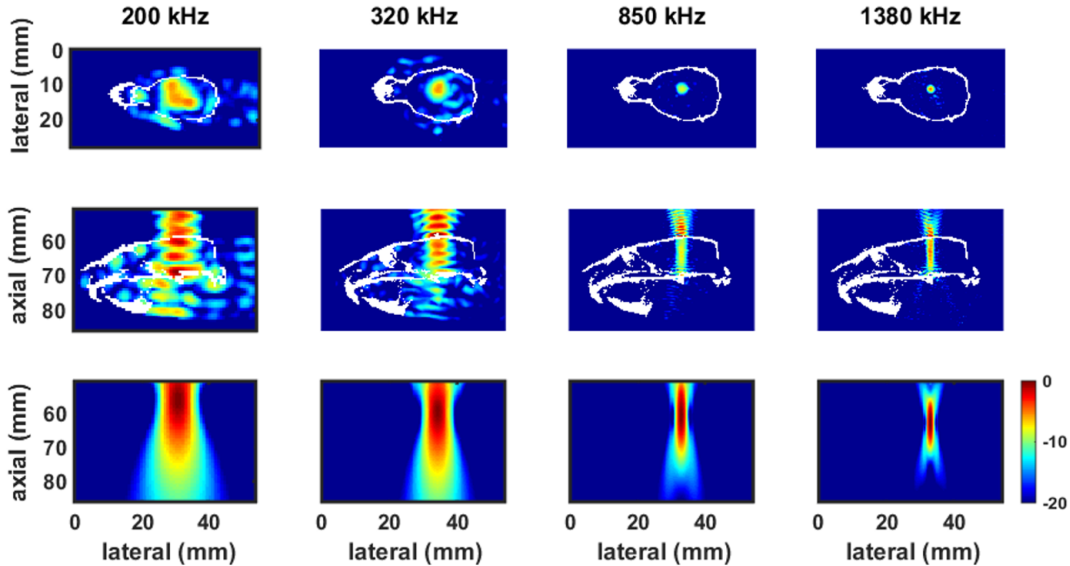


Figure 3.4: Pressure fields are normalized with maximum pressure over volume. The transducer is located so that the focal spot is inside the brain at $y=64$ mm.

Measurements and simulation of transmission through monkey skull flap The purpose of this series of measurements and simulations was to determine the acoustic parameters (sound speed, density, attenuation law) for use in the simulations in the entire monkey head, assuming that the piece of skull used for simulation model calibration and monkeys Y and L skulls, share the same properties. Given their differences of thickness and shape this is not true for transmission. Measurements of transmission through monkey skull were performed at the four frequencies 200,

320, 850 and 1380 kHz. The values of transmission, measured for different positions of the skull, are plotted for each frequency on figure 3.5. The 4 black dotted lines represent the results from simulations, where the focal point is translated by small lateral shifts ((0,0),(0,-0.5),(1,0),(-1,0) mm). The best match between experiment and simulation was found with the parameters listed in Table 3.3. With these parameters, the mean values of velocity and density are respectively 2263 m/s and 1572 kg/m³. As a comparison, reported mean values of velocity and density in human skull are 2240 m/s at 0.5 MHz [55, 42] and 1610 kg/m³ [216, 42]. Fry and Barger [55] also reported attenuation coefficients of 22 dB/cm at 1 MHz and 78 dB/cm at 3MHz. Assuming that $attenuation = 3 * absorption$ [166, 67], this leads to $\alpha_{0exp} = 7.3dB/cm/MHz^b$ and $b_{exp} = 1.16$.

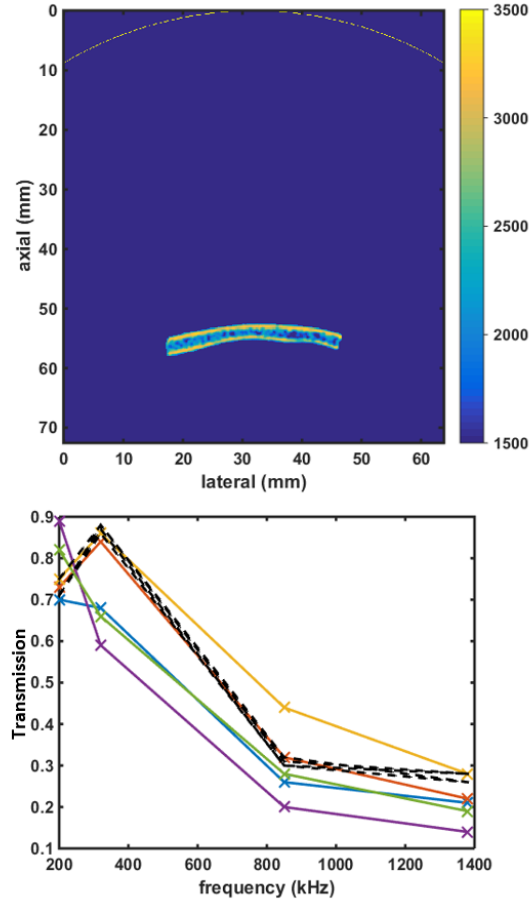


Figure 3.5: Top: Sound speed field (in m/s) for simulations in monkey skull flap with a representation of the transducer. Bottom: Measured transmission at different positions (colored lines) and simulated transmission (black lines) for different positions of skull flap as a function of frequency.

Table 3.3: Optimal acoustic parameters

ρ_{max}	c_{max}	β	α_0	b
2200 kg/m ³	3100 m/s	0.5	8dB/cm/MHz ^b	1.1

Table 3.4: Measured and simulated transmission values

	200 kHz	320 kHz	850 kHz	1380 kHz
Mean simulated transmission	0.72	0.87	0.31	0.27
Mean measured transmission	0.78	0.73	0.30	0.21
Standard deviation	0.11	0.11	0.06	0.05

The monkey skull flap exhibits heterogeneities, implying that changing its position in front of the transducer may result in variations in transmission. As the flap was held by a flexible piece of plastic, both its orientation and lateral position could be modified between two measurements. Interestingly, two behaviors were seen: for some positions, the transmission decreased with frequency (as expected, absorption being more important), but for others, ultrasound transmission was greatest at 320 kHz (orange and yellow lines). The maximum transmission at a given frequency could be due to a change in the orientation of the skull in regards to the main beam axis. Changing the orientation of the skull induces a shift in the apparent thickness. At 320 kHz, assuming that the mean velocity in the skull flap is $c \simeq 2000$ m/s (corresponding to $\lambda/2 \simeq 3mm$ in the skull), a 1.5 mm increase/decrease in thickness would change reflection from a minimum to a maximum. Given the curvature and heterogeneities of the skull flap, an incidence shift of a few degrees would eventually induce an apparent thickness shift of 1.5 mm. At 200 kHz, we can assume that the better transmission stability is due to a longer wavelength, causing the maxima and minima of reflection also to be extended. At 850 kHz and 1380 kHz ($\lambda/2 \simeq 1.2mm$ and $\lambda/2 \simeq 0.7mm$ respectively), it is likely that a maximum can switch to a minimum from one measurement to another. Indeed the transmission measured with our setup varies between 0.2 and 0.45 at 850 kHz and between 0.15 and 0.28 at 1380 kHz. In the simulations, only one behavior is observed, but one has to keep in mind that the orientation was kept constant.

Simulations in monkey brain The pressure gain at each frequency was estimated from 3D simulations in monkeys heads and were compared to free field values (Table 3.1, lines 4 and 5).

Figure 3.6 displays the normalized maximum pressure in decibels in monkey L (1st row), monkey Y (2nd row) heads and in free water (3rd row) for every frequency.

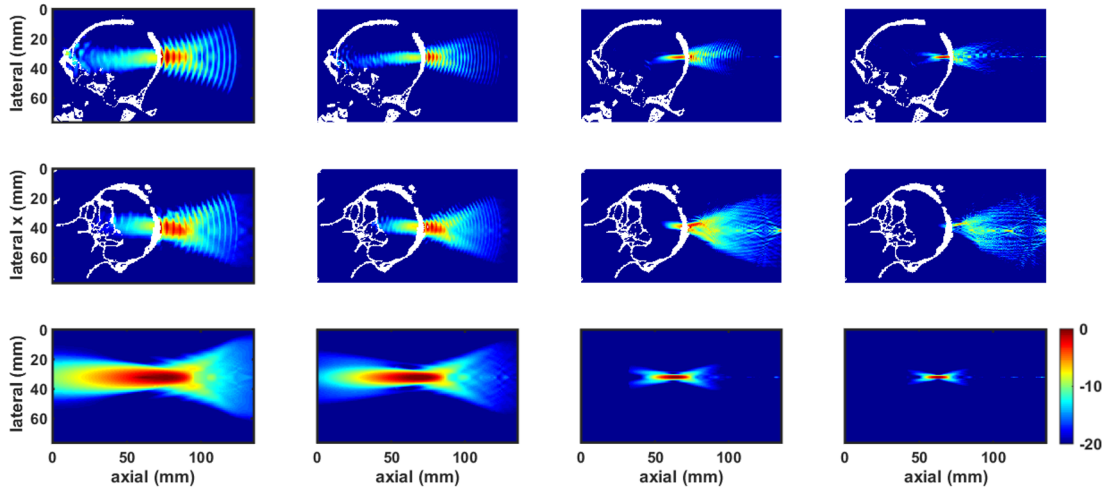


Figure 3.6: Maximum positive pressure over time in female monkey L (top), male monkey Y (middle) and free water (bottom), in decibels. Pressure fields are normalized to the maximum pressure over volume for each frequency and model. The transducer is positioned so that the geometric focal spot 7.7mm (monkey L) and 4.3 mm (monkey Y) deep in the brain.

3.4 Discussion

In this chapter we have demonstrated that our single element transducer driven by a 75 W amplifier could deliver more than 0.5 MPa in situ in both rat and macaque brains. Figure 3.7 summarizes the peak pressures that were obtained with our quadrifrequency transducer in the light of the peak pressures that have been previously reported for induction of neuromodulation. In the 250-690 kHz range, peak pressures up to 0.43 MPa in primate brain and 0.68 MPa in rodent brain have been reported. At higher frequencies (1.9 MHz), 1.79 MPa were reported to elicit a movement with a 70% success rate in rats. As can be seen in figure 3.7, such values are in line with the simulated maximum pressures in the rat and monkey brains with the quadrifrequency transducer. Moreover, the transducer was calibrated without any matching circuit; if needed, it will be possible to optimize the set-up by using one.

US

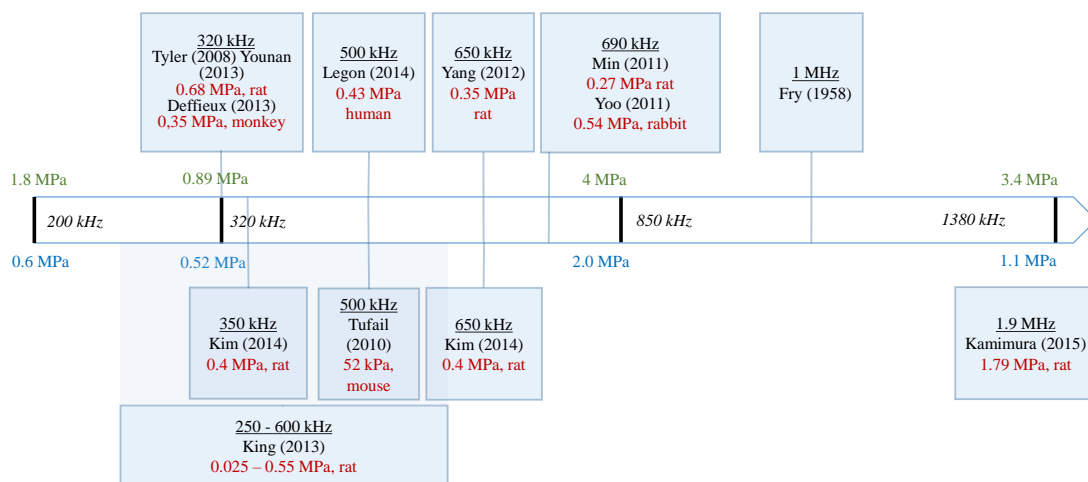


Figure 3.7: Schematic review of maximum pressures applied in brain to achieve neuromodulation. In green, above the arrow: simulated maximum pressure in the rat brain with the quadrifrequency transducer; in blue, below: simulated maximum pressure in the monkey Y brain with the quadrifrequency transducer.

Simulations in rat brain The importance of interference in the rat head, especially at low frequency should be noted (figure 3.4). As this depends on the geometry, the exact position of the standing waves, peaks cannot be assumed. Nevertheless, one can evaluate the area that is affected by them by assessing the estimated volume for half maximum pressure (-3dB) and for half maximum intensity (-6dB). At 200 kHz, almost the entire brain experiences significant ultrasound exposure, while at 1380 kHz, the half maximum pressure volume is 40 times smaller (Table 3.2). As a consequence, for a given peak pressure at the focus, the total energy dissipated in the brain decreases strongly with frequency. The standing wave ratio is 4 times smaller at the highest frequency compared to the lowest one. At high frequency, the rat head is large enough compared to the wavelength to form an efficient cavity for ultrasound (standing wave ratio is close to one). The two effects combined (larger affected area and more prominent standing waves at low frequency) may help to explain the reported greater efficiency of low frequencies for achieving neurostimulation [99, 101, 206, 222]. As the skull thickness (less than 1mm) is less than the wavelength at all frequencies, we can assume that the skull itself does not act as a Fabry Perot

cavity.

Simulations in monkey brain Results predict higher transmission through monkey L's skull than monkey Y's. The anatomical differences between these two specimens should be noted here: compared to monkey L (female), monkey Y (male) has a thicker skull (4.3 mm in the ultrasound propagation direction for monkey Y vs 2.5mm for monkey L) with more surrounding muscle (muscles have a 15.4mm width for monkey Y as compared to 4.9 mm for monkey L, along the direction of propagation). In monkey Y case, this means that the transducer is further from the skull and the focal spot to be less deep in the brain as a consequence. The fact that the pressure gain is lower for monkey Y at all frequencies is not in line with a reflection effect, but is more likely due to absorption: reflection depends on the thickness in a cyclic fashion [201], whereas absorption increases monotonically with the frequency. In our simulations, the cavity formed by the entire skull does not seem to play a significant role in comparison to the rat brain. One explanation could be that the size and geometrical shape of the primate head, combined with absorption, impede the formation of standing waves with such a focused transducer. We could not evaluate here the influence of the skull thickness and orientation alone on the pressure field inside the brain because the position of the transducer with respect to the head is kept constant in our simulations in monkey heads. Further work could be done to investigate their effects but this is beyond the scope of this chapter. The two monkeys are representative of animals that are commonly used in animal experimentation: they exhibit differences in terms of gender, age, weight, and skull thickness. Prediction of the in vivo pressure field could compensate for anatomical variability. This opens the possibility of adjusting the electrical power in order to compensate for anatomical idiosyncrasies across animals.

Linear simulation A linear simulation was used in this chapter. The validity of this assumption was tested through the monkey skull flap. Peak negative (PNP) and peak positive pressures (PPP) were recorded systematically for every output voltage. Figure 3.3 shows the typical linear behavior of both PNP and PPP with respect to the output voltage. There is a deviation in PNP of up to 11% at high voltages, causing differences in the slopes of PNP and PPP curves up to 10%. However this deviation occurs only at pressure levels greater 1.5 MPa, above the dose that is required for neuromodulation [36, 227]. When investigating pressure amplitudes higher than this

value, non-linear simulations would be needed.

Towards a multifrequency study of ultrasonic neuromodulation Many parameters are susceptible to have an impact on ultrasonic neuromodulation: peak pressure amplitude, ultrasonic frequency, pulse duration, duty cycle. . . Some are linked to each other. For example King et al [101] used a fix number of periods (40000 cycles) for all the frequencies they investigated. Consequently, different pulse lengths were used for each frequency. Based on the intra-membrane cavitation model [168], Plaskin et al suggest that the effects reported by King et al are “primarily a result of different pulse durations used experimentally”. In the light of these two studies, the quadrifrequency transducer proposed in this chapter should be used with a fixed duration for each frequency, while keeping in mind that the focal volumes are changing with the frequency.

3.5 Conclusion

We have proposed here a single transducer for multi-frequency studies. Calibration and simulation predict that it is possible to achieve high enough pressures to induce neuromodulation in rodents and primates at 200 kHz, 320 kHz, 850 kHz and 1380 kHz. All simulations highlight the importance of the head geometry. Standing waves significantly impact the pressure field in rat brain, although these have been neglected in most neuromodulation studies. Moreover, the differences between the monkey head specimens leads to significantly different pressure levels in the brain. Being able to investigate multiple frequencies with the same transducer and to adapt the power in order to induce similar pressure amplitudes in different animals’ brains opens up the path to more reliable neuromodulation studies. Other parameters than the frequency need to be optimized, based on measurements of the neuromodulation effects amplitude in animals or humans. Behavioral assessments [36] are currently used to evaluate neuromodulation effects, but animals need to be trained and results come from a large quantity of data, resulting in long and expensive studies. By contrast, physiological studies allow direct measurements of the brain response to a stimulus [110]. In the next chapter, electrophysiology is used to observe the activity of individual neurons of macaques after ultrasound stimulation during a visual task.

Chapter 4

Transcranial ultrasonic stimulation modulates single-neuron discharge in macaques performing an antisaccade task

4.1 Introduction

An improved understanding of the physiological action of FUS would enable fine tuning of protocols based on a known effect of the stimulation, which will improve the effectiveness of the technique, and thus accelerate clinical transfer. Here we report the feasibility of simultaneous recording of single neuron activity during FUS in an alert macaque performing an oculomotor task, the anti-saccade. This task, implying the repression of a reflexive ocular movement when a visual target appears and the generation of a voluntary movement towards the opposite side of the target, is particularly interesting in the case of patients affected by neurodegenerative diseases: it has been shown that the predictive, memory-guided component of the antisaccade is affected in PD patients [5, 50, 6]. As a consequence, the antisaccade latencies and amplitude alterations can be markers for the disease. Being able to track changes induced by FUS on neurons while performing such a

task will therefore be of great interest when investigating FUS potential as a treatment for neurodegenerative disease. A focused ultrasound transducer was positioned using a neuronavigation system (Rogue Research) to apply brief pulses of ultrasound in the frontal eye field (FEF) while neurophysiological recordings were performed in the supplementary eye field (SEF). Two discrete areas in frontal cortex are involved in generating saccadic eye movements in primates: the FEF and the SEF. Anatomically the FEF is reciprocally and bilaterally connected with the SEF [77, 126] and these connections appear to vary the least between primate species, suggesting that the most conserved functions of these regions may serve as a link for facilitating, planning of eye movements [162]. In both regions, eye movements can be evoked by direct electrical microstimulation with relatively low current [185]. Invasive intracortical recordings and/or stimulation techniques have been widely used to better apprehend the role of these two frontal areas, in combination with ocular motor measurements and mapping techniques, such as electrophysiological and fMRI recordings in non-human primates. Those approaches have provided causal evidence about the role of the FEF, with direct bearing on ocular motor and attentional function [19, 132]. More recently, the causal involvement of FEF in attentional orienting has been demonstrated [147, 146] as well as its ability to modulate different aspects of visual perception [44, 200] while indirect control and monitoring processes have been assigned to SEF functions [170, 171]. In order to examine the possible distant role of neuromodulation caused by FUS applied to a cortical brain region, we decided to target a cortical circuit controlling voluntary eye movement. Our short-term goal was to demonstrate the feasibility of combining real time focused ultrasound with single unit (SU) recordings in an alert macaque performing an antisaccade task. The combined approach of FUS and single unit recording has the potential to elucidate the mechanisms underlying the effects of focused ultrasound on the central nervous system. FUS and single unit recording could also be combined with 3D functional ultrasound imaging of brain activity, as recently demonstrated in alert animals in conjunction with EEG recordings [189, 127]. This will serve the causal non-invasive exploration of cognition in non-human primate models.

4.2 Materials and methods

Focused Ultrasound A single element ultrasound transducer (H115, diameter 64 mm, Sonic Concept, Bothell, WA, USA), geometrically focused to 64 mm, was used with a coupling cone

(C103, Sonic Concepts, Bothell, WA, USA) filled with degassed water. The transducer has four frequency resonances: 200 kHz, 320 kHz, 850 kHz and 1380 kHz. We chose the same main parameters (frequency and burst length) as our previous study [36] which had shown successful neuromodulation with the same transducer in monkeys: the ultrasound wave frequency was set to 320 kHz and 100 ms bursts of ultrasound were generated with a digital function generator, with rise and fall times set to 5 ms at the beginning and the end of the pulse, respectively (Handyscope HS5, TiePie engineering, Sneek, The Netherlands). A 75-Watt amplifier (75A250A, Amplifier Research, Souderton, PA) was used to deliver the required power to the transducer and the input voltage and current of the transducer were recorded using a voltage probe (HP9250, TiePie engineering, Sneek, The Netherlands) and a current probe (P6021, Tektronix, Beaverton, Oregon) connected to the HS5 card inputs. The recorded peak to peak voltage (V_{PP}) was $139 \pm 26V$ for monkey Y and $56 \pm 15V$ for monkey L. The calibration of the transducer inwater with a custom built heterodyne interferometer [86] led to a linear relationship between V_{PP} and peak negative pressure (PNP) in water of 5.68 kPa/V. The peak pressure in the brain of the monkeys was estimated by using 3D simulations of the ultrasonic field (see details below), taking into account the experimental geometry (0.41 ± 0.08 MPa for monkey Y and 0.24 ± 0.07 MPa for monkey L). For comparison, previous studies in human and non-human primates estimated peak pressures of 0.35 MPa [36] and 0.43 MPa [114]. The ultrasound was directly applied to previously shaved skin. A coupling cone filled with water ensured ultrasonic coupling between the transducer and the animal’s head. FUS was performed once every 5 trials with an unpredictable minimum duration of 3s between trials. There was therefore a pause of at least 10 s between ultrasound pulses. The corresponding overall spatial peak pulse average intensity (I_{SPPA}) was thus estimated to be $5.6 \pm 0.2W/cm^2$ and $1.9 \pm 0.2W/cm^2$ for monkey Y and L respectively ($I_{SPPA} = \frac{p^2}{2\rho c}$ with ρ and c approximated to ρ_{water} and c_{water}). For comparison, the FDA I_{SPPA} limit for ultrasound imaging safety guidelines is $190W/cm^2$ for adult transcranial imaging [52]. We emphasize here that we do not claim to be below FDA requirements as long pulses (100 ms, or 32000 periods) are used here, as compared to short pulses for imaging (one period for Bmode imaging, corresponding to 3ms at the frequency used here).

Experimental Setup The antisaccade paradigms and data acquisition were under the control of a computer running a Rexeno real-time data acquisition system [36].

Behavioral task Two captive-born macaques (*Maccaca mulatta*, “Y”, and “L”, one male and one female 11 and 8 years old and 17 and 7 kg respectively) participated in this study. The monkeys were paired-housed and handled in strict accordance with the recommendations of the Weatherall Report on good animal practice. Our experiments were approved by the Animal Health and Veterinary Medication Division of the Department of Public Veterinary Health, Nutrition and Food Safety of the French Ministry of Health (current renewal N° DTPP 2010e424). Monkeys had access to toys, mirrors and swings and also had visual, auditory and olfactory contact with other animals, and, when appropriate, could touch and groom each other. An institutional veterinary doctor constantly monitored their wellbeing and health conditions. Prior to participating in the study, both animals were periodically chaired, head-posted and trained to perform a series of tasks for a period of 6-12 months, until they became regular and proficient performers. Prior to the first experimental session, animals were specifically trained in an antisaccade (AS) task. Between 500 and 1000 ms after initial fixation onset on a brown central fixation stimulus and simultaneously to its disappearance (no gap), a red square appeared for 1000 ms at a 16° of visual angle to a rightward or leftward location (direction randomly selected). Monkeys were trained not to look at this peripheral target but instead, initiate as soon as possible a saccade in the opposite direction. After the saccade, the monkey received a reward if the saccade fell within a $10^\circ \times 10^\circ$ window centered at the mirror location of the visual target. Failure to trigger a saccade within 1000 ms of target onset cancelled the trial. The AS task was chosen since prior human and monkey FUS experiments have revealed prosaccade paradigms to be much less sensitive to single pulse FUS interference than antisaccades [36]. Trials were aligned on the appearance of the peripheral target.

Data analysis Eye movements were recorded with an infrared video eye tracker (Eyelink 1k, SR-Research, Ontario, Canada). Eye position was digitized and sampled at 1 kHz and stored for off-line analysis. All the analyses were performed on a personal computer with custom software written in the Python programming language. Eye position signals were low-pass filtered using a third order Savitzky-Golay filter (window: 41 ms). Eye velocity and eye acceleration were extracted from the Savitzky-Golay filter. Saccades were detected with a $30^\circ/\text{s}$ velocity threshold. For each cortical site tested with FUS, we used an online windows discriminator to isolate one neuron at a time for each recording. Offline cluster cutting (PCA) techniques were used systematically to confirm that action potential waveforms were produced by individual neuronal elements. Spikes

were sorted on-line using a box sorting method as a pair of time-level windows (Rasputin, Plexon Inc.). Offline examination of the sorting quality was systematically realized using a semiautomatic PCA calculation without restriction to a certain number of waveforms (Offline-Sorter Plexon Inc). Following the extraction of the spike time, we evaluated the average firing rate of each neuron (and the confidence interval of the average) using bootstrapping techniques on the computation of the spike density function [127]. The principle of bootstrap is to randomly select trials without replacement from the larger dataset (here control trials) and with replacement in the smaller dataset (FUS trials). This random selection is made N times where $N = 50 * \text{sample size of the smaller dataset}$ as described by Daye and colleagues [35]. The effect of FUS between functional cell types was compared using the chi-squared test.

Surgical procedure The surgical procedures for the titanium head-post implant were as previously described [36]. Each animal was deeply anaesthetized using ketamine hydrochloride (5 mg/kg i.m.) for initial sedation before induction with 2-4% isoflurane gas, which was then maintained during surgery. Pain medication was given prior to surgery and routinely given after surgery. Implanted head posts (7.1 mm internal diameter) (Part 6-FHP-X2F, Crist Instrument, Hagerstown, MD, USA) were designed to mate with a head-post holder (Part 6-FHB-S2B, Crist Instrument, Hagerstown, MD, USA). SEF Recording chambers were placed according to stereotactic coordinates (AP: 26; ML: 0) and MRI scans. The craniotomies were performed under deep anesthesia with ketamine hydrochloride (5 mg/kg i.m.) for initial sedation, and induction and maintenance with 2-4% isoflurane gas. Pain medication was given prior the surgery and routinely given after surgery.

Neurophysiological data acquisition and analysis For single unit recordings, multiple tungsten microelectrodes (FHC, 8-10 $M\Omega$) were introduced through guide tubes and independently positioned with a custom-made stepper-motor microdrive. The recordings were made on a MAP system (Plexon Inc.,TX, USA), storing spike times with 25 μ s resolution. Online discrimination based on wave shape parameters was used to select a single neuron on each independent recording electrode channel. Respectively 39 and 46 neurons were recorded in monkey Y and L. All isolated neurons recorded were kept for the analysis. All sets of recordings consisted in more than 386 and 400 valid trials for monkey Y and L respectively.

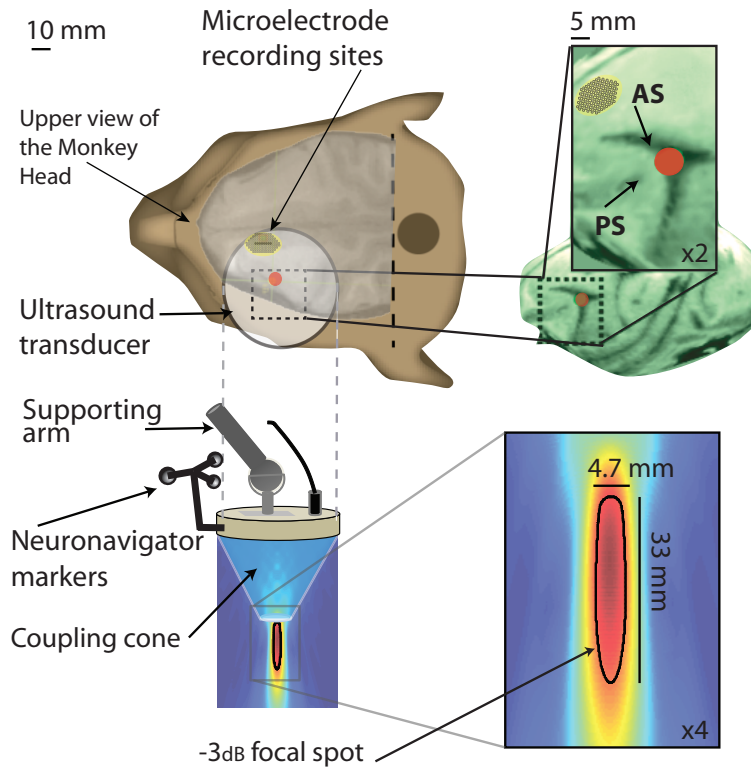


Figure 4.1: The ultrasonic transducer was attached to a neuro-navigation module that allows co-registration of digitized external coordinate systems with the internal MRI coordinate system. This system makes it possible to direct an attached transducer in real-time to functional and anatomical target regions of the brain (Rogue Research). Using this co-registration, the cigar-shaped focal spot of FUS was placed over the left FEF (red spot). For each animal the FEF was identified with anatomical landmarks (arcuate sulcus AC, and principal sulcus PS). A coupling cone filled with water ensured ultrasonic coupling between the transducer and the animal's head. The neurophysiological recordings were performed in the left SEF area (yellow spot) through a recording chamber and grid adaptor.

FEF targeting with FUS Targeting of the FEF with the FUS transducer was performed using a neuro-navigator tool (Brainsight, Rogue Research, Montreal, Canada). An MRI dataset (structural T1) was acquired for each monkey with an attached MR fiducial marker array. The FEF target was manually registered once and used for all sessions. Prior to each session, the position of the fiducial marker array was manually registered to a position sensor serving as a reference and fixed to the chair. In a second step, the focal spot of the FUS transducer, materialized using a 3D printed piece, was registered using a tracked pointer to a second position sensor, which was fixed behind the transducer. Before each session, the transducer, supported by a mechanical arm

Table 4.1: Acoustic parameters

	Air	Water	Tissue	Max
Velocity (m/s)	340	1500	1560	3100
Density (kg/m ³)	1.2	1000	1030	2200

Table 4.2: CT parameters

	Monkey Y	Monkey L
HU_{max}	3300	3000
HU_{tissue}	1035	1031

(Rogue Research, Montreal, Canada) was then manually moved until the focal spot was aligned and positioned over the predetermined FEF target. The arm was then locked for the rest of the session.

Numerical simulations Acoustic density and velocity maps were reconstructed from CT scans of both monkeys' heads (Philips Brilliance 64 CT Scanner, Voltage: 120 kV, Intensity: 350 mA; FilterType: 'D'). The brain, skin and muscle tissue was considered as a homogeneous medium and skull was modeled as a heterogeneous model by using a linear conversion from Hounsfield units (HU) to density and velocity of the skull (Chapter 3).

The power law model for attenuation is $abs = \alpha\Phi^\beta$ where the porosity Φ is defined by $\Phi = \frac{\rho_{max} - \rho}{\rho_{max} - \rho_{water}}$ in the skull [9]. α and β were experimentally determined by transmission measures and simulations to a monkey skull flap: the best match was found with $\beta = 0.5$ and $\alpha=8.0$ dB/cm/MHz^{1.1}, leading to $\alpha=2.3$ dB/cm at 320 kHz. The acoustic parameters are summarized in Table 4.1 and 4.2. CT images were acquired with the smallest field of view to obtain the best possible resolution in the transverse plane: 0.358 mm and 0.136 mm for monkey Y and L respectively. The acoustic density and velocity 3D maps were then subsampled to respectively 0.358 mm and 0.407 mm isotropic resolution for monkey Y and monkey L, which gave a ratio of 13.6 and 12.0 pixels per wavelength in tissue at 320 kHz.

The pseudo-spectral method-based software k-Wave [32] was used to perform the linear acoustic simulation through the water cone, skull and brain with the same geometry used in vivo with the neuro-navigator positioning. The head was modeled as immersed in water, given that, in that

setup, tissue/air interfaces are unlikely to play a significant role compared to skull/tissue interfaces. Not considering the air medium, whose impedance is much lower than water, significantly reduced the computation time. To limit the computation time, the total simulation duration was limited to $150\mu s$, which was sufficient to reach a steady-state. For each simulation, the pressure field was stored in three dimensions and in a full volume including the FEF for all time steps. Time profiles of the acoustic pressure were extracted at the geometric focus and at the point of maximal pressure amplitude over time. Maps of the in-situ time peak pressure at steady-state were also estimated by taking the time peak of the pressure field at each pixel in 3 planes (orthogonal to, or including the transducer direction), centered on the geometric focus. As the muscular tissue surrounding monkey Y's skull was much thicker than monkey L's (respectively about 16 mm and 5 mm), a 1 cm transducer's pressed into the tissue was taken into account in the simulation. This value was set based on the actual in vivo positioning of the transducer, based on the neuro-navigator guidance for FEF targeting. The calibration of the transducer in water showed a linear relationship between peak to peak voltage and peak negative pressure in water of 5.68 kPa/V. Simulations were first performed in water without the skull, in order to normalize the simulations based on actual pressure measurements in water. Table 4.3 summarizes the results of the simulations.

4.3 Results

The goal of our study is to show that FUS and single unit recordings can be combined to probe the interactions between two reciprocally-connected distal bilateral areas. First, we present how FUS applied to FEF affects the neural activity of a SEF neuron. Then we extend these analyses to the whole neuronal population that has been recorded to investigate the overall effect of FUS on a distal connected area.

Table 4.3: Estimations of peak pressure in monkeys' brains

	Monkey Y	Monkey L
VPP	139 ± 26 V	56 ± 15 V
Equivalent PNP in free water	0.76 ± 0.08 MPa	0.31 ± 0.14 MPa
Simulated steady state PNP in FEF	0.50 ± 0.09 MPa	0.33 ± 0.09 MPa

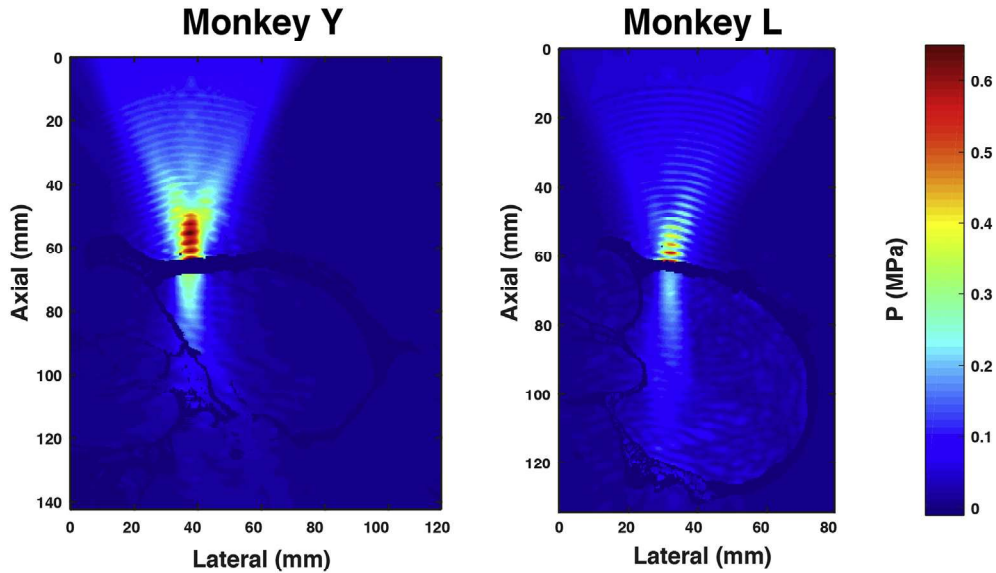


Figure 4.2: Peak negative pressure (MPa) in the brains of monkey Y (left) and L (right) from simulations, taking into account the respective voltage applied to the ultrasonic transducer ($139 \pm 26V$ and $56 \pm 15V$).

Simulation of ultrasonic pressure field in the brain The voltage applied to the ultrasonic transducer was respectively equal to $139 \pm 26V$ and $56 \pm 15V$ for monkey Y and L. As shown in figure 4.2, female monkey L had a smaller head than male monkey Y. 3D numerical simulations of the ultrasound propagation were conducted in order to investigate the ultrasound field in the two different monkey brains while taking into account head geometry, and the reflection, refraction and absorption associated with the full skull cavity and head geometry, (Table 4.3). A linear simulation model was used in which the acoustic pressure was proportional to the applied voltage. In water, the peak pressure was found to be 2.5 times higher with monkey Y's settings than monkey L's. Nevertheless, the peak pressure in the FEF is only 1.7 times higher for monkey Y. This is most probably due to anatomical differences such as skull thickness, skull density, skull geometry and frontal muscular tissue thickness (Table 4.3 and figure 4.1). Owing to the different acoustic pressures used between the two animals, as well as the compounding effects of differences in head size, skull thickness, the recorded neuron data from each animal was analyzed separately and is quantified in figure 4.4 (top panel for monkey Y and middle panel for monkey L). To minimize the difference between peak pressure in the brain between the two animals the voltage was reduced to 139V for monkey Y (compared to [36]). Behaviorally, the latencies were significantly modulated

by FUS for monkey L across sessions ($n = 46$, $p < 0.01$) and marginally modulated for monkey Y ($n = 39$, $p = 0.08$).

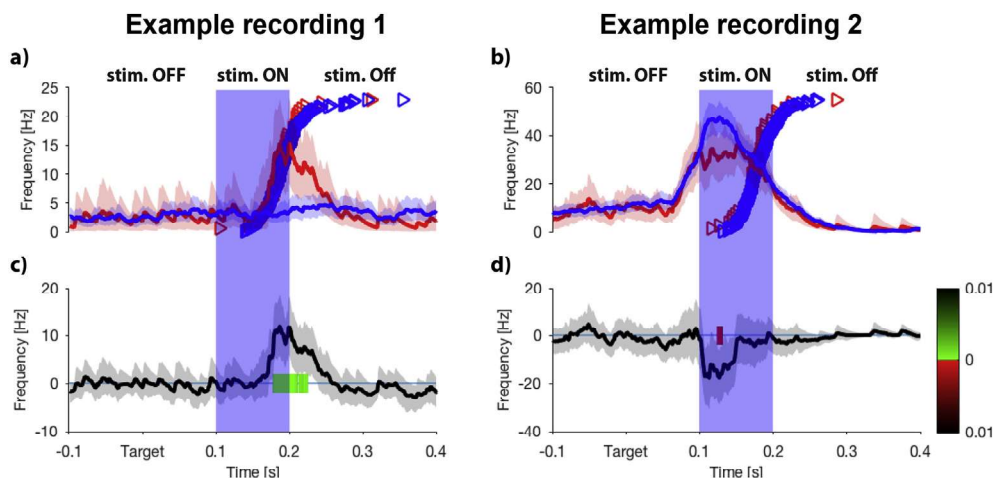


Figure 4.3: Average recorded spikes per seconds with (red lines) or without (blue lines) single pulse FUS. The two columns represent two examples of neurons showing significant change of activity following FUS. Vertical blue shaded area represents the time interval of FUS. Origin of time corresponds to the appearance of the visual stimulus. (a) Example from a neuron showing an increase of activity with FUS. Triangles represent ranked saccadic latencies for each trial respectively with (red) or without (blue) FUS. (b) Example from a single neuron showing a decrease of activity with FUS while the monkey is preparing a saccade opposite to the target. (c and d) Bootstrap difference of the control vs FUS condition (grey). Significant differences between FUS and control trials are respectively represented by a red (FUS < Control trials) or green (FUS > Control trials) line ($p < 0.01$). These two neurons were selected for illustration because the FUS elicited activation of diverse neuronal elements.

Typical trials Figure 4.3: Recordings of neuronal spikes activated by single pulse FUS. (a) Example raw data from 41 trials with FUS (red) and 179 without stimulation (blue). (b) Bootstrap difference of the control vs. FUS condition at the same site ($p < 0.01$). These data were selected for illustration because the FUS elicited activation of diverse neuronal elements. The triangles represent latencies for each trial respectively for FUS (red) or no stimulation (blue) trials. The average firing activity across trials are shown during control trials (blue line) and following FUS (red line) (Figure 4.3 a and b). Red and blue shaded areas represent the 99% confidence interval respectively for average activity. The time course of the difference between these two conditions (control and FUS) is shown in figure 4.3 c and d. The black line and shaded areas represent the 99% confidence interval for activity difference when comparing FUS and control trials. The blue

vertical rectangles represent the time interval during FUS stimulation (100 ms) where time $t = 0$ corresponds to target presentation. We consider the difference between FUS and control conditions activity as statistically different from zero when $p < 0.01$ and the duration of the difference is greater than or equal to 5 ms. The green (increase in activity) or red (decrease in activity) segments in figure 4.3c and d highlights these significant time periods. In the stimulation condition, figure 4.3a shows that the activity started to increase 67 ms after FUS onset and became statistically significantly different from the control condition 78-111ms and from 113 to 125ms after FUS onset (shown by the first significant segment in figure 4.3b). The neuron reached a peak activity of 10.1 Hz (with 99% confidence interval (CI) of 15.48 and 21.61 Hz) 99 ms after stimulation onset compared to 2.1 Hz (with 99% CI of 5.45 and 9.53 Hz) during control trials. For this neuron, this level of activity was maintained during the stimulation. After stimulation ceased, the neuron activity decayed back to the activity observed during the control condition. As shown on the right panel (Figure 4.3 b,d), a decrease in activity in the SEF was also observed following FUS in the FEF. The activity of this neuron starts to increase before FUS and appeared to be significantly reduced from 24 to 41 ms after FUS onset.

Population activity Figure 4.4a and b illustrates changes in the activity of the population of the neurons recorded in the two animals. Significant periods of neuromodulation were observed for 39% and 41% of the recorded neurons respectively for monkey Y and L. A transient increase of activity for 53% and 47% of neurons recorded respectively in monkey Y and L reveal the perturbation induced by FUS. For 47% and 53% of neurons respectively in monkey Y and L the perturbation was revealed by a significant decrease in activity. Among all recorded neurons the effects of FUS parameters are presented chronologically during the series of experiments for the 39 and 46 neurons respectively recorded in monkey Y and L. Each horizontal gray line represents a neuron. As in figure 4.3, the time origin corresponds to target presentation, and shaded gray areas represent the stimulation period. The colored lines in figure 4.4 highlight the periods during which the neuronal activity differed significantly between FUS and control trials. The color of each segment represents the p-value of the difference between FUS and control trials. Green (red) colored segments correspond to excitation (inhibition). Figure 4.4a and b shows that many of the recorded neurons had their activity modulated (increased or decreased) when FUS was applied in both monkeys. Overall, our analysis demonstrates a significant effect on SEF neuronal activity when

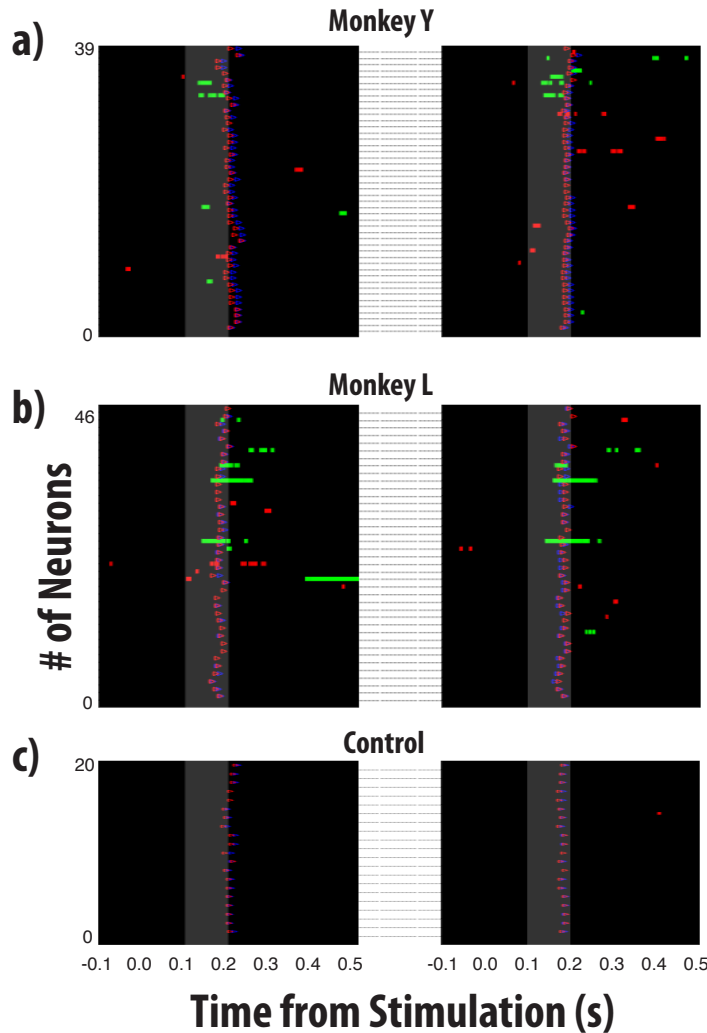


Figure 4.4: Modulation while comparing FUS and control trials ($p < 0.01$) in the population of recorded neurons in the two animals. Significant differences between FUS and control trials are respectively represented by a red (FUS<Control trials) or green (FUS>Control trials) line ($p < 0.01$) for leftward (left panel) or rightward (right panel) direction of eye movement. Vertical gray shaded area represents the time interval of FUS. Origin of time corresponds to the appearance of the visual stimulus. Top panel population of 46 for Monkey L. Middle panel: 39 neurons respectively for Monkey Y. Bottom panel of 20 neurons while FUS is being applied to the control region. Note that the significant periods of neuro-modulation are drastically reduced (if present at all) during the control condition. All isolated and recorded neurons were analyzed and no selection was made to avoid sampling bias due to cell types.

FUS was applied to the FEF. Comparison between cell types based on their functional properties [171, 197] did not reveal any significant susceptibility (respectively χ^2 , $p=0.39$ for monkey Y and χ^2 , $p=0.37$ for monkey L). For monkey Y: of 39 neurons, 0 of the 3 of fixation; 5 of the 11 of

movement; 9 of the 18 non-specific; 1 of the 7 post-saccadic; and 0 of 0 visual neurons showed a significant neuro-modulation induced by FUS. For monkey L: of 46 neurons, 2 of 2 of fixation; 2 of 9 of movement; 13 of 26 non-specific; 1 of 7 post-saccadic; and 1 of 2 of visual neurons showed significant neuro-modulation by FUS. In contrast to FUS stimulation applied to the FEF, FUS applied to control extra-striate visual cortex did not significantly generate changes in activity rates (Figure 4.4c). Only one of the 20 recorded neurons did show a brief significant period of modulation when the control region was stimulated compared with 39 and 41% of significant neurons showing modulation when the FEF was stimulated in the same animal (monkey L). We verified whether the observed change of activity during the stimulation could be explained by a modification of the spikes isolation of the neuron due to the ultrasound stimulation. We did not observe any difference of spike waveform when comparing FUS and control conditions (Figure 4.5), demonstrating that the pattern of activity of our neuron observed during stimulation trials is not an artifact related to a propagation of the ultrasound wave to the recorded region (CI: 99%). At the population level none of the recorded neurons show a significant modulation of waveforms above the confidence interval (Figure 4.6).

4.4 Discussion and conclusion

FUS techniques have been used to produce increased neuronal firing rates in the peripheral and central nervous system in vitro or in anesthetized preparations [101, 207, 205, 99, 150, 142]. Suppression of activity following FUS has also been reported [224, 143, 100], as well as more subtle changes in excitability [145]. However, non-invasive exploitation of the concomitant effects of transcranial ultrasound stimulation (FUS) in alert animals would have many applications in neuroscience. However, and despite the increasing volume of work done with the emerging of FUS, there is limited knowledge concerning its effects on neurons. Investigating neural connectivity - how two connected regions interact by stimulating one area and recording in another - is the most straightforward application. Our approach was to perform the feasibility of such study by studying the interaction within the oculomotor regions of the frontal lobes in awake primates performing an antisaccade task. By combining FUS with traditional electrophysiology, the ability to study the mechanisms of FUS is vastly expanded, and paves the way for research and development needed to usher in the next generation of noninvasive FUS technologies and treatments. In particular, the

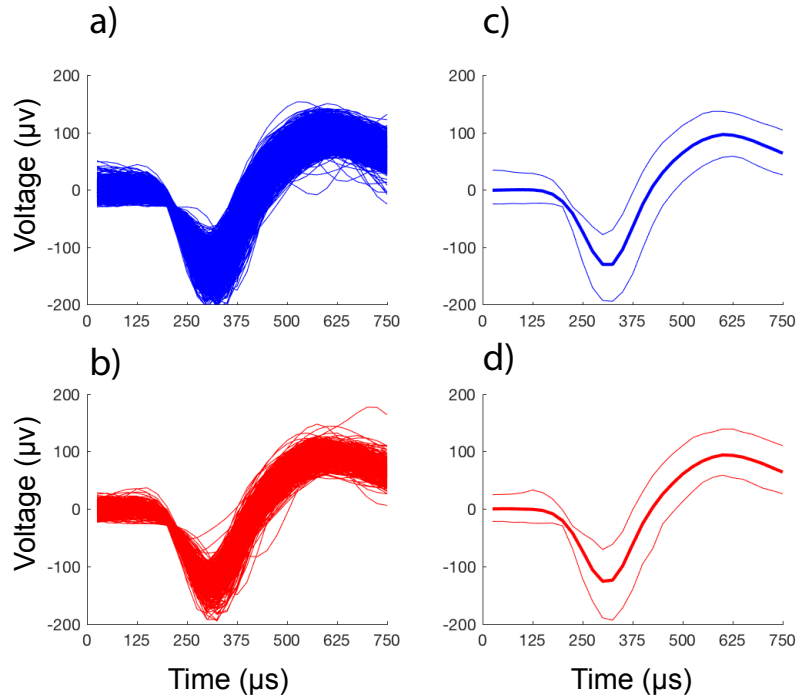


Figure 4.5: Spike waveforms with and without FUS. A) All spike waveforms from a representative session without stimulation (blue thick line d) B) median \pm CI 99% (blue thin line d). C) All spike waveforms from a representative session with focused ultrasound stimulation (red thick line d) B) median \pm CI 99% (red thin line d).

study opens the door for further parametric studies for fine-tuning the ultrasonic parameters. The ultrasonic effect could indeed be quantified based on the direct measurement of the intensity of the modulation induced on a single neuron in a freely performing animal. In this work the recorded region (SEF) was different from the stimulated region (FEF) and despite the fact that these two regions are connected, not each FEF neuron projects to an SEF neuron. The fact that FUS can induce an effect in a connected brain region re-enforces the potential uses of this technique to modify network activities. Further studies are required to better understand the mechanisms of action of FUS. Potentially, clinical use of FUS might be similar to transcranial magnetic stimulation (TMS) and could thus be valuable in the treatment of depression [64], movement disorders [113, 72], or patients suffering from perceptual disorders [117]. The development of ultrasonic neuro-modulation is largely motivated by future therapeutic applications. A critical issue is to increase the duration of its effects, which were limited to less than 10 minutes in previous studies. In the next chapter,

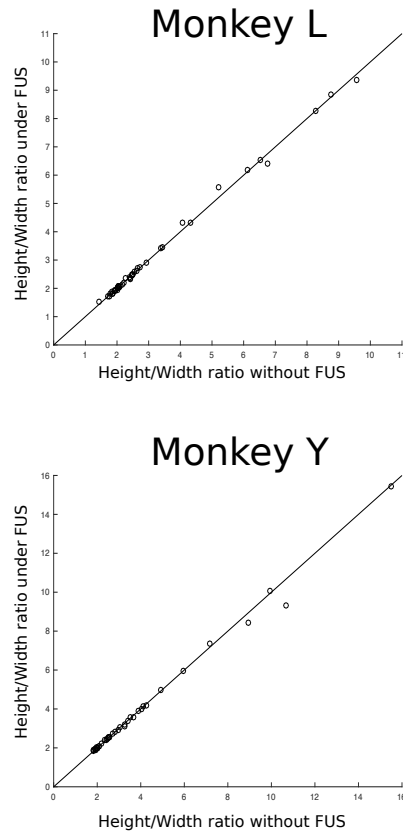


Figure 4.6: Height/Width ratio of spike waveforms with and without FUS for all neurons recorded in monkey L and monkey Y respectively. Note that none of the recording show a significant deviation while comparing FUS and no FUS trials ($p > 0.6$).

a modified (longer) ultrasound sequence is introduced to increase the modulation duration. It was tested on macaques performing a visual task.

Chapter 5

Repetitive Transcranial Focused Ultrasound Stimulation

5.1 Introduction

In spite of the several advantages (non-invasiveness, high spatiotemporal resolution, access to deep brain structures) that focused ultrasound-induced neurostimulation has compared to current non ultrasonic neurostimulation techniques, the duration and strength of the effect after TUS could clearly be identified as a limiting factor when exploring its therapeutic use [36]. With the exception of Elias group's work on swine [33], TUS effects have been found to be transient, inducing a brief change in a motor command, sensation or electrical activity within a few hundreds of milliseconds after applying the ultrasonic stimulation. Our group's previous work on neuronal discharge response in macaques [215] found that a 100ms-long pulse induced a transient effect from 113 to 125ms after TUS onset. By applying an extended 40s pulse with a 43.7% duty cycle, Dallapiazza *et al.* [33] observed a substantial and sustained decrease in neuronal function for several minutes in anesthetized swine. Since a sustained effect of ultrasound on brain function opens the door to a wide range of clinical applications, it would be of great interest to achieve durable neurostimulation on awake animals. Here we present a detailed account of the effects of repetitive transcranial ultrasonic stimulation (rTUS) on the oculomotor cortex regions of macaques while the animals were performing an antisaccade (AS) task, described in chapter 4. We used

focused ultrasound on macaque frontal brain areas to interfere with the activity of AS preparatory processes driven by spatial visual stimuli. It has been suggested that, during the AS task, inhibition of reflexive misdirected saccades is due in part to the SEF, whereas triggering of the intentional, correct AS depends upon the FEF [186, 184]. Our short-term goal was to demonstrate the feasibility of offline sustained focused ultrasound experiments in an awake and freely performing non-human primate.

5.2 Materials and Methods

Repetitive transcranial focused ultrasound A single element focused ultrasound transducer (H115, Sonic Concept, Bothell, WA, USA; central frequency 250 kHz, diameter 64mm, FD # 1) was used in those experiments. A coupling cone (C103, Sonic Concepts, Bothell, WA, USA) filled with degassed water was placed between the transducer and the animal head. The transducer was fixed on a mechanical arm with four rotation axes (Viewmaster LCD, Osmond Ergonomics, Wimborne, UK) to enable flexible positioning of the transducer over the head. A thin layer of echographic gel (Aquasonic 100, Parker Laboratories Inc., Fairfield, NJ, USA) was applied to the skin and the membrane of the coupling cone to ensure acoustic coupling.

The ultrasound frequency was set to 320 kHz. The pulse duration was 30 ms, the pulse repetition frequency (PRF) was 10Hz and the total sonication time was 20s. The signal was generated by a TiePie generator (Handyscope HS5). A 75-watt amplifier (75A250A, Amplifier Research, Souderton, PA) was then used to deliver the required power to the transducer and the input voltage of the transducer was monitored using a voltage probe (P6139A, Tektronix, Melrose, MA) connected to a TiePie oscilloscope. The amplifier gain was set to deliver an output voltage $V_{out}=173V$ peak-to-peak, corresponding to a pressure amplitude of $0.76MPa$ in water (calibrated with the interferometer described in chapter 3 [30]).

In chapter 3, a simulation-based value of the transmission was used. Here, the transmission of the pressure through the degassed primate skull was assessed at 7 different points arbitrary chosen on the skull. The transmission ratio was found to be $58\% \pm 8\%$ (standard deviation). The in-situ pressure delivered to the monkey brain transcranially was subsequently estimated at 0.44 ± 0.06 MPa. The equivalent mechanical index (MI) value is 1.3 with an intensity spatial peak pulse average (I_{SPPA}) of $19W/cm^2$ in free water. Those values are attenuated to $MI = 0.8 \pm 0.1$ and

$I_{SPPA} = 6.5 \pm 1.8W/cm^2$ respectively inside the primate skull. By taking into account the pulse duration and PRF (respectively 30 ms and 10Hz, corresponding to a 30 % duty cycle) during the neurostimulation sequence, the intensity spatial peak time average (I_{SPTA}) is estimated to be $5.7W/cm^2$ in free water and $1.9W/cm^2$ inside the primate skull.

Task The AS task is described in chapter 4.

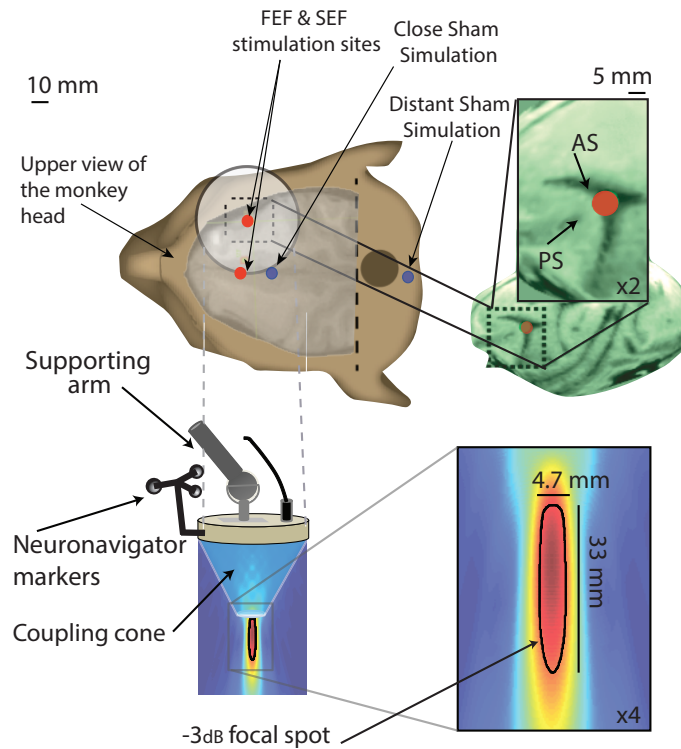


Figure 5.1: The ultrasonic transducer is manually positioned guided by neuro-navigation system (Rogue Research). The cigar-shaped focal spot targets the FEF right or SEF in the left hemisphere of the cerebral cortex (red spot) is displaced through the MRI scans obtained for each animal. A coupling cone filled with water ensures ultrasonic coupling between the transducer and the animal’s head. Sham stimulation was performed by placing the transducer over the motor or primary visual cortex (blue dot). The behavioral recordings were performed during seven blocks of 100 trials for each individual session. Forty sessions were recorded for each monkey.

Experimental protocols Two captive-born male macaques, *Macaca fascicularis* “A” and *Macaca mulatta* “B” (both 11 years old and respectively 8 and 13 kg) participated in the study. The protocol and the surgical procedure were identical to the previous study (chapter 4). In this study,

animals performed a total of 40 sessions (10 stimulated sessions and 10 non-stimulated sessions for each region of interest ‘ROI’ or control region). Each experiment session contained, after one non-recording warm-up block, a total of 7 blocks of 100 antisaccades (50 each side). The rTUS stimulation was delivered after the first block had been completed. In order to keep conditions across all experimental sessions as similar as possible, the transducer was placed on the targeting region in both stimulated and non-stimulated sessions. The FEF, SEF, cortical motor and visual fields were targeted with a neuro-navigator (BrainSight, Rogue Research, Canada) coupled with a transducer guided by an MRI. For macaque “B” the ROI was set to the FEF and the control region on the visual cortex. For macaque “A” , due to an important mass of muscle, the ROI was set to the SEF and in order to have a control region closer to the ROI we have chosen motor cortex. SEF, motor and visual cortex spots were defined on the MRI according to stereotaxic coordinates. The FEF was classically identified as the fundus of the arcuate sulcus.

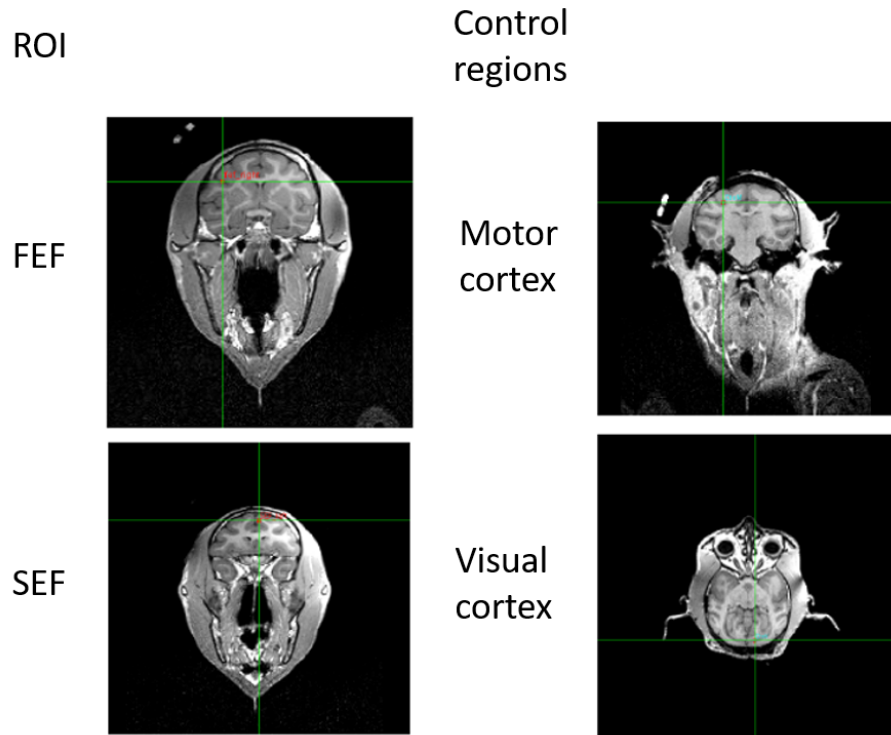


Figure 5.2: rTUS stimulation sites and neuronavigation. FEF, SEF, motor and visual cortex as rTUS neuronavigation targets on the cortical surface (on the T1 MRI scan of a representative animal). The green cross indicates the transducer target.

Thermal modeling The propagation of focused ultrasound was simulated in an entire monkey head to obtain the pressure amplitude and spatial distribution at steady state. The simulations were performed using a k-space pseudospectral method-based solver, k-Wave [32]. 3D maps of the skull, brain, and tissues were extracted from a monkey CT scan (0.14 mm resolution). Soft tissues were assumed to be homogeneous, with acoustic values close to those of water ($\rho_{tissue} = 1030kg/m^3$ and $c_{tissue} = 1560m/s$). In the bone, a linear relationship between the Hounsfield Units (HU) from the CT scan and the sound speed, as well as the density, was used. The power law model for attenuation is $abs = \alpha\Phi^\beta$ where the porosity ϕ is defined by $\Phi = \frac{\rho_{max} - \rho}{\rho_{max} - \rho_{water}}$ in the skull [9]. The attenuation coefficient for the acoustic propagation α_1 depends on the frequency: $\alpha_1 = \alpha_0 f^b$. We set the parameters to $\rho_{max} = 2200kg/m^3, c_{max} = 3100m/s, \beta = 0.5, \alpha_0 = 8dB/cm/MHz^b, b=1.1$ [30]. The attenuation coefficient in bone accounts for both absorption and scattering. The propagation simulation was performed at 250 kHz with a $150\mu s$ -long pulse signal (enough to reach a steady state) and a 0.41mm pixel size. The transducer was modeled as a spherical section (63mm radius of curvature and 64mm active diameter). The simulated pulses were spatially apodized ($r=0.35$) on the spherical section. Ultrasound propagates first through the water-filled cone before entering the head, since the geometrical focal point is located below the surface, inside the brain. The pressure amplitude map was then rescaled to a maximum pressure of 0.44 MPa in the brain, corresponding to the estimated experimental value.

The thermal modeling is based on the bio-heat equation [161]:

$$\rho C \frac{\partial T}{\partial t} = \kappa \nabla^2 T + q + w \rho_b C_b (T - T_a)$$

where T, ρ, C, κ and q are the temperature, density, specific heat, thermal conductivity and rate of heat production respectively. Heat production is defined as $q = \alpha_{abs} \frac{PPP^2}{2\rho c}$, α_{abs} being the absorption coefficient. According to [42] κ is set to $0.528W/m/K$ in soft tissue and $0.4W/m/K$ in the skull and C is set to $3600J/kg/K$ in soft tissue and $1300J/kg/K$ in the skull. In the tissue, the absorption coefficient was set to $\alpha_{abstissue} = 0.21dB/cm/MHz^b$ [67].

In the skull the longitudinal absorption coefficient is proportional to the density with $\alpha_{absmax} = \alpha_0/3 = 2.7dB/cm/MHz^b$ [166]. The last term corresponds to the perfusion process: w, ρ_b, C_b and T_a correspond to the blood perfusion rate, blood density, blood specific heat and blood ambient temperature respectively. These parameters are assumed homogeneous in the brain, although a

more detailed description of the brain cooling processes can be found in the literature [213]. The perfusion parameters are taken from Pulkkinen et al [176]: $w = 0.008s^{-1}$; $\rho_b = 1030kg.m^{-3}$; $C_b = 3620J/kg/K$ and $T_a = 3^\circ C$.

The bioheat equation is solved by using a 3D finite-difference scheme in Matlab with Dirichlet boundary conditions. Initial temperature conditions were $37^\circ C$ in the brain, skull and tissue, and $24^\circ C$ in the water coupling cone. Simulations were run over 2 minutes pre-sonication, followed by 40 seconds of sonication and 5 minutes cooling post-sonication, according to the experimental procedure.

5.3 Results

Following 20s of rTUS, subsequent antisaccade (AS) latencies were significantly modified compared to the control condition. The effect was maintained for up to 25 minutes after rTUS. After 25 minutes the saccade latencies returned to normal and were indistinguishable from saccades recorded in the control condition. Our study demonstrates for the first time the feasibility of using repetitive focused ultrasound stimulation to modulate behavior in awake non-human primate brain for several minutes. The AS latency for each individual trial was calculated as the time between stimulus presentation and the onset derivative of the eye saccade velocity reaching a speed of $30^\circ s^{-1}$. The AS latencies were averaged for each individual block of trials before and after focused ultrasound (rTUS session) and compared to similar chronological blocks without stimulation (no-rTUS session) with a Wilcoxon rank sum test.

Repetitive stimulation over FEF and SEF As shown in figure 5.3 (left), 20s of rTUS directed at the FEF on monkey B almost exclusively affected ipsilateral AS latencies. More specifically, ipsilateral mean AS latencies with rTUS stimulation to the FEF were significantly faster compared to non-stimulation. Post stimulation blocks were up to 10.82ms (sem=2.58 ms) faster than similar blocks with no stimulation (Wilcoxon rank sum test, $p < 0.001$). This effect persisted for some time, taking 25 minutes for the oculomotor behavior to return to baseline and be indistinguishable from the control condition. Importantly, the effects of 20 seconds of rTUS over control visual cortex on monkey B did not show any significant effect on AS latency (Wilcoxon rank sum test, $p > 0.1$) compared to the non-stimulation.

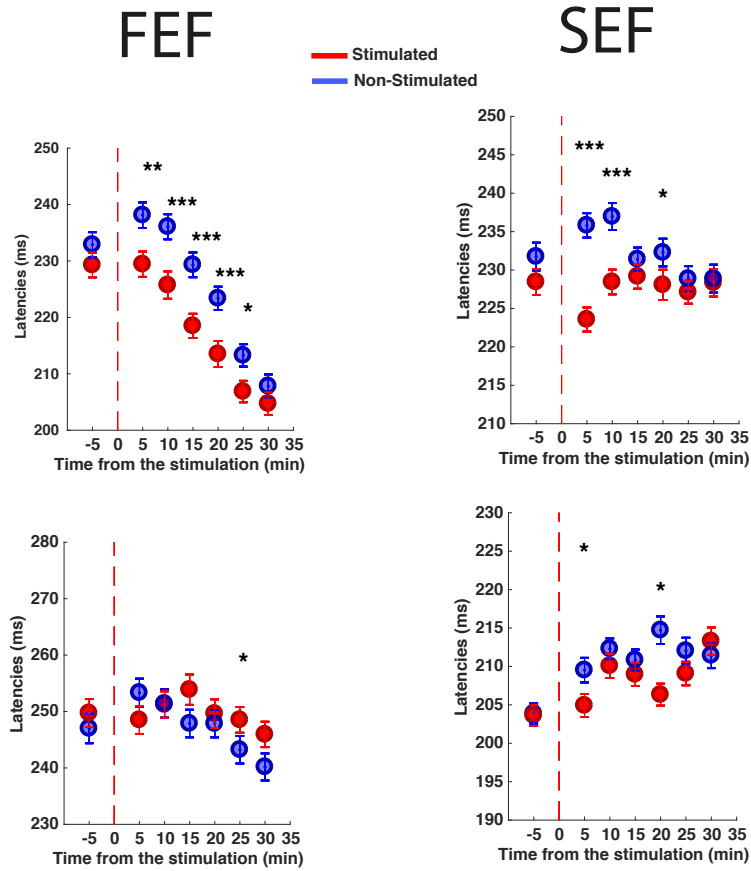


Figure 5.3: Mean saccadic latencies (in ms), separately for FEF and SEF conditions (FEF right or SEF in the left hemisphere respectively right and left panels) and direction of eye movement (ipsilateral (above) and contralateral (below) movement). Data were averaged across experimental sessions. Error bars represent normalized standard errors. The asterisk highlights the significantly affected antisaccade latencies with stimulation compared with baseline (* $p < 0.05$; ** $p < 0.01$; *** $p < 0.001$)

As shown in figure 5.3 (right) mean AS latencies with rTUS stimulation over the SEF on monkey A in the left hemisphere of the cerebral cortex were also significantly modulated compared to the non-stimulation. As for FEF, SEF stimulation modulates ipsilateral AS latencies. The first post stimulation block was 12.25ms (sem=1.68 ms) faster than the same block with no-stimulation (Wilcoxon rank sum test, $p < 0.001$). As shown in figure 5.4 and as compared to FEF or SEF stimulations, no significant effects of 20s of rTUS were observed after control regions stimulation of either visual (figure 5.4 left) or motor cortex (figure 5.4 right) (Wilcoxon rank sum test, $p > 0.1$).

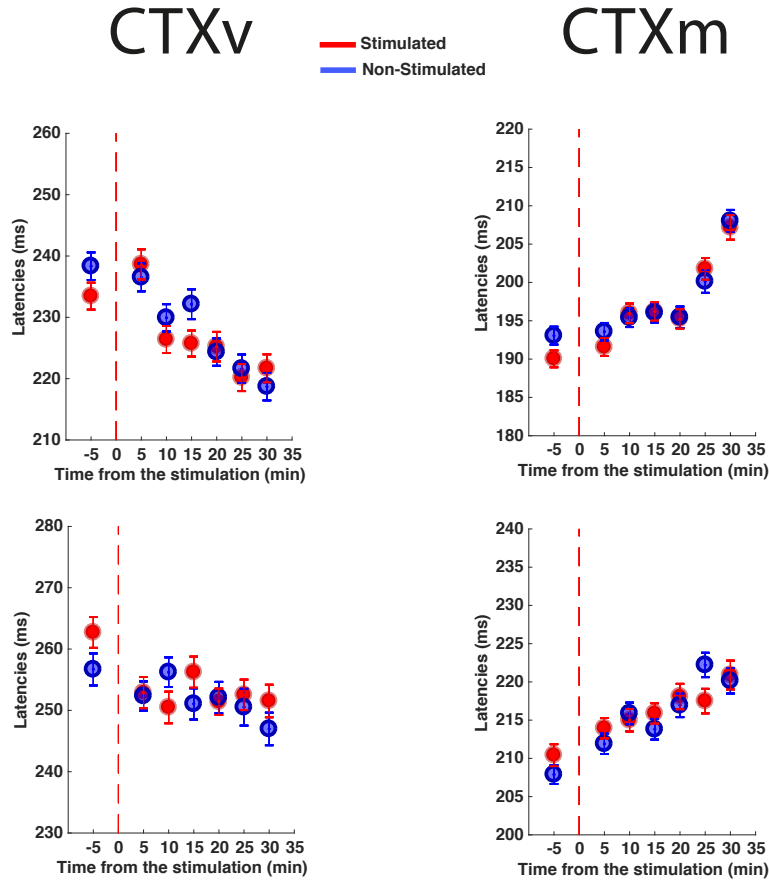


Figure 5.4: Mean saccadic latencies (in ms) for antisaccades, separately for control regions conditions (visual (left panel) or motor (right panel) cortex) and direction of eye movement (ipsilateral (above) and contralateral (below) movement). The asterisk highlights the significantly affected antisaccade latencies with stimulation compared with baseline. Note that none of the sham stimulation recorded sessions significantly differed from baseline ($*p < 0.05$; $**p < 0.01$; $***p < 0.001$).

Thermal modeling Results indicate a cooling of skull and brain rather than a heating, due to the contact with cold water. The maximum thermal rise over the whole volume was $0.2^{\circ}C$, ensuring the safety of the stimulation. Figure 5.5 displays the final temperature map, at the end of the 20s sonication, and the temporal evolution of the temperature at the focal point.

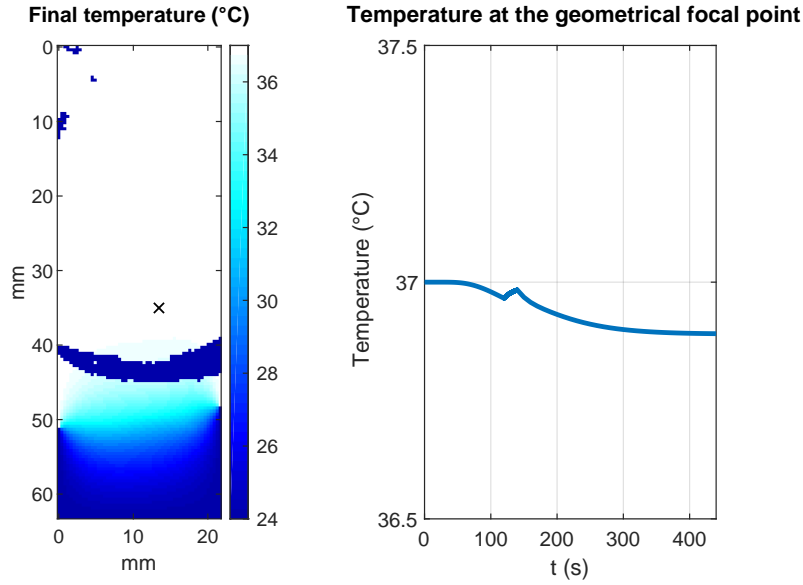


Figure 5.5: Thermal rise during rTUS. Left: Map of the final temperature at the end of rTUS sonication. The black cross indicates the focal spot location. Right: Temporal evolution of the temperature at focal point. Sonication begins at $t=120s$ and ends at $t=140s$.

5.4 Discussion

The study demonstrates the feasibility of using focused ultrasound to modulate visual behaviour for a sustained period of several minutes in the awake non-human primate brain. In this study, 30ms-long pulses of ultrasound fired at 10Hz for 20s were used with a low frequency (320) kHz and a low pressure amplitude (estimated at 0.4 MPa in situ). Compared with the modulation of response times reported with repetitive transcranial magnetic stimulation (rTMS) our results appear to be less affected by baseline variability of response times and no normalization was thus required [202]. Furthermore, no discomfort was observed in the animals during ultrasonic neurostimulation, in contrast to that observed during rTMS.

5.5 Conclusion

Extending the duration of ultrasound-induced neuromodulation effect from a few hundreds of milliseconds to 25 minutes is an encouraging step towards clinical applications for the treatment of

neurological disorders. During a long-term treatment with repetitive TUS, brain plasticity might also play a role. Further experiments are therefore needed to further improve the efficiency of TUS and study the brain's adaptation to explore the therapeutic potential of repetitive ultrasonic neuromodulation. Furthermore, the sustained effect opens the door to post-sonication functional Magnetic Resonance Imaging (fMRI) to investigate how the brain connectivity is affected by the local neuromodulation induced by focused ultrasound. The proof of concept of such an approach is investigated in the next chapter.

Chapter 6

Spatially specific and non-specific effects of focused ultrasound neuromodulation on BOLD responses in primates

6.1 Introduction

To understand brain circuits it is necessary both to record and manipulate their activity. In recent years, there has been extensive progress in this field, which was in part made possible by the availability of new technologies [17, 34, 169]. While techniques for transiently manipulating activity in rodents, such as optogenetics and chemogenetics, are increasingly accessible and applied, techniques for manipulating activity in the primate brain are less widely available and remain accessible to comparatively few researchers in a limited number of research centers worldwide. These techniques have yet to prove their full potential, especially for impacting on cortical activity and behavior. Here we propose to take advantage of the offline effects of TUS, investigating the impact of 40 s trains of TUS on the measurement of neural activity provided by fMRI up to 2 hours after stimulation. FMRI is one of the most widely used methods for estimating neural

activity. Despite limitations in its spatial and temporal resolution, fMRI is often used to provide information about activity throughout the whole brain thanks to its non-invasiveness. Rather than providing a direct measure of neural activity, it images the change in blood flow related to brain activity via the blood-oxygen-level dependent (BOLD) signal. Typically, fMRI-measured activity in any given brain area is a function of activity in other brain areas, especially those with which it is closely interconnected [152]. We exploited this feature of activity to examine the impact of TUS application to the pre-supplementary motor area (preSMA). In the control state, each area’s activity is normally a function of the activity in the areas that constitute its connectional fingerprint. If this pattern is altered by TUS in a manner that is dependent on the location of the stimulation, then this will constitute evidence that TUS exerts a spatially selective effect on neural activity. One animal participated in the study and a control experiment was conducted in the absence of TUS. This is a proof of concept study and we show here preliminary results.

6.2 Materials and Methods

Ultrasound We used a single element transducer (H115, diameter 64 mm, Sonic Concept, Bothell, WA, USA), geometrically focused to 63 mm, fixed to a coupling cone (C103, Sonic Concepts, Bothell, WA, USA) filled with degassed water. The signal was generated with a digital function generator (Handyscope HS5, TiePie engineering, Sneek, The Netherlands) and transmitted to a 75W amplifier (75A250A, Amplifier Research, Souderton, PA) which delivered the required power to the transducer. The output voltage was monitored with a voltage probe (HP9250, TiePie engineering, Sneek, The Netherlands) connected to the TiePie card. The ultrasound neurostimulation sequence was a 40s sonication composed of 30ms pulses at a PRF of 10 kHz (duty cycle: 30%). The ultrasound frequency was set to 200 kHz and the output voltage to 127 V, corresponding to a pressure amplitude at focus of 0.65 MPa, as measured in free water with a heterodyne interferometer. Skull transmission was estimated on a clean and degassed primate skull specimen (*Macaca mulatta* skull) at seven different locations and was found to be 61%. This allowed us to estimate the derated pressure to 0.4 MPa in the brain. The intensity spatial peak pulse average (ISPPA) is 5 W/cm² and the intensity spatial peak time average (ISPTA) is 0.15W/cm² behind the skull.

MRI Data Acquisition Resting-state fMRI and anatomical scans were collected for 1 healthy macaque (*Macaca mulatta*, male). Protocols for animal care, magnetic resonance imaging, and anaesthesia were carried out in accordance with the French Committee for ethical procedures in animal research and were approved by local ethic committee. Anaesthesia was induced using intramuscular injection of ketamine (10 mg/kg) either combined with xylazine (0.125-0.25 mg/kg) or with midazolam (0.1 mg/kg) and buprenorphine (0.01mg/kg). Macaques also received injections of atropine (0.05 mg/kg intramuscularly), meloxicam (0.2 mg/kg intravenously) and ranitidine (0.05 mg/kg intravenously). For non-TUS scanning sessions, the anaesthetized animals were placed in an MRI compatible stereotactic frame (Crist Instrument Co., Hagerstown, MA, USA). For TUS sessions, animals were scanned on a stereotaxic free frame (Rogue Research, Montreal, CA). In all cases animals were lying in a feet first prone position within a horizontal 3T MRI scanner with a full-size bore. Scanning commenced approximately 1.5-2 hours after induction, when the peak effect of ketamine was unlikely still to be present, and 5 minutes after sonication for the TUS sessions. This timing was kept for baseline sessions, without stimulation. Anaesthesia was maintained using the lowest possible concentration of isoflurane (0.8 - 1%) to ensure that macaques were lightly anaesthetised. The depth of anaesthesia was assessed using physiological parameters (heart rate and blood pressure as well as clinical checks before the scan for muscle relaxation). In addition to these parameters, core temperature and SpO₂ were monitored throughout the scan. A customized coil was used for data acquisition. A structural scan (three averages) was acquired using a T1-weighted MP-RAGE sequence (246 axial slices, TR: 2.3 s, TE: 2.5 ms, 0.8x0.8x0.8 mm voxel resolution). For each session, a whole-brain BOLD fMRI data was collected in three runs of 27 minutes, using the following parameters: 36 axial slices, in-plane resolution 2x2 mm, slice thickness 2 mm, no slice gap, TR=2050 ms, TE=30 ms, flip angle = 90°, 800 volumes per run.

Sessions Four sessions of three runs were acquired for pre-frontal cortex (preSMA) stimulation and for baseline. There was a minimum of one week gap between sessions.

Data analyses and statistics The analysis was conducted by Cécile Gallea (ICM). The first functional volumes of each functional dataset were discarded, and the following preprocessing was performed using FSL [62]: non-brain removal, 0.1 Hz low-pass filtering to remove respiratory artifacts, motion correction, spatial smoothing (using Gaussian 3 mm FWHM kernel), high-pass

temporal filtering (Gaussian-weighted least-squares straight line fitting, with $\sigma=50.0$ s). Registration of functional images to the skull-stripped structural and a macaque template (AFNI) was done using FLIRT [91]. The structural volume was segmented into gray matter, white matter, and CSF tissue classes [141]. The remaining temporal noise was described by the mean time course and the components of the white matter (WM) and CSF compartments (considering only voxels with a high posterior probability of belonging to the WM or CSF, obtained in the T1w image using FAST toolbox of FSL). Regions of interest definition: The stimulation points of the four preSMA sessions were located in medial prefrontal cortex, focused on the anterior part of preSMA. To construct region of interest (ROI) for preSMA, a circle of 4 mm radius was drawn following the contours of the cortical surface around the point closest to the average stimulation coordinate, in both the left and the right hemisphere. The same procedure was used to define other cortical regions of interest, based on literature coordinates in the visual cortex V1, to serve as seeds for connectivity analyses. V1 area is weakly connected with the preSMA stimulation site and was used as a control seed. Regression analyses were run following procedures described previously [181]. One model consisted of 9 regressors. The first regressor consisted of the first Eigen time series of each ROI. Eigen time series is a single time series which best reflects coherent activity across the mask, representing the largest amount of variance across the set of voxels in the ROI mask to minimize the mixing of signal and noise. The second and third regressors were the major Eigen time series in masks representing the white-matter and cerebrospinal fluid (CSF; across the whole brain volume), derived from the individual tissue segmentation. The six last regressors were the time series representing head motion during the recording [91]. These 8 “confounding” time series (white matter and CSF Eigen time series plus 6 time series representing head motion) were included in the first-level analyses as regressors of no interest. Individual statistical maps were then converted into template space for the second level analyses. The standard-space individual contrast maps were entered into a general linear model (GLM) analysis using a mixed-effects approach with automatic outlier deweighting [219, 218]. The resulting Z-statistical images were entered in a second level analysis (one-way ANOVA) testing the effect of the stimulation type (3 levels: prefrontal, visual, baseline) for each ROI separately. The main effects and post-hoc t-test were thresholded using clusters determined by $Z > 2.8$ and an uncorrected cluster significance threshold of $P < 0.001$.

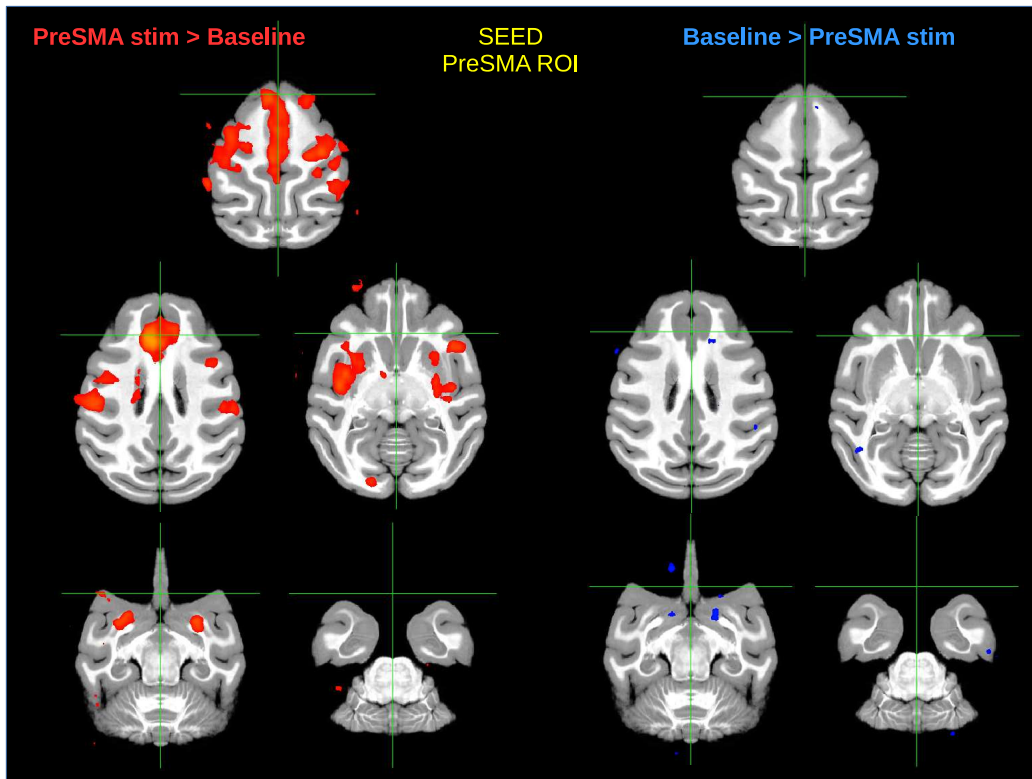


Figure 6.1: The red and blue clusters (left end right, respectively) represent the regions where the connectivity relative to preSMA is higher and lower, respectively, after preSMA stimulation compared to baseline.

Surgical procedure The surgical procedures for the titanium headpost implant were as previously described (chapter 4).

6.3 Results

Following prefrontal stimulation and compared to baseline, the anterior preSMA had an increase of functional connectivity with the bilateral medial prefrontal gyrus (medial area 8B), bilateral F3, bilateral intermediate part of the cingulate gyrus (area 24b'), bilateral lateral prefrontal cortex (area 8Bs/8Ad), bilateral F4, the bilateral 6VA/6VB (figure 6.1).

Following prefrontal stimulation and compared to baseline, there was no significant difference of functional connectivity seeding the visual cortex V1 (figure 6.2). None of the regions of interest showed any significant clusters in the reverse contrast (Baseline compared to preSMA stimulation).

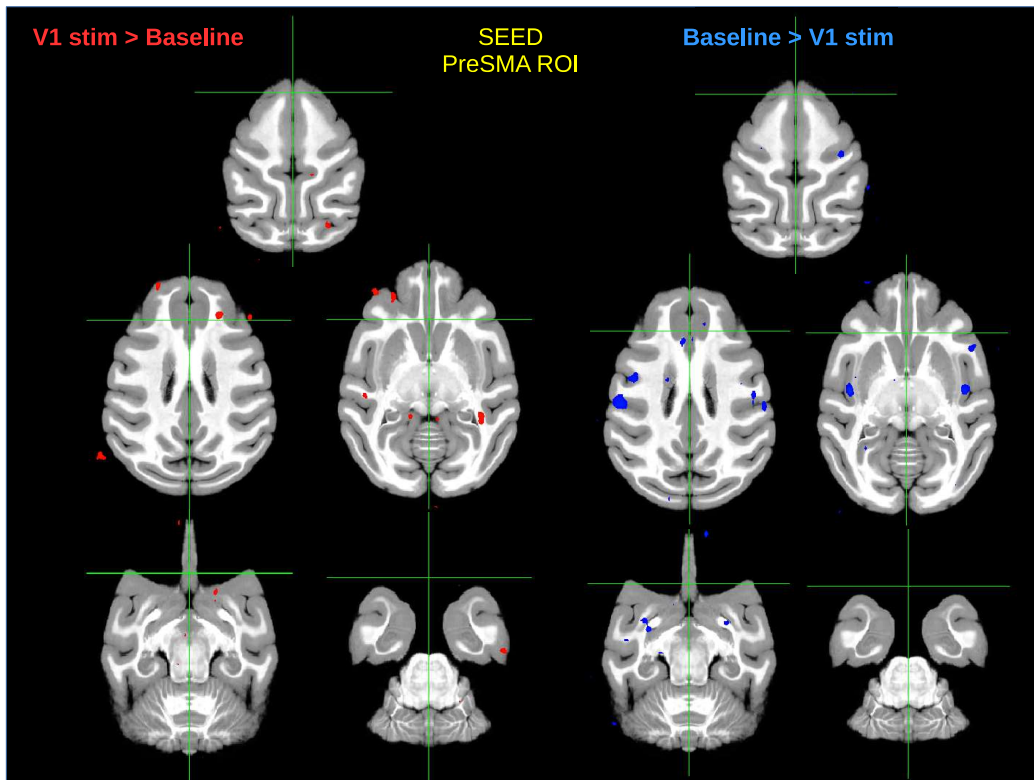


Figure 6.2: The red and blue clusters (left end right, respectively) represent the regions where the connectivity relative to V1 is higher and lower, respectively, after preSMA stimulation compared to baseline.

6.4 Discussion and conclusion

We found that preSMA's connectional fingerprint was significantly changed by TUS, but only when it was applied to that area itself (figures 6.1,6.2). The pattern of inputs each area receives from other areas and the influence it wields over other areas are a major determinant of its function and here we have shown that this pattern is altered by TUS. TUS may therefore provide a relatively straightforward method for transient manipulation of specific components of neural circuits in the primate brain. This may be important for investigating primate brain areas when homologues in non-primate species, such as rodents, are non-existent or disputed [172, 217].

Chapter 7

GABA-induced neuromodulation in non-human primates

7.1 Introduction

Despite the efforts to extend the neuromodulatory effects of ultrasound (chapter 5), the impact of TUS remains limited in time and intensity compared to other relatively established neurostimulation techniques. We show here that it is possible to bypass this issue by combining the action of ultrasound with the efficiency of a neuroactive agent. Most molecules, like γ -Aminobutyric acid (GABA), cannot pass the BBB. Nevertheless, the BBB can be temporary and reversibly lifted [105, 159] through the intravascular injection of microbubbles coupled with low-intensity ultrasound [83, 84]: the acoustic wave induces the bubbles oscillations in the fine brain capillaries, leading to the temporary disruption of the cohesion of endothelial cells through tight junctions which ensured the BBB efficiency. The BBB opening lasts a few hours [16] and its safety has been investigated in several studies on small animals [12, 211, 139] and non-human primates [137, 131], highlighting the possibility of non-destructive, efficient BBB openings below 0.46 mechanical index (MI) in rabbits [138] and 0.58 MI in monkeys [137]. None of these early studies have shown functional consequences of BBB opening. The technique holds promise for therapeutic drug delivery. A clinical trial has been conducted with the objective of delivering chemotherapy on patients with glioblastoma by opening the BBB with an ultrasound device implanted into the skull [24]. We

propose to use this as a novel tool for non-invasive and local brain modulation by delivering inhibiting or stimulating drugs. For example GABA is a neuroactive agent which does not normally pass through the BBB [209]. GABA is the main inhibitory neurotransmitter in the central nervous system: when it binds to a cell, it induces an hyperpolarization of its membrane. McDannold et al. (2015) [140] demonstrated the feasibility to temporary suppress the SSEP in rats by GABA delivery with ultrasonic BBB opening. Here we demonstrate that this technique is non-invasive, controllable, repeatable and reversible on anesthetized non-human primates with a real-time monitoring of bubbles harmonic response to ensure both safety and efficiency of the BBB opening. For the first time, functional modulation induced by BBB opening is observed in non-human primates. We targeted the visual cortex of the animals with a single-element transducer operated at 245 kHz. We observed a decrease of the visual response intensity to full field visual stimuli and investigated the GABA dose dependency of this effect. The BBB opening was confirmed twice with MRI acquisition. We additionally evaluated the relative impact of FUS alone, FUS with Ultrasound Contrast Agent (UCA), and GABA delivery on the visual response.

7.2 Materials and methods

Animals Two captive-born macaques (*Macaca mulatta* ‘A’ and ‘B’), both 6-year-old and respectively 8 and 10 kg, participated to the study. Monkeys were paired-housed and handled in strict accordance with the recommendations of the Weatherall Report about good animal practice. Monkey housing conditions, surgical procedures and experimental protocols were all carried out in strict accordance with the authorization for conducting experiments in our institute delivered by the Animal Health and Veterinary Medication Division of the Department of Public Veterinary Health, Nutrition and Food Safety of the French Ministry of Health (last renewal: Arrêté préfectoral DTPP B-75-13-19). Monkeys were enrolled in the project ‘Thérapie non invasive du cerveau par ultrasons focalisés’ (Non-invasive brain therapy using focused ultrasound) validated by the ethical committee C.DARWIN under the reference 6355. Our routine laboratory procedures included an environmental enrichment program where monkeys had access to toys, mirrors and swings. Monkeys also had visual, auditory and olfactory contacts with other animals and, when appropriate, could touch/groom each other. An institutional veterinary doctor regularly monitored the well-being and health conditions of the monkeys.

Anesthesia was induced with a blend of ketamine hydrochloride (3 mg/kg i.m.) and dexmedetomidine (0.015 mg/kg i.m.) for initial sedation and animals were anesthetized with isoflurane during the entire procedure (1.5% during installation, 1% during experiments). All procedures lasted less than 3 hours. Heart rate, temperature and respiration were monitored and kept within physiological range. The animal bodies were covered with survival sheets to limit the temperature decrease.

Focused ultrasound and harmonics control A single element focused ultrasound transducer (H117, Sonic Concept, Bothell, WA, USA) (center frequency 261kHz, diameter 64mm with 20mm central opening, $F=1$) with a passive cavitation detector (PCD) in its center (Y107, Sonic Concept, Bothell, WA, USA, 17.5mm active diameter, 64mm geometric focus, 10kHz to 20MHz bandwidth) was used at the frequency of 245 kHz. A coupling cone (C101, Sonic Concepts, Bothell, WA, USA) filled with degassed water was placed between the transducer and the animal head. The transducer was fixed on a mechanical arm with 4 rotation axes (Viewmaster LCD, Osmond Ergonomics, Wimborne, UK) to provide the flexibility for the positioning and orientation of the transducer over the head. The transducer was placed manually, targeting the middle of visual cortex V1. A thin layer of echographic gel (Aquasonic 100, Parker Laboratories Inc., Fairfield, NJ, USA) was applied on the shaved skin and on the membrane of the coupling cone to ensure acoustic coupling. The signal (20ms pulse every second for 200 seconds) was created by a function generator (33250A, Agilent, Santa Clara, CA). A 75-Watts amplifier (75A250A, Amplifier Research, Souderton, PA) was then used to deliver the required power to the transducer through a matching network and the input voltage of the transducer was monitored using a voltage probe (P6139A, Tektronix, Melrose, MA) connected to an oscilloscope (Handyscope HS5, TIEPIE Engineering, Sneek, The Netherlands). The amplifier gain was set to deliver an output voltage $V_{out}=200V$ peak-to-peak to the transducer. A calibration was conducted before the UCA injection: at a given amplifier gain, the amplitude of the signal generated by the first function generator was ramped up to 0.6V (with 0.02V steps), corresponding to approximately 215 V after amplification. The generator amplitude corresponding to the closest amplified voltage below 200V was chosen for the experiments. Different harmonics type responses were analyzed from the PCD recording.

The levels of the different harmonics types (harmonics nf_0 , subharmonic $f_0/2$ and ultraharmonics $(n+1/2)f_0$) and the broadband were recorded for this given voltage and used as baseline. In order

to estimate the peak pressure in the brain, a clean and degassed primate skull specimen (Maccaca Mulatta skull) was put in front of the transducer in a degassed water tank and the pressure at the focus was estimated using a heterodyne interferometer [30]. A heterodyne interferometer uses a laser beam to detect the vibration of a Mylar membrane induced by the ultrasound wave with. The amplitude of the vibration is then converted to pressure with high sensibility and a flat frequency response [178].

The transmission of ultrasound through the degassed primate skull was assessed at 6 different points randomly chosen on the skull. The transmission was found to be $82\% \pm 6\%$. The in situ pressure delivered to the monkey brain transcranially was subsequently estimated at 0.54 ± 0.03 MPa. The equivalent MI value is 1.1 with an Intensity Spatial Peak Pulse Average (I_{SPPA}) of $9.7W/cm^2$ in the brain. By taking into account the pulse duration and pulse repetition frequency (respectively 20ms and 1Hz, corresponding to a 2% duty cycle) during the sequence, the Intensity Spatial Peak Time Average (I_{SPTA}) is estimated to be $194mW/cm^2$ behind the primate skull.

Visual stimuli and visual evoked potentials (VEP) recordings The animals were installed in a sphinx position in front of a black screen. Eyes were kept opened and gel (Ocry-gel, TVM, France) was applied to avoid eyes drying. A run of visual stimuli consisted in 200 full field flashes separated by 2s intervals. Two electrodes were inserted symmetrically in the skin above the V1 regions. The reference electrode was subcutaneously inserted in the eye brows and the ground electrode in the maxilla. The VEPs were recorded on a MAP system (Plexon Inc., TX, USA). Sham sessions were performed without any ultrasound sonication nor UCA and GABA injection, but the timing of VEP recordings was identical to a non-sham session. The transducer was positioned on the animal head in order to reproduce the non-sham conditions but was turned off.

MRI We ran two experiments of BBB opening without the visual stimuli but with MRI assessment of Gadolinium (Gd) diffusion on monkey A. The MR contrast agent (MRCA) was gadoterate meglumine (Dotarem, Guerbet, France). We used a dose of 2mL of a 0.5mmol/mL Gd solution. The animal head was maintained with a stereotaxic frame during the image acquisition. Three MR acquisitions were obtained during the experiment. The first MRI acquisition was performed at baseline before sonication without MRCA. The second MRI acquisition was performed before

sonication and 5 to 10 minutes after injection of the MRCA (2mL), and the third acquisition was performed 15 minutes after sonication with a second MRCA injection 10 minutes after sonication. The second and third acquisitions were separated by a delay of about 25 minutes. MRI was performed with a 3T magnet (Prisma, Siemens, Germany) using an 8-channel receive only head coil specifically designed for non-human primate experiments (Life Services LLC, USA). Images were acquired with a 2D-sagittal T1-weighted turbo spin-echo sequence with the following parameters: TR/TE: 689/11 ms, Echo Train Length: 4; voxel size: 0.4*0.4*1.5 mm³, averages: 8, 10 slices, acquisition time: 7min 20s).

Data analysis Electrophysiological data were post-processed using Matlab (MathWorks). The ground electrode signal was subtracted from the VEP recordings. The resulting signals were then filtered with a Savitzky-Golay filter (order 1, 21 ms frame length) and averaged (200 VEPs for a run). The offset, calculated as the mean of the first 50ms, was removed from each curve. For the spectral power calculation, the signal was reduced to its period of interest (e.g. 0-100ms after stimulus onset) before the Fourier transform. The spectral vector was then squared and summed over its length to get the spectral power. To standardize the analysis among the sessions, we always considered the five first GABA runs, even though we could acquire more data in some sessions. The exception is for Monkey A – 2mg/kg and Monkey B – 1 mg/kg sessions, in which we have only 3 ‘GABA’ runs. In figure 5, the error bars represent the root mean square of the corresponding runs SEM (the ones giving minimum and maximum amplitudes). In figure S1, the average harmonic response over 15 ultrasound pulses is represented on a logarithmic scale as the Fourier transform of the time signals before and after UCA injection. The plots are normalized by the resonant response at f_0 after UCA injection.

7.3 Results

MRI To verify the efficiency of the FUS system, we performed two BBB openings on an anesthetized animal before an MRI acquisition. On these sessions, no VEP were recorded but the FUS + UCA procedure was identical. We used gadolinium (gadoterate meglumine, DOTAREM®, Guerbet, France) as the MR contrast agent (MRCA). Gadolinium has a molecular weight of 938 Da and does not normally pass the BBB [16]. The diffusion of the MRCA in the brain tissue

indicated where the BBB was disrupted. Both BBB openings proved successful on the images: the MRCA appeared in the occipital and cerebellar areas where ultrasounds were focalized after the FUS procedure only. Figure 7.1 displays the MRI images before and after BBB opening. The signal intensity of T1-weighted images varied from 1.23 to 2.27 in the targeted region, relatively to a Region of Interest (ROI) defined within neck muscle.

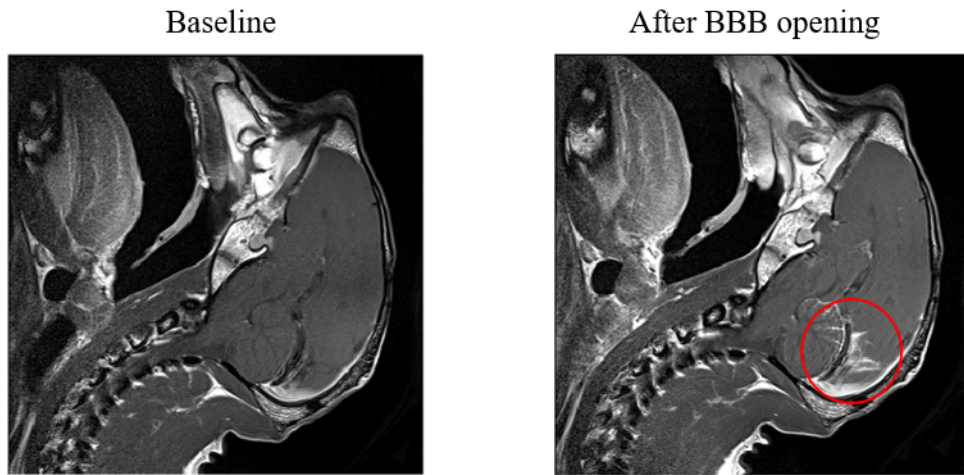


Figure 7.1: MRI assessment of BBB opening. Both images were obtained 10 minutes after injection of 2mL of a 0.5mmol /mL Gd. Left: before BBB opening. Right: after BBB opening. The red circle indicates the region where MRCA appeared.

Response to visual stimuli Figure 7.2 represents the timeline of the procedure. Three ‘baseline’ runs were performed after installation of the animal and placement of the transducer, prior to any sonication. The animals were installed in sphinx position in front of a black screen. Eyes were kept opened. A run of visual stimuli consisted in 200 full field white flashes with a stimulus onset asynchrony (SOA) of 2s. The animals were placed in a dim room and we waited at least five minutes after the complete extinction of light in the room to start the first run. A ‘neuromodulation’ sonication was then launched, with the same ultrasound sequence than for BBB opening but without any injection of UCA. The ‘neuromodulation’ run occurred at the end of this sonication. UCA injection was then performed under the reduced light of a smartphone, via a catheter inserted in the small saphenous vein before light extinction. The ultrasound sequence coupled with

the UCA injection was launched, followed by a ‘BBB opening, no GABA’ run. Finally GABA was injected intravenously (0.1 to 6 mg/kg) and at least 3 ‘GABA’ runs were conducted, depending on the animal temperature state.

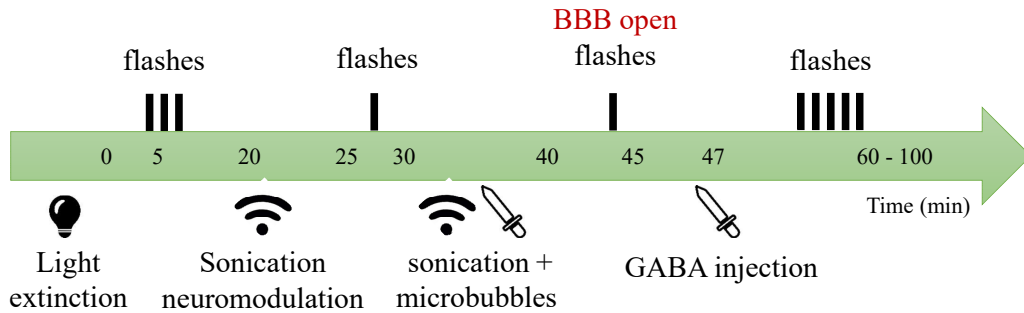


Figure 7.2: Timeline of the experiments. Each bar represents a VEP run (measurement of the visual responses to 200 full field flashes)

Figure 7.3 displays the VEP results of one session (monkey A, GABA dose=5 mg/kg). Each curve represents the mean of 200 responses. The ‘baseline’ curve corresponds to the third baseline run, the first two runs being considered as a period of stabilization and dark adaptation (a total time of 20 minutes). The legend describes the runs in the chronological order. A FUS procedure without UCA is performed between the ‘baseline’ and ‘neuromodulation’ runs. Then the BBB is opened with FUS and UCA injection between the ‘neuromodulation’ and ‘No GABA’ runs. Finally, GABA is injected intravenously after the ‘no GABA’ run and the ‘GABA’ runs are conducted successively, each one lasting about 5 min. Sham sessions were performed without any ultrasound sonication nor UCA and GABA injection, but the timing of VEP recordings was identical to a non-sham session. The runs’ names were kept similar to the non-sham sessions (‘baseline’, ‘neuromodulation’, ‘no GABA’, ‘GABA’), even though there was no neuromodulation nor GABA injection.

Another illustration of the decrease of visual response for both animals is shown in figure 7.4. For sake of clarity, only two of the recordings under sham conditions and at a 4 mg/kg GABA dose are displayed for each animal: the average of the VEP recordings of baseline 3 (before BBB opening), and the ‘GABA 1’ run (after BBB opening and GABA injection), corresponding to the first ‘GABA’ run.

Finally, we performed a dose study. To quantify the decrease of the visual cortex activity during

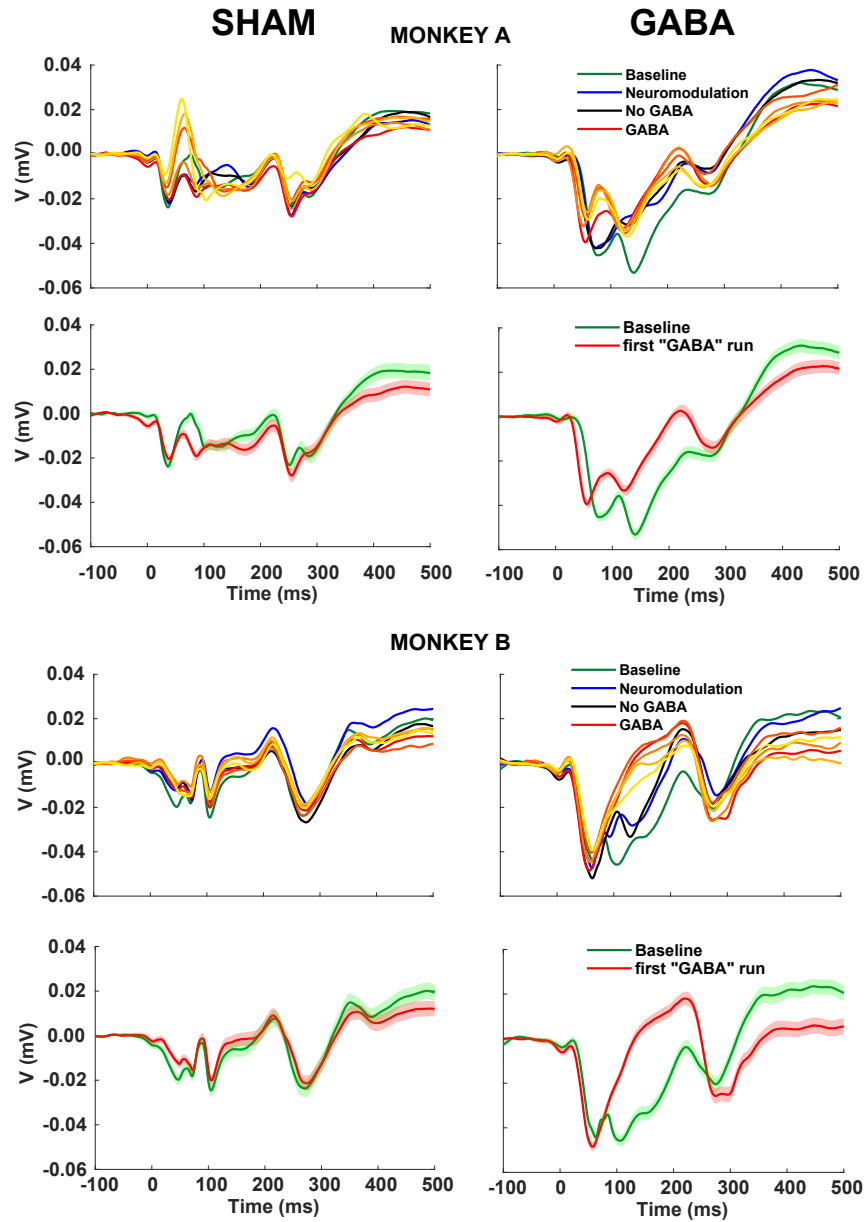


Figure 7.3: Mean VEP recordings for each run from baseline to ‘GABA 5’ for sham sessions on both monkeys (left), session 5 mg/kg GABA dose for monkey A and 4 mg/kg for monkey B (right). Each curve represents the VEP recordings of one run. The GABA runs are represented in orange gradient colors (red: GABA 1, yellow: GABA 5). The visual stimuli occur at time 0. For clarity purposes, each graph is replicated with only 2 runs (baseline run and first GABA run) with the standard error of the mean (SEM) (rows 2 and 4).

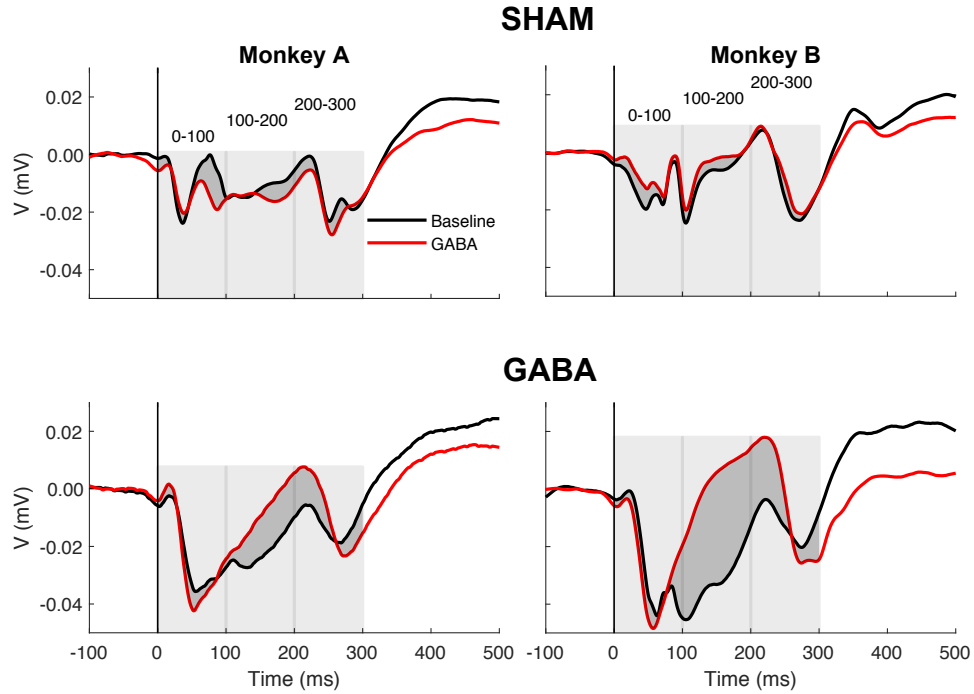


Figure 7.4: Comparison between the visual response before (last baseline: black curves) and after ('GABA 1': red curves) neuromodulation by BBB opening and GABA injection for the two animals with a 4 mg/kg GABA dose (bottom) or under sham conditions (up). Each curve represents the mean of the 200 VEP recordings.

each session, we considered the decay of the VEPs P1 amplitudes by calculating the difference between the maximum and the minimum P1 peaks over all GABA runs. Figure 7.5 shows that the impact on P1 amplitude increases linearly when the GABA dose increases.

UCA harmonics content For every pulse, the signal received by the hydrophone, monitored on the second channel of the TiePie oscilloscope, was analyzed in the frequency domain. The level of broadband, harmonics, subharmonics and ultraharmonics was displayed in real time. The subharmonic is the signal at half excitation frequency $f_0/2$ (here, $245/2 = 122.5$ kHz). The subharmonic emission is known to be associated with stable cavitation [165, 151]. Harmonics ($f = nf_0$ with $n \geq 2$) and ultraharmonics ($f = (n + 1/2)f_0$ with $n \geq 1$) emissions, which are also often associated with stable cavitation [151], were also recorded. The broadband emission corresponds to all the other frequencies emissions. This noise, caused by the bubbles collapse, is

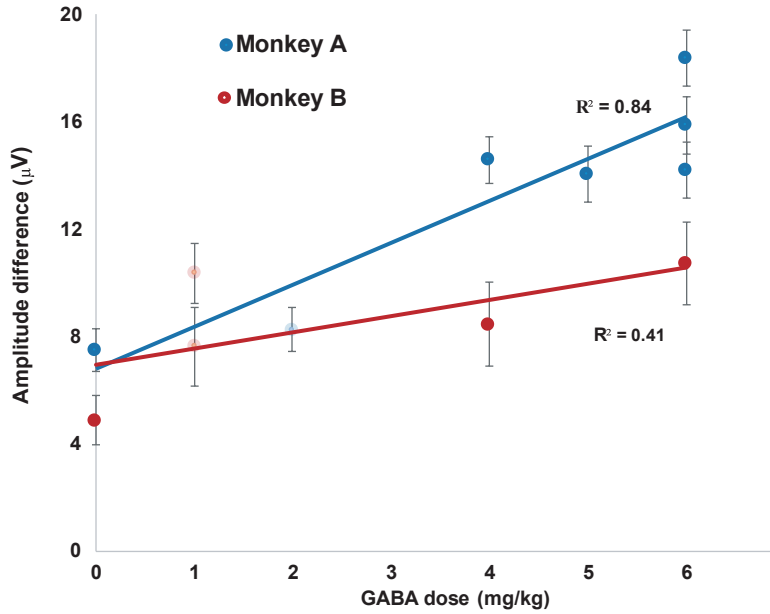


Figure 7.5: VEPs decrease of amplitude (maximum P1 amplitude – minimum P1 amplitude over the five first GABA runs (except for monkey A - 2mg and monkey B - 1mg with only 3 GABA runs, in light colors)) after GABA injection, as a function of GABA dose.

related to inertial cavitation.

The bolus injection of 2mL of UCA (SonoVue, Bracco, Milan, Italy) took place after the beginning of the sonications, typically between the 20th and 50th seconds (out of 200). A second injection of physiological serum with the same syringe was administrated a few seconds later to flush the rest of UCA that could have deposited in the syringe. The levels of the different harmonics types and the broadband were first recorded prior to UCA injection. The relative augmentation $\frac{harmonic\ level(i) - harmonic\ level(baseline)}{harmonic\ level(baseline)}$ was calculated at every pulse i for all types of harmonics and the broadband. An arbitrary safety threshold of 3 was set for the broadband maximum relative augmentation: if this value was reached, the sonication would stop immediately. An efficiency threshold was also set to 3 for the subharmonic $f_0/2$ minimum relative augmentation as an indicator of BBB opening.

Figure 7.6 displays the relative elevation for each pulse (one per second) for the session with monkey A at 5mg/kg GABA dose, which VEP results were presented previously (figure 7.2). The bolus injection of UCA (2mL) started at shot #15 and ended at shot #29. The syringe was rinsed with

a bolus of physiological serum between shots #47 and 50.

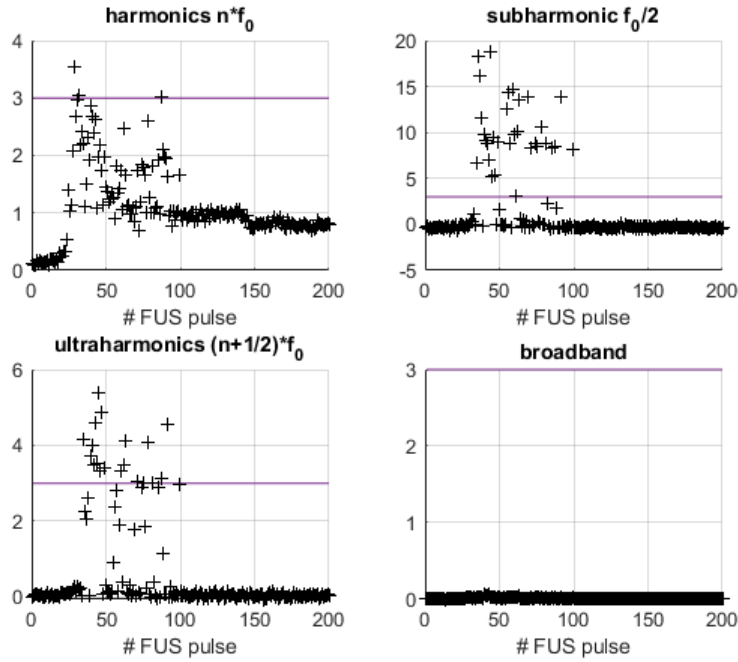


Figure 7.6: Harmonics and broadband level during BBB opening, session with monkey A at 5 mg/kg.

Figure 7.7 displays the mean harmonic content of the same session before the microbubbles injection (between the 1st and 15th pulses) and after (between the 45th and the 60th pulses). All types of harmonics are clearly emitted during the second period. The subharmonic emission was above the efficiency threshold for at least 21 seconds for all sessions.

Table 7.1 shows, for each session, the maximum level of relative augmentation for each type of harmonics and broadband. We also calculated the time spent by the subharmonic level above the efficiency threshold.

7.4 Discussion

Analysis of VEPs recordings showed a decrease of the visual response to the full field flashes following the GABA injection (figure 7.3 and 7.5). The activity was not suppressed entirely, whereas McDannold et al. (2015) [140] could almost completely inhibit the cortical primary somato-sensory

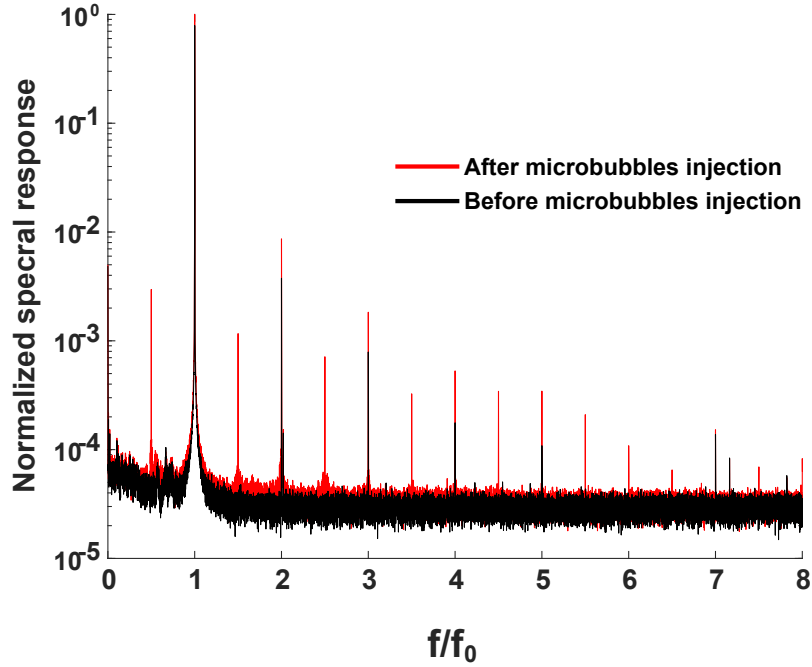


Figure 7.7: Spectral UCA response summed over $t=1$ to $t=15$ (before microbubbles injection) and over $t=45$ to $t=60$ (after microbubbles injection) on a logarithmic scale, session Monkey A 5mg/kg. The excitation frequency was $f_0=245$ kHz.

Table 7.1: Maximum relative augmentation and time above the efficiency threshold for the sub-harmonic.

Monkey	GABA dose (mg/kg)	Maximum relative augmentation							Time above the efficiency threshold
		broadband	$n * f_0$	$f_0/2$	$(n + 1/2) * f_0$	$f_0/3$	$f_0/4$	$f_0/6$	
Monkey B	1	1.2	0.6	2.3	1.2	5.3	1.9	2.0	21
Monkey B	1	0.83	7.5	40	16	13	8.6	3.5	70
Monkey A	2	0.57	6.0	25	16	12	7.9	2.1	140
Monkey A	4	0.08	1.5	46	3.2	0.7	0.4	0.3	150
Monkey B	4	1.2	4.5	4.0	5.7	5.7	3.5	2.5	>118
Monkey A	5	0.07	3.5	19	5.4	0.1	0.2	0.2	65
Monkey A	6	0.23	3.5	5.3	15	4.9	6	1.3	56
Monkey A	6	0.2	4.9	38	8.7	0.7	0.9	0.3	27
Monkey A	6	0.8	12.1	59	23	16	11	6	>157
Monkey B	6	1.1	8.1	80	21	7.1	5.7	3.1	>135

(S1) activity in rats. Several hypotheses could explain this difference.

First, we probably did not reach the GABA dose required to inhibit completely the structures were the BBB was open. Since there is no pharmacology data on BBB disruption-induced GABA in the brain, the dose was limited to 6 mg/kg in our study for the safety of the animals (due to

possible peripheral effect of GABA). For sake of comparison, McDannold et al. [140] injected up to 60mg/kg in rats.

Second, even at a frequency as low as 245 kHz, the focal spot did not cover the entire area involved in the visual circuit, as it can be seen on the MRI (figure 7.1). In the rat study, BBB disruption was produced in both the cortex and subcortical structures such as the thalamus [140], hence the possibility of a complete inhibition. Third, the inhibition of the visual cortex might not be as straightforward as the inhibition of S1 cortex. The contributions of distinct primary visual areas to feedforward and feedback connections to the electrical potential recorded by VEPs are complex to disentangle. Based on peak latencies, an incremental delay between V1, V2, V3, and V3A visual latency has been reported, suggesting serial stages of processing. The extent to which early visual areas have distinct time courses of activation is, however, somewhat contentious [4, 98]. According to direct recordings in monkeys, early visual areas first become active nearly simultaneously^{54,55}. Additionally, V2, V3, and V3A receive some degree of direct, subcortical input that bypasses V1 [15, 21, 226, 175, 187, 194]. Historically, single-cell recordings in nonhuman primates have shown that inactivation of higher-order areas modulates neuronal responses in lower-order areas [182, 79, 192, 81]. It has been shown that V1 activity is modulated by GABA inhibition of area V2. Another study found similar results for V1, V2, and V3 neurons when area MT was inactivated [80]. Many studies indicate feedback signals mediating surround suppression of V1 neurons. Taken together these results strongly support the role of feedback from higher visual areas in determining V1 neural activity. Feedback interactions in human vision were also reported recently. It has also have been shown that early (40–100 ms) inactivation of V1, using transcranial magnetic stimulation (TMS), inhibits detection of simple features, but not conjunctions [15]. Conversely, inactivation of V1 after longer delays (200–240 ms) seems to impair detection of feature conjunctions, while leaving simple feature detection intact. This double-dissociation implicates V1 in feedback loops with higher visual areas, although it does not specify from where such feedback might originate. Other TMS studies [93, 193] specifically indicated feedback inputs from MT to V1 with latencies 80–125 ms from the stimulus onset. Using transcranial ultrasound method, McDannold et al. [140] raised the question of possible neuromodulation effects on the somatosensorial cortex activity during BBB opening, independently of the GABA inhibition. Indeed, several studies reported that ultrasound-induced neuromodulation can modulate brain function in primates [114, 36, 215, 223]. In 5 out of

7 case, we observed a significant neuromodulation effects, before the GABA injection, between 100 and 300ms after the stimulus onset (figure 7.3 is one example). We therefore calculated the spectral power of the signals at each step: the baseline run, after ultrasound alone ('Neuromodulation' run), after ultrasound coupled with UCA before GABA injection ('No GABA' run), and finally after GABA injection ('GABA' run). We calculated the mean contribution of each step in the inhibition (corresponding to the spectral power decrease) over all sessions with a GABA dose of at least 4mg/kg for three different time periods: 0-100ms, 100-200ms and 200-300ms after the stimulus onset (figure 7.8). The neuromodulation contribution corresponds to the decrease of activity after the 'neuromodulation' run, i.e. the neuromodulation spectral power minus the baseline spectral power; the UCA contribution is the one after the 'no GABA' run, i.e. the 'No GABA' spectral power minus the neuromodulation spectral power; the GABA contribution is the one from the most perturbed 'GABA' run. In this analysis, we considered the spectral power instead of the amplitude in order to quantify the cerebral activity on different time periods after the stimulus onset. Results showed that FUS+UCA influence got stronger as time increases after the visual stimulus onset, compared to GABA-induced effects. The percentage of GABA-induced inhibition relative to the total inhibition (combined effects of neuromodulation, UCA and GABA) is 90% during the first 100 ms, 42% during the 100-200ms period and 50% during the 200-300ms period.

7.5 Conclusion

As for today, the study of brain connectivity often requires alterations of the brain structures that experimenters perform through direct injections in the brain [156, 190, 191, 87]. This work demonstrates the feasibility of non-invasively delivering a neurotransmitter on a targeted, limited region of the monkey brain, paving the way for extended connectivity studies using varied neuroactive agents in diverse regions, with adapted target volume sizes. Pharmacological applications are also concerned by the ability of safely delivering large molecules to a precise brain location; the translation of this work to the human anatomy requires further developments but will be facilitated by the recent development of multi-element transcranial ultrasound devices [46, 48, 121, 133, 43], as well a low cost approach taking advantage of an acoustic lens to compensate for the aberrations induced by the human skull [128].

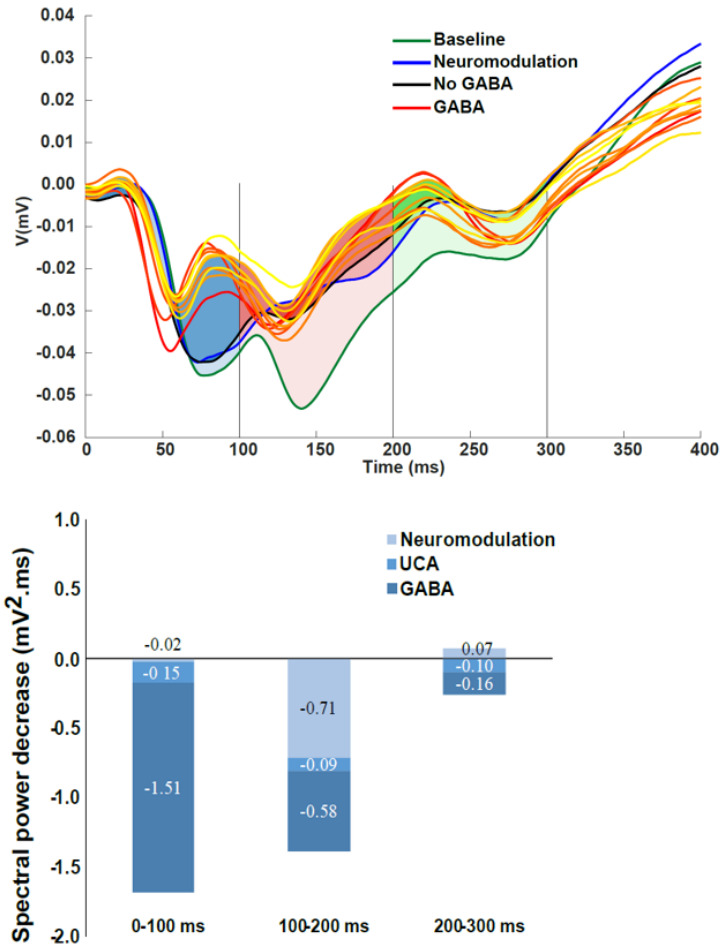


Figure 7.8: Proportion of the inhibitory effects due to neuromodulation (ultrasound only), BBB opening (ultrasound + UCA) and GABA (after BBB opening and GABA injection). Top: Illustration of the calculation of the contributions from the three events for one session (monkey A, GABA: 5 mg/kg). Bottom: Quantification (average of all sessions with a GABA dose of at least 4mg/kg on monkey A) of the contributions from neuromodulation, UCA and GABA on VEP spectral power decrease, for three different time periods.

Chapter 8

Conclusion and perspectives

The general objective of this manuscript was to investigate the potential of focused ultrasound for neuromodulation. The two main axis were: first, the optimization of the ultrasonic parameters, and second, the development of novel techniques to help investigate brain connectivity. Numerical simulations provide the pressure field distribution inside the brain, including the pressure amplitude and the shape of possible interferences at different frequencies, for each animal model. The study highlighted the influence of the frequency in the field distribution, not only regarding the focal spot size but also the occurrence and location of standing waves and the absorption effects. Simulations on rat and monkey models also underlined the influence of the skull geometry on wave propagation. Indeed, considering the skull thickness only is not enough to predict the pressure field in the brain: interferences in the bone and in the skull cavity were taken into account. The model will be useful to choose which set of parameters (power, frequency) is the best suited for a given study. Thermal rise estimation was then shown to help adjusting stimulation duration and duty cycle limits to avoid tissue lesions and limit thermal effects on neurons. Numerical results suggested that in previous studies from other groups, thermal dose might have come close to the threshold for brain damages. Our results underlie the need for a systematic surveillance of thermal effects.

Experimentation on monkeys allowed us to develop methods for the optimization of ultrasonic neuromodulation and for the understanding of the underlying physiological mechanism. First, the direct recording of a single neuron activity during ultrasound stimulation was achieved in awake

monkeys, which is a step forward in studying the direct effects of ultrasound on neurons. Second, a long lasting effect of focused ultrasound was induced thanks to repetitive ultrasonic neuromodulation : a significant perturbation of activity was measured in non human primates up to 25 minutes after stimulation, whereas only a few hundreds of milliseconds of modulation were previously reported. This work paved the way to non invasive stimulation followed by off line fMRI imaging of the brain activity in an ultrasound-free environment. Finally, the combined action of ultrasound and an inhibitory agent via the blood brain barrier opening highlighted the possibility for a non invasive, long lasting neuromodulation of a specific brain region with the efficiency of a neuroactive molecule. Localized and non-invasive neuromodulation (with or without a neuroactive agent) combined with non invasive whole brain activity imaging opens new avenues for studying brain connectivity.

Many follow-up research projects could be envisioned based on the work presented here. Our work on off line fMRI post ultrasonic neuromodulation could further be used to investigate long-term connectivity in the entire brain of any animal model and eventually humans. Furthermore, a new technique recently developed in our laboratory, functional ultrasound imaging, has provided maps of brain activity in rodents with high temporal and spatial accuracy. Simultaneous FUS stimulation and functional ultrasound imaging could give precious insight into neuromodulation effects in the cortical and sub-cortical structures. Lastly, the relative specificity of ultrasound effects with varied duty cycle on the different types of neurons could be exploited to activate selectively a given type of cells. The selectivity could be pushed even further by delivering, through blood brain barrier opening, designed drugs that would target specific receptors. The non invasive, reversible and local properties of ultrasound-induced BBB opening combined with techniques from imaging, molecular biology and genetics could lead to a wide range of applications not only in the biomedical field, but also in fundamental neuroscience.

Bibliography

- [1] N. J. Abbott, A. A. Patabendige, D. E. Dolman, S. R. Yusof, and D. J. Begley. Structure and function of the blood–brain barrier. *Neurobiology of disease*, 37(1):13–25, 2010.
- [2] N. J. Abbott and I. A. Romero. Transporting therapeutics across the blood-brain barrier. *Molecular Medicine Today*, 2(3):106–113, 1996.
- [3] N. J. Abbott, L. Rönnbäck, and E. Hansson. Astrocyte–endothelial interactions at the blood–brain barrier. *Nature Reviews Neuroscience*, 7(1):41, 2006.
- [4] J. M. Ales, J. L. Yates, and A. M. Norcia. V1 is not uniquely identified by polarity reversals of responses to upper and lower visual field stimuli. *NeuroImage*, 52(4):1401–1409, 2010.
- [5] T. J. Anderson and M. R. MacAskill. Eye movements in patients with neurodegenerative disorders. *Nature Reviews Neurology*, 9(2):74, 2013.
- [6] C. Antoniadou, U. Ettinger, B. Gaymard, I. Gilchrist, A. Kristjánsson, C. Kennard, R. J. Leigh, I. Noorani, P. Pouget, N. Smyrnis, et al. An internationally standardised antisaccade protocol. *Vision research*, 84:1–5, 2013.
- [7] M. Aryal, C. D. Arvanitis, P. M. Alexander, and N. McDannold. Ultrasound-mediated blood–brain barrier disruption for targeted drug delivery in the central nervous system. *Advanced Drug Delivery Reviews*, 72(Supplement C):94–109, 2014.
- [8] K. Ashkan, P. Rogers, H. Bergman, and I. Ughratdar. Insights into the mechanisms of deep brain stimulation. *Nature Reviews Neurology*, 13(9):548, 2017.
- [9] J.-F. Aubry, M. Tanter, M. Pernot, J.-L. Thomas, and M. Fink. Experimental demonstration

- of noninvasive transskull adaptive focusing based on prior computed tomography scans. *The Journal of the Acoustical Society of America*, 113(1):84–93, 2003.
- [10] D. Avery and G. Winokur. The efficacy of electroconvulsive therapy and antidepressants in depression. *Biological psychiatry*, 12(4):507–523, 1977.
- [11] J. W. Barnard, W. J. Fry, F. J. Fry, and R. F. Krumins. Effects of high intensity ultrasound on the central nervous system of the cat. *Journal of Comparative Neurology*, 103(3):459–484, 1955.
- [12] B. Baseri, J. J. Choi, Y.-S. Tung, and E. E. Konofagou. Multi-Modality Safety Assessment of Blood-Brain Barrier Opening Using Focused Ultrasound and Definity Microbubbles: A Short-Term Study. *Ultrasound in Medicine & Biology*, 36(9):1445–1459, 2010.
- [13] R. Bation, E. Poulet, F. Haesebaert, M. Saoud, and J. Brunelin. Transcranial direct current stimulation in treatment-resistant obsessive-compulsive disorder: an open-label pilot study. *Progress in Neuro-Psychopharmacology and Biological Psychiatry*, 65:153–157, 2016.
- [14] A. L. Benabid. Deep brain stimulation for parkinson’s disease. *Current opinion in neurobiology*, 13(6):696–706, 2003.
- [15] L. A. Benevento and K. Yoshida. The afferent and efferent organization of the lateral geniculo-prestriate pathways in the macaque monkey. *The Journal of Comparative Neurology*, 203(3), 1981.
- [16] Benjamin Marty, Benoit Larrat, Maxime Van Landeghem, Caroline Robic, Philippe Robert, Marc Port, Denis Le Bihan, Mathieu Pernot, Mickael Tanter, Franck Lethimonnier, and Sébastien Mériaux. Dynamic Study of Blood-Brain Barrier Closure after its Disruption using Ultrasound: A Quantitative Analysis. *Journal of Cerebral Blood Flow & Metabolism*, 32(10):1948–1958, 2012.
- [17] S. Bestmann and V. Walsh. Transcranial electrical stimulation. *Current Biology*, 27(23):R1258–R1262, 2017.
- [18] Bronstein JM, Tagliati M, Alterman RL, and et al. Deep brain stimulation for parkinson disease: An expert consensus and review of key issues. *Archives of Neurology*, 68(2):165–165, 2011.

- [19] C. J. Bruce and M. E. Goldberg. Primate frontal eye fields. I. Single neurons discharging before saccades. *Journal of Neurophysiology*, 53(3):603–635, 1985.
- [20] A. R. Brunoni, M. A. Nitsche, N. Bolognini, M. Bikson, T. Wagner, L. Merabet, D. J. Edwards, A. Valero-Cabre, A. Rotenberg, A. Pascual-Leone, R. Ferrucci, A. Priori, P. S. Boggio, and F. Fregni. Clinical research with transcranial direct current stimulation (tDCS): Challenges and future directions. *Brain Stimulation*, 5(3):175–195, 2012.
- [21] J. Bullier and H. Kennedy. Projection of the lateral geniculate nucleus onto cortical area V2 in the macaque monkey. *Experimental Brain Research*, 53(1):168–172, 1983.
- [22] P. W. Burgoon and J. A. Boulant. Temperature-sensitive properties of rat suprachiasmatic nucleus neurons. *American Journal of Physiology - Regulatory, Integrative and Comparative Physiology*, 281(3):R706–R715, 2001.
- [23] P. W. Burgoon and J. A. Boulant. Temperature-sensitive properties of rat suprachiasmatic nucleus neurons. *American Journal of Physiology-Regulatory, Integrative and Comparative Physiology*, 281(3):R706–R715, 2001.
- [24] A. Carpentier, M. Canney, A. Vignot, V. Reina, K. Beccaria, C. Horodyckid, C. Karachi, D. Leclercq, C. Lafon, J.-Y. Chapelon, L. Capelle, P. Cornu, M. Sanson, K. Hoang-Xuan, J.-Y. Delattre, and A. Idbah. Clinical trial of blood-brain barrier disruption by pulsed ultrasound. *Science Translational Medicine*, 8(343):343re2–343re2, 2016.
- [25] W. S. Chang, H. H. Jung, E. J. Kweon, E. Zadicario, I. Rachmilevitch, and J. W. Chang. Unilateral magnetic resonance guided focused ultrasound thalamotomy for essential tremor: practices and clinicoradiological outcomes. *Journal of Neurology, Neurosurgery & Psychiatry*, 86(3):257–264, 2015.
- [26] D. Chauvet, L. Marsac, M. Pernot, A.-L. Boch, R. Guillevin, N. Salameh, L. Souris, L. Darasse, M. Fink, M. Tanter, and J.-F. Aubry. Targeting accuracy of transcranial magnetic resonance-guided high-intensity focused ultrasound brain therapy: a fresh cadaver model. *Journal of Neurosurgery*, 118(5):1046–1052, 2013.
- [27] C.-C. Chio, T. Baba, and K. L. Black. Selective blood-tumor barrier disruption by leukotrienes. *Journal of neurosurgery*, 77(3):407–410, 1992.

- [28] G. T. Clement and K. Hynynen. A non-invasive method for focusing ultrasound through the human skull. *Physics in Medicine and Biology*, 47(8):1219–1236, 2002.
- [29] G. T. Clement, J. White, and K. Hynynen. Investigation of a large-area phased array for focused ultrasound surgery through the skull. *Physics in Medicine and Biology*, 45(4):1071–1083, 2000.
- [30] C. Constans, T. Deffieux, P. Pouget, M. Tanter, and J. F. Aubry. A 200 - 1380 kHz Quadrifrequency Focused Ultrasound Transducer For Neurostimulation In Rodents And Primates: Transcranial In Vitro Calibration And Numerical Study Of The Influence Of Skull Cavity. *IEEE Transactions on Ultrasonics, Ferroelectrics, and Frequency Control*, PP(99):1–1, 2017.
- [31] C. Constans, P. Mateo, M. Tanter, and J.-F. Aubry. Potential impact of thermal effects during ultrasonic neurostimulation: retrospective numerical estimation of temperature elevation in seven rodent setups. *Physics in Medicine & Biology*, 63(2):025003, 2018.
- [32] B. T. Cox, S. Kara, S. R. Arridge, and P. C. Beard. k-space propagation models for acoustically heterogeneous media: Application to biomedical photoacoustics. *The Journal of the Acoustical Society of America*, 121(6):3453–3464, 2007.
- [33] R. F. Dallapiazza, K. F. Timbie, S. Holmberg, J. Gatesman, M. B. Lopes, R. J. Price, G. W. Miller, and W. J. Elias. Noninvasive neuromodulation and thalamic mapping with low-intensity focused ultrasound. *Journal of Neurosurgery*, pages 1–10, 2017.
- [34] E. Dayan, N. Censor, E. R. Buch, M. Sandrini, and L. G. Cohen. Noninvasive brain stimulation: from physiology to network dynamics and back. *Nature neuroscience*, 16(7):838, 2013.
- [35] P. M. Daye, D. C. Roberts, D. S. Zee, and L. M. Optican. Vestibulo-Ocular Reflex Suppression during Head-Fixed Saccades Reveals Gaze Feedback Control. *Journal of Neuroscience*, 35(3):1192–1198, 2015.
- [36] T. Deffieux, Y. Younan, N. Wattiez, M. Tanter, P. Pouget, and J.-F. Aubry. Low-Intensity Focused Ultrasound Modulates Monkey Visuomotor Behavior. *Current Biology*, 23(23):2430–2433, 2013.

- [37] E. Dervishi, B. Larrat, M. Pernot, C. Adam, Y. Marie, M. Fink, J.-Y. Delattre, A.-L. Boch, M. Tanter, and J.-F. Aubry. Transcranial high intensity focused ultrasound therapy guided by 7 TESLA MRI in a rat brain tumour model: A feasibility study. *International Journal of Hyperthermia*, 29(6):598–608, 2013.
- [38] W. C. Dewey. Arrhenius relationships from the molecule and cell to the clinic. *International Journal of Hyperthermia*, 25(1):3–20, 2009.
- [39] I. du Cerveau et de la Moëlle épinière. <https://icm-institute.org/en/depression-en/>.
- [40] I. du Cerveau et de la Moëlle épinière. <https://icm-institute.org/en/ocd/>.
- [41] M. Dubin. Imaging tms: antidepressant mechanisms and treatment optimization. *International Review of Psychiatry*, 29(2):89–97, 2017.
- [42] F. A. Duck. *Physical properties of tissues: a comprehensive reference book*. Academic press, 2013.
- [43] M. D. Eames, A. Hananel, J. W. Snell, N. F. Kassell, and J.-F. Aubry. Trans-cranial focused ultrasound without hair shaving: feasibility study in an ex vivo cadaver model. *Journal of therapeutic ultrasound*, 1(1):24, 2014.
- [44] L. B. Ekstrom, P. R. Roelfsema, J. T. Arsenault, G. Bonmassar, and W. Vanduffel. Bottom-Up Dependent Gating of Frontal Signals in Early Visual Cortex. *Science*, 321(5887):414–417, 2008.
- [45] W. J. Elias, D. Huss, T. Voss, J. Loomba, M. Khaled, E. Zadicario, R. C. Frysinger, S. A. Sperling, S. Wylie, S. J. Monteith, J. Druzgal, B. B. Shah, M. Harrison, and M. Wintermark. A Pilot Study of Focused Ultrasound Thalamotomy for Essential Tremor, 2013.
- [46] W. J. Elias, D. Huss, T. Voss, J. Loomba, M. Khaled, E. Zadicario, R. C. Frysinger, S. A. Sperling, S. Wylie, S. J. Monteith, et al. A pilot study of focused ultrasound thalamotomy for essential tremor. *New England Journal of Medicine*, 369(7):640–648, 2013.
- [47] W. J. Elias, M. Khaled, J. D. Hilliard, J.-F. Aubry, R. C. Frysinger, J. P. Sheehan, M. Wintermark, and M. B. Lopes. A magnetic resonance imaging, histological, and dose modeling

- comparison of focused ultrasound, radiofrequency, and Gamma Knife radiosurgery lesions in swine thalamus. *Journal of Neurosurgery*, 119(2):307–317, 2013.
- [48] W. J. Elias, M. Khaled, J. D. Hilliard, J.-F. Aubry, R. C. Frysinger, J. P. Sheehan, M. Wintermark, and M. B. Lopes. A magnetic resonance imaging, histological, and dose modeling comparison of focused ultrasound, radiofrequency, and gamma knife radiosurgery lesions in swine thalamus. *Journal of neurosurgery*, 119(2):307–317, 2013.
- [49] W. J. Elias, N. Lipsman, W. G. Ondo, P. Ghanouni, Y. G. Kim, W. Lee, M. Schwartz, K. Hynynen, A. M. Lozano, B. B. Shah, et al. A randomized trial of focused ultrasound thalamotomy for essential tremor. *New England Journal of Medicine*, 375(8):730–739, 2016.
- [50] C. Ewencyk, S. Mesmoudi, C. Gallea, M.-L. Welter, B. Gaymard, A. Demain, L. Y. Cherif, B. Degos, H. Benali, P. Pouget, et al. Antisaccades in parkinson disease a new marker of postural control? *Neurology*, 88(9):853–861, 2017.
- [51] R. Fisher, V. Salanova, T. Witt, R. Worth, T. Henry, R. Gross, K. Oommen, I. Osorio, J. Nazzaro, D. Labar, et al. Electrical stimulation of the anterior nucleus of thalamus for treatment of refractory epilepsy. *Epilepsia*, 51(5):899–908, 2010.
- [52] U. Food. Drug administration information for manufacturers seeking marketing clearance of diagnostic ultrasound systems and transducers. *Center for Devices and Radiological Health, FDA, Rockville, MD*, 1997.
- [53] F. Fregni, P. S. Boggio, M. A. Nitsche, M. A. Marcolin, S. P. Rigonatti, and A. Pascual-Leone. Treatment of major depression with transcranial direct current stimulation. *Bipolar disorders*, 8(2):203–204, 2006.
- [54] F. J. Fry, H. W. Ades, and W. J. Fry. Production of Reversible Changes in the Central Nervous System by Ultrasound. *Science*, 127:83–84, 1958.
- [55] F. J. Fry and J. E. Barger. Acoustical properties of the human skull. *The Journal of the Acoustical Society of America*, 63(5):1576–1590, 1978.
- [56] F. J. Fry and Et. Production of reversible changes in the central nervous system by ultrasound, 1958.

- [57] W. J. Fry. Use Of Intense Ultrasound in Neurological Research. *American Journal of Physical Medecine*, 37(8), 1958.
- [58] W. J. Fry and F. J. Fry. Fundamental Neurological Research and Human Neurosurgery Using Intense Ultrasound. *IRE Transactions on Medical Electronics*, ME-7(3):166–181, 1960.
- [59] W. J. Fry and R. Meyers. Ultrasonic Method of Modifying Brain Structures. *Stereotactic and Functional Neurosurgery*, 22(3-5):315–327, 1962.
- [60] W. J. Fry, W. Mosberg Jr, J. Barnard, and F. Fry. Production of focal destructive lesions in the central nervous system with ultrasound. *Journal of neurosurgery*, 11(5):471–478, 1954.
- [61] W. J. Fry, V. J. Wulff, D. Tucker, and F. J. Fry. Physical Factors Involved in Ultrasonically Induced Changes in Living Systems: I. Identification of Non-Temperature Effects. *The Journal of the Acoustical Society of America*, 22(6):867–876, 1950.
- [62] FSL. <https://fsl.fmrib.ox.ac.uk/fsl/fslwiki>.
- [63] B. N. Gaynes, S. W. Lloyd, L. Lux, G. Gartlehner, R. A. Hansen, S. Brode, D. E. Jonas, T. E. Swinson, M. Viswanathan, and K. N. Lohr. Repetitive transcranial magnetic stimulation for treatment-resistant depression: a systematic review and meta-analysis., 2014.
- [64] M. S. George, J. J. Taylor, and E. B. Short. The expanding evidence base for rTMS treatment of depression:. *Current Opinion in Psychiatry*, 26(1):13–18, 2013.
- [65] M. S. George, E. M. Wassermann, W. A. Williams, A. Callahan, T. A. Ketter, P. Basser, M. Hallett, and R. M. Post. Daily repetitive transcranial magnetic stimulation (rtms) improves mood in depression. *Neuroreport: An International Journal for the Rapid Communication of Research in Neuroscience*, 1995.
- [66] A. Gironell, J. Kulisevsky, J. Lorenzo, M. Barbanoj, B. Pascual-Sedano, and P. Otermin. Transcranial magnetic stimulation of the cerebellum in essential tremor: a controlled study. *Archives of neurology*, 59(3):413–417, 2002.
- [67] S. A. Goss, L. A. Frizzell, and F. Dunn. Ultrasonic absorption and attenuation in mammalian tissues. *Ultrasound in Medicine & Biology*, 5(2):181–186, 1979.

- [68] B. D. Greenberg, M. S. George, J. D. Martin, J. Benjamin, et al. Effect of prefrontal repetitive transcranial magnetic stimulation in obsessive-compulsive disorder: a preliminary study. *The American journal of psychiatry*, 154(6):867, 1997.
- [69] B. D. Greenberg, D. A. Malone, G. M. Friehs, A. R. Rezai, C. S. Kubu, P. F. Malloy, S. P. Salloway, M. S. Okun, W. K. Goodman, and S. A. Rasmussen. Three-year outcomes in deep brain stimulation for highly resistant obsessive-compulsive disorder. *Neuropsychopharmacology*, 31(11):2384, 2006.
- [70] J. Greenwood. Experimental manipulation of the blood-brain” and blood-retinal barriers. In *Physiology and pharmacology of the blood-brain barrier*, pages 459–486. Springer, 1992.
- [71] M. Gumerlock and E. Neuwelt. Therapeutic opening of the blood-brain barrier in man. In *Physiology and Pharmacology of the Blood-Brain Barrier*, pages 525–542. Springer, 1992.
- [72] M. Hallett. Transcranial magnetic stimulation and the human brain. *Nature*, 406(6792):147, 2000.
- [73] B. T. Hawkins and T. P. Davis. The blood-brain barrier/neurovascular unit in health and disease. *Pharmacological Reviews*, 57(2):173–185, 2005.
- [74] T. Heimburg and A. D. Jackson. On soliton propagation in biomembranes and nerves. *Proceedings of the National Academy of Sciences of the United States of America*, 102(28):9790–9795, 2005.
- [75] A. L. Hodgkin and A. F. Huxley. A quantitative description of membrane current and its application to conduction and excitation in nerve. *The Journal of physiology*, 117(4):500–544, 1952.
- [76] P. E. Holtzheimer and H. S. Mayberg. Deep brain stimulation for psychiatric disorders. *Annual review of neuroscience*, 34:289–307, 2011.
- [77] M. F. Huerta, L. A. Krubitzer, and J. H. Kaas. Frontal eye field as defined by intracortical microstimulation in squirrel monkeys, owl monkeys, and macaque monkeys ii. cortical connections. *Journal of Comparative Neurology*, 265(3):332–361, 1987.

- [78] F. Hugo, B. van Heerden, N. Zungu-Dirwayi, and D. J. Stein. Functional brain imaging in obsessive-compulsive disorder secondary to neurological lesions. *Depression and anxiety*, 10(3):129–136, 1999.
- [79] J. M. Hupé, A. C. James, P. Girard, and J. Bullier. Response modulations by static texture surround in area V1 of the macaque monkey do not depend on feedback connections from V2. *Journal of Neurophysiology*, 85(1):146–163, 2001.
- [80] J. M. Hupé, A. C. James, P. Girard, S. G. Lomber, B. R. Payne, and J. Bullier. Feedback connections act on the early part of the responses in monkey visual cortex. *Journal of Neurophysiology*, 85(1):134–145, 2001.
- [81] J. Hupé, A. James, B. Payne, S. Lomber, P. Girard, and J. Bullier. Cortical feedback improves discrimination between figure and background by v1, v2 and v3 neurons. *Nature*, 394(6695):784, 1998.
- [82] K. Hynynen, N. McDannold, G. Clement, F. A. Jolesz, E. Zadicario, R. Killiany, T. Moore, and D. Rosen. Pre-clinical testing of a phased array ultrasound system for MRI-guided noninvasive surgery of the brain—A primate study. *European Journal of Radiology*, 59(2):149–156, 2006.
- [83] K. Hynynen, N. McDannold, N. A. Sheikov, F. A. Jolesz, and N. Vykhodtseva. Local and reversible blood–brain barrier disruption by noninvasive focused ultrasound at frequencies suitable for trans-skull sonications. *NeuroImage*, 24(1):12–20, 2005.
- [84] K. Hynynen, N. McDannold, N. Vykhodtseva, and F. A. Jolesz. Noninvasive MR Imaging–guided Focal Opening of the Blood-Brain Barrier in Rabbits. *Radiology*, 220(3):640–646, 2001.
- [85] S. Ibsen, A. Tong, C. Schutt, S. Esener, and S. H. Chalasani. Sonogenetics is a non-invasive approach to activating neurons in *Caenorhabditis elegans*. *Nature Communications*, 6:ncomms9264, 2015.
- [86] X. Jacob, C. Barriere, R. Takatsu, G. Montaldo, and D. Royer. Optical measurement of transient ultrasonic shock waves. In *IEEE Ultrasonics Symposium, 2004*, volume 1, pages 52–55 Vol.1, 2004.

- [87] A. Jansen-Amorim, M. Fiorani, and R. Gattass. Gaba-induced inactivation of cebus apella v2 neurons: effects on orientation tuning and direction selectivity. *Brazilian Journal of Medical and Biological Research*, 46(7):589–600, 2013.
- [88] D. Jeanmonod, B. Werner, A. Morel, L. Michels, E. Zadicario, G. Schiff, and E. Martin. Transcranial magnetic resonance imaging-guided focused ultrasound: noninvasive central lateral thalamotomy for chronic neuropathic pain. *Neurosurgical Focus*, 32(1):E1, 2011.
- [89] J. W. Jefferson, K. A. Kobak, D. J. Katzelnick, R. C. Serlin, et al. Efficacy and tolerability of serotonin transport inhibitors in obsessive-compulsive disorder: a meta-analysis. *Archives of General psychiatry*, 52(1):53–60, 1995.
- [90] B. Jenkins and S. J. Tepper. Neurostimulation for primary headache disorders: Part 2, review of central neurostimulators for primary headache, overall therapeutic efficacy, safety, cost, patient selection, and future research in headache neuromodulation. *Headache: The Journal of Head and Face Pain*, 51(9):1408–1418, 2011.
- [91] M. Jenkinson, P. Bannister, M. Brady, and S. Smith. Improved optimization for the robust and accurate linear registration and motion correction of brain images. *Neuroimage*, 17(2):825–841, 2002.
- [92] J. F. Jordão, E. Thévenot, K. Markham-Coultes, T. Scarcelli, Y.-Q. Weng, K. Xhima, M. O’reilly, Y. Huang, J. McLaurin, K. Hynynen, et al. Amyloid- β plaque reduction, endogenous antibody delivery and glial activation by brain-targeted, transcranial focused ultrasound. *Experimental neurology*, 248:16–29, 2013.
- [93] C.-H. Juan and V. Walsh. Feedback to v1: a reverse hierarchy in vision. *Experimental brain research*, 150(2):259–263, 2003.
- [94] H. H. Jung, W. S. Chang, I. Rachmilevitch, T. Tlusty, E. Zadicario, and J. W. Chang. Different magnetic resonance imaging patterns after transcranial magnetic resonance-guided focused ultrasound of the ventral intermediate nucleus of the thalamus and anterior limb of the internal capsule in patients with essential tremor or obsessive-compulsive disorder. *Journal of neurosurgery*, 122(1):162–168, 2015.

- [95] H. Kamimura, S. Wang, H. Chen, Q. Wang, C. Aurup, C. Acosta, A. Carneiro, and E. Konofagou. Pupil dilation and motor response elicitation by ultrasound neuromodulation. In *Ultrasonics Symposium (IUS), 2015 IEEE International*, pages 1–4, 2015.
- [96] H. A. S. Kamimura, S. Wang, H. Chen, Q. Wang, C. Aurup, C. Acosta, A. A. O. Carneiro, and E. E. Konofagou. Focused ultrasound neuromodulation of cortical and subcortical brain structures using 1.9 MHz: FUS neuromodulation of cortical/subcortical brain structures. *Medical Physics*, 43(10):5730–5735, 2016.
- [97] E. R. Kandel. *In search of memory: The emergence of a new science of mind*. WW Norton & Company, 2007.
- [98] S. P. Kelly, C. E. Schroeder, and E. C. Lalor. What does polarity inversion of extrastriate activity tell us about striate contributions to the early VEP? A comment on Ales et al. (2010). *NeuroImage*, 76:442–445, 2013.
- [99] H. Kim, A. Chiu, S. D. Lee, K. Fischer, and S.-S. Yoo. Focused Ultrasound-mediated Non-invasive Brain Stimulation: Examination of Sonication Parameters. *Brain Stimulation*, 7(5):748–756, 2014.
- [100] H. Kim, M. Y. Park, S. D. Lee, W. Lee, A. Chiu, and S.-S. Yoo. Suppression of eeg visual-evoked potentials in rats via neuromodulatory focused ultrasound. *Neuroreport*, 26(4):211, 2015.
- [101] R. L. King, J. R. Brown, W. T. Newsome, and K. B. Pauly. Effective Parameters for Ultrasound-Induced In Vivo Neurostimulation. *Ultrasound in Medicine & Biology*, 39(2):312–331, 2013.
- [102] W. C. Koller, K. E. Lyons, S. B. Wilkinson, A. I. Troster, and R. Pahwa. Long-term safety and efficacy of unilateral deep brain stimulation of the thalamus in essential tremor. *Movement disorders*, 16(3):464–468, 2001.
- [103] B. Krasovitski, V. Frenkel, S. Shoham, and E. Kimmel. Intramembrane cavitation as a unifying mechanism for ultrasound-induced bioeffects. *Proceedings of the National Academy of Sciences*, 108(8):3258–3263, 2011.

- [104] M. L. Kringelbach, N. Jenkinson, S. L. F. Owen, and T. Z. Aziz. Translational principles of deep brain stimulation. *Nature Reviews Neuroscience*, 8(8):623–635, 2007.
- [105] R. A. Kroll, E. A. Neuwelt, and E. A. Neuwelt. Outwitting the Blood-Brain Barrier for Therapeutic Purposes: Osmotic Opening and Other Means. *Neurosurgery*, 42(5):1083–1099, 1998.
- [106] Z. Kronfol, H. A. Nasrallah, S. Chapman, and J. D. House. Depression, cortisol metabolism and lymphocytopenia. *Journal of affective disorders*, 9(2):169–173, 1985.
- [107] D. Lee and A. D. Pierce. Parabolic equation development in recent decade. *Journal of Computational Acoustics*, 03(02):95–173, 1995.
- [108] W. Lee, Y. A. Chung, Y. Jung, I.-U. Song, and S.-S. Yoo. Simultaneous acoustic stimulation of human primary and secondary somatosensory cortices using transcranial focused ultrasound. *BMC Neuroscience*, 17:68, 2016.
- [109] W. Lee, H. Kim, Y. Jung, I.-U. Song, Y. A. Chung, and S.-S. Yoo. Image-Guided Transcranial Focused Ultrasound Stimulates Human Primary Somatosensory Cortex. *Scientific Reports*, 5:8743, 2015.
- [110] W. Lee, H.-C. Kim, Y. Jung, Y. A. Chung, I.-U. Song, J.-H. Lee, and S.-S. Yoo. Transcranial focused ultrasound stimulation of human primary visual cortex. *Scientific Reports*, 6:srep34026, 2016.
- [111] W. Lee, S. D. Lee, M. Y. Park, L. Foley, E. Purcell-Estabrook, H. Kim, K. Fischer, L.-S. Maeng, and S.-S. Yoo. Image-Guided Focused Ultrasound-Mediated Regional Brain Stimulation in Sheep. *Ultrasound in Medicine & Biology*, 42(2):459–470, 2016.
- [112] W. Lee, S. D. Lee, M. Y. Park, L. Foley, E. Purcell-Estabrook, H. Kim, K. Fischer, L.-S. Maeng, and S.-S. Yoo. Image-guided focused ultrasound-mediated regional brain stimulation in sheep. *Ultrasound in Medicine and Biology*, 42(2):459–470, 2016.
- [113] J.-P. Lefaucheur, N. André-Obadia, A. Antal, S. S. Ayache, C. Baeken, D. H. Benninger, R. M. Cantello, M. Cincotta, M. de Carvalho, D. De Ridder, et al. Evidence-based guidelines on the therapeutic use of repetitive transcranial magnetic stimulation (rtms). *Clinical Neurophysiology*, 125(11):2150–2206, 2014.

- [114] W. Legon, T. F. Sato, A. Opitz, J. Mueller, A. Barbour, A. Williams, and W. J. Tyler. Transcranial focused ultrasound modulates the activity of primary somatosensory cortex in humans. *Nature Neuroscience*, 17(2):322–329, 2014.
- [115] G. Leinenga and J. Götz. Scanning ultrasound removes amyloid- β and restores memory in an alzheimer’s disease mouse model. *Science translational medicine*, 7(278):278ra33–278ra33, 2015.
- [116] P. P. Lele. Effects of focused ultrasonic radiation on peripheral nerve, with observations on local heating. *Experimental Neurology*, 8(1):47–83, 1963.
- [117] L. Leocani, L. G. Cohen, E. M. Wassermann, K. Ikoma, and M. Hallett. Human corticospinal excitability evaluated with transcranial magnetic stimulation during different reaction time paradigms. *Brain*, 123(6):1161–1173, 2000.
- [118] G.-F. Li, H.-X. Zhao, H. Zhou, F. Yan, J.-Y. Wang, C.-X. Xu, C.-Z. Wang, L.-L. Niu, L. Meng, S. Wu, H.-L. Zhang, W.-B. Qiu, and H.-R. Zheng. Improved Anatomical Specificity of Non-invasive Neuro-stimulation by High Frequency (5 MHz) Ultrasound. *Scientific Reports*, 6:24738, 2016.
- [119] P. Limousin, J. Speelman, F. Gielen, M. Janssens, et al. Multicentre european study of thalamic stimulation in parkinsonian and essential tremor. *Journal of Neurology, Neurosurgery & Psychiatry*, 66(3):289–296, 1999.
- [120] C.-Y. Lin, H.-Y. Hsieh, C.-M. Chen, S.-R. Wu, C.-H. Tsai, C.-Y. Huang, M.-Y. Hua, K.-C. Wei, C.-K. Yeh, and H.-L. Liu. Non-invasive, neuron-specific gene therapy by focused ultrasound-induced blood-brain barrier opening in parkinson’s disease mouse model. *Journal of Controlled Release*, 235:72–81, 2016.
- [121] N. Lipsman, M. L. Schwartz, Y. Huang, L. Lee, T. Sankar, M. Chapman, K. Hynynen, and A. M. Lozano. Mr-guided focused ultrasound thalamotomy for essential tremor: a proof-of-concept study. *The Lancet Neurology*, 12(5):462–468, 2013.
- [122] N. Lipsman, M. L. Schwartz, Y. Huang, L. Lee, T. Sankar, M. Chapman, K. Hynynen, and A. M. Lozano. MR-guided focused ultrasound thalamotomy for essential tremor: a proof-of-concept study. *The Lancet Neurology*, 12(5):462–468, 2013.

- [123] H.-L. Liu, M.-Y. Hua, P.-Y. Chen, P.-C. Chu, C.-H. Pan, H.-W. Yang, C.-Y. Huang, J.-J. Wang, T.-C. Yen, and K.-C. Wei. Blood-brain barrier disruption with focused ultrasound enhances delivery of chemotherapeutic drugs for glioblastoma treatment. *Radiology*, 255(2):415–425, 2010.
- [124] C. K. Loo and P. B. Mitchell. A review of the efficacy of transcranial magnetic stimulation (TMS) treatment for depression, and current and future strategies to optimize efficacy. *Journal of Affective Disorders*, 88(3):255–267, 2005.
- [125] E. Louis. Essential tremor. *The Lancet. Neurology*, 4(2):100, 2005.
- [126] G. Luppino, M. Matelli, and G. Rizzolatti. Cortico-cortical connections of two electrophysiologically identified arm representations in the mesial agranular frontal cortex. *Experimental Brain Research*, 82(1):214–218, 1990.
- [127] E. Macé, G. Montaldo, I. Cohen, M. Baulac, M. Fink, and M. Tanter. Functional ultrasound imaging of the brain. *Nature Methods*, 8(8):662, 2011.
- [128] G. Maimbourg, A. Houdouin, T. Deffieux, M. Tanter, and J.-F. Aubry. 3d-printed adaptive acoustic lens as a disruptive technology for transcranial ultrasound therapy using single-element transducers. *Physics in Medicine & Biology*, 63(2):025026, 2018.
- [129] F. Marquet, A.-L. Boch, M. Pernot, G. Montaldo, D. Seilhean, M. Fink, M. Tanter, and J.-F. Aubry. Non-invasive ultrasonic surgery of the brain in non-human primates. *The Journal of the Acoustical Society of America*, 134(2):1632, 2013.
- [130] F. Marquet, M. Pernot, J.-F. Aubry, M. Tanter, G. Montaldo, and M. Fink. In-vivo non-invasive motion tracking and correction in High Intensity Focused Ultrasound therapy. pages 688–691. IEEE, 2006.
- [131] F. Marquet, Y.-S. Tung, T. Teichert, V. P. Ferrera, and E. E. Konofagou. Noninvasive, Transient and Selective Blood-Brain Barrier Opening in Non-Human Primates In Vivo. *PLOS ONE*, 6(7):e22598, 2011.
- [132] R. T. Marrocco. Saccades induced by stimulation of the frontal eye fields: Interaction with voluntary and reflexive eye movements. *Brain Research*, 146(1):23–34, 1978.

- [133] L. Marsac, D. Chauvet, R. La Greca, A.-L. Boch, K. Chaumoitre, M. Tanter, and J.-F. Aubry. Ex vivo optimisation of a heterogeneous speed of sound model of the human skull for non-invasive transcranial focused ultrasound at 1 mhz. *International Journal of Hyperthermia*, 33(6):635–645, 2017.
- [134] E. Martin, D. Jeanmonod, A. Morel, E. Zadicario, and B. Werner. High-intensity focused ultrasound for noninvasive functional neurosurgery. *Annals of Neurology*, 66(6):858–861, 2009.
- [135] J. L. R. Martin, M. J. Barbanoj, T. E. Schlaepfer, E. Thompson, V. Pérez, and J. Kulisevsky. Repetitive transcranial magnetic stimulation for the treatment of depression: systematic review and meta-analysis. *The British Journal of Psychiatry*, 182(6):480–491, 2003.
- [136] H. S. Mayberg, A. M. Lozano, V. Voon, H. E. McNeely, D. Seminowicz, C. Hamani, J. M. Schwalb, and S. H. Kennedy. Deep brain stimulation for treatment-resistant depression. *Neuron*, 45(5):651–660, 2005.
- [137] N. McDannold, C. D. Arvanitis, N. Vykhodtseva, and M. S. Livingstone. Temporary Disruption of the Blood–Brain Barrier by Use of Ultrasound and Microbubbles: Safety and Efficacy Evaluation in Rhesus Macaques. *Cancer Research*, 72(14):3652–3663, 2012.
- [138] N. McDannold, N. Vykhodtseva, and K. Hynynen. Blood-Brain Barrier Disruption Induced by Focused Ultrasound and Circulating Preformed Microbubbles Appears to Be Characterized by the Mechanical Index. *Ultrasound in Medicine & Biology*, 34(5):834–840, 2008.
- [139] N. McDannold, N. Vykhodtseva, F. A. Jolesz, and K. Hynynen. MRI investigation of the threshold for thermally induced blood-brain barrier disruption and brain tissue damage in the rabbit brain. *Magnetic Resonance in Medicine*, 51(5):913–923, 2004.
- [140] N. McDannold, Y. Zhang, C. Power, C. D. Arvanitis, N. Vykhodtseva, and M. Livingstone. Targeted, noninvasive blockade of cortical neuronal activity. *Scientific Reports*, 5, 2015.
- [141] D. G. McLaren, K. J. Kosmatka, T. R. Oakes, C. D. Kroenke, S. G. Kohama, J. A. Matochik, D. K. Ingram, and S. C. Johnson. A population-average mri-based atlas collection of the rhesus macaque. *Neuroimage*, 45(1):52–59, 2009.

- [142] M. D. Menz, Ö. Oralkan, P. T. Khuri-Yakub, and S. A. Baccus. Precise neural stimulation in the retina using focused ultrasound. *Journal of Neuroscience*, 33(10):4550–4560, 2013.
- [143] B.-K. Min, A. Bystritsky, K.-I. Jung, K. Fischer, Y. Zhang, L.-S. Maeng, S. In Park, Y.-A. Chung, F. A. Jolesz, and S.-S. Yoo. Focused ultrasound-mediated suppression of chemically-induced acute epileptic EEG activity. *BMC Neuroscience*, 12:23, 2011.
- [144] A. Misra, S. Ganesh, A. Shahiwala, and S. P. Shah. Drug delivery to the central nervous system: a review. *Journal of pharmacy & pharmaceutical sciences : a publication of the Canadian Society for Pharmaceutical Sciences, Societe canadienne des sciences pharmaceutiques*, 6(2):252–273, 2003.
- [145] J. H. Moore, J. Gieck, E. Saliba, D. Perrin, D. Ball, and F. McCue. *The biophysical effects of ultrasound on median nerve distal latencies*. PhD thesis, University of Virginia, 1997.
- [146] T. Moore and K. M. Armstrong. Selective gating of visual signals by microstimulation of frontal cortex. *Nature*, 421(6921):370, 2003.
- [147] T. Moore and M. Fallah. Control of eye movements and spatial attention. *Proceedings of the National Academy of Sciences*, 98(3):1273–1276, 2001.
- [148] D. Moser, E. Zadicario, G. Schiff, and D. Jeanmonod. MR-guided focused ultrasound technique in functional neurosurgery: targeting accuracy. *Journal of Therapeutic Ultrasound*, 1:3, 2013.
- [149] J. K. Mueller, L. Ai, P. Bansal, and W. Legon. Computational exploration of wave propagation and heating from transcranial focused ultrasound for neuromodulation. *Journal of Neural Engineering*, 13(5):056002, 2016.
- [150] O. Naor, Y. Hertzberg, E. Zemel, E. Kimmel, and S. Shoham. Towards multifocal ultrasonic neural stimulation II: design considerations for an acoustic retinal prosthesis. *Journal of Neural Engineering*, 9(2):026006, 2012.
- [151] E. A. Neppiras. Acoustic cavitation. *Physics Reports*, 61(3):159–251, 1980.

- [152] F.-X. Neubert, R. B. Mars, A. G. Thomas, J. Sallet, and M. F. Rushworth. Comparison of human ventral frontal cortex areas for cognitive control and language with areas in monkey frontal cortex. *Neuron*, 81(3):700–713, 2014.
- [153] M. A. Nitsche, P. S. Boggio, F. Fregni, and A. Pascual-Leone. Treatment of depression with transcranial direct current stimulation (tDCS): A Review. *Experimental Neurology*, 219(1):14–19, 2009.
- [154] M. A. Nitsche, L. G. Cohen, E. M. Wassermann, A. Priori, N. Lang, A. Antal, W. Paulus, F. Hummel, P. S. Boggio, F. Fregni, et al. Transcranial direct current stimulation: state of the art 2008. *Brain Stimulation: Basic, Translational, and Clinical Research in Neuromodulation*, 1(3):206–223, 2008.
- [155] B. Nuttin, P. Cosyns, H. Demeulemeester, J. Gybels, and B. Meyerson. Electrical stimulation in anterior limbs of internal capsules in patients with obsessive-compulsive disorder. *The Lancet*, 354(9189):1526, 1999.
- [156] S. W. Oh, J. A. Harris, L. Ng, B. Winslow, N. Cain, S. Mihalas, Q. Wang, C. Lau, L. Kuan, A. M. Henry, et al. A mesoscale connectome of the mouse brain. *Nature*, 508(7495):207, 2014.
- [157] U. Palm, S. Ayache, F. Padberg, and J. Lefaucheur. Transcranial direct current stimulation (tdcs) for depression: Results of nearly a decade of clinical research, 2016.
- [158] G. I. Papakostas. Tolerability of modern antidepressants. *The Journal of clinical psychiatry*, 69:8–13, 2008.
- [159] W. M. Pardridge. The Blood-Brain Barrier: Bottleneck in Brain Drug Development. *NeuroRX*, 2(1):3–14, 2005.
- [160] Passeportsante. <https://www.passeportsante.net/fr/maux/problemes/fiche.aspx?doc=depression-pm-traitements-medicaux-de-la-depression>.
- [161] H. H. Pennes. Analysis of Tissue and Arterial Blood Temperatures in the Resting Human Forearm. *Journal of Applied Physiology*, 1(2):93–122, 1948.

- [162] G. Percheron, C. François, and P. Pouget. What makes a frontal area of primate brain the frontal eye field? *Frontiers in Integrative Neuroscience*, 9, 2015.
- [163] E. Persad. Electroconvulsive therapy in depression. *The Canadian Journal of Psychiatry*, 35(2):175–182, 1990.
- [164] A. G. Petrov. Flexoelectric Model for Active Transport. In *Physical and Chemical Bases of Biological Information Transfer*, pages 111–125. Springer, Boston, MA, 1975. DOI: 10.1007/978-1-4684-2181-1_9.
- [165] A. D. Phelps and T. G. Leighton. The Subharmonic Oscillations And Combination-Frequency Subharmonic Emissions From A Resonant Bubble: Their Properties and Generation Mechanisms. *Acta Acustica united with Acustica*, 83(1):59–66, 1997.
- [166] G. Pinton, J.-F. Aubry, E. Bossy, M. Muller, M. Pernot, and M. Tanter. Attenuation, scattering, and absorption of ultrasound in the skull bone. *Medical Physics*, 39(1):299–307, 2012.
- [167] M. Plaksin, E. Kimmel, and S. Shoham. Cell-type-selective effects of intramembrane cavitation as a unifying theoretical framework for ultrasonic neuromodulation. *eNeuro*, pages ENEURO–0136, 2016.
- [168] M. Plaksin, S. Shoham, and E. Kimmel. Intramembrane Cavitation as a Predictive Bio-Piezoelectric Mechanism for Ultrasonic Brain Stimulation. *Physical Review X*, 4(1):011004, 2014.
- [169] R. Polanía, M. A. Nitsche, and C. C. Ruff. Studying and modifying brain function with non-invasive brain stimulation. *Nature neuroscience*, page 1, 2018.
- [170] P. Pouget. The cortex is in overall control of ‘voluntary’ eye movement. *Eye*, 29(2):241, 2015.
- [171] P. Pouget, A. Murthy, and V. Stuphorn. Cortical control and performance monitoring of interrupting and redirecting movements. *Phil. Trans. R. Soc. B*, 372(1718):20160201, 2017.
- [172] T. M. Preuss. Do rats have prefrontal cortex? the rose-woolsey-akert program reconsidered. *Journal of cognitive neuroscience*, 7(1):1–24, 1995.

- [173] A. Priori, M. Hallett, and J. C. Rothwell. Repetitive transcranial magnetic stimulation or transcranial direct current stimulation? *Brain Stimulation: Basic, Translational, and Clinical Research in Neuromodulation*, 2(4):241–245, 2009.
- [174] C. L. Prosser. Action potentials in the nervous system of the crayfish. *The Journal of General Physiology*, 19(1):65–73, 1935.
- [175] M. Ptito, P. Johannsen, J. Faubert, and A. Gjedde. Activation of human extrageniculostriate pathways after damage to area v1. *Neuroimage*, 9(1):97–107, 1999.
- [176] A. Pulkkinen, Y. Huang, J. Song, and K. Hynynen. Simulations and measurements of transcranial low-frequency ultrasound therapy: skull-base heating and effective area of treatment. *Physics in Medicine and Biology*, 56(15):4661, 2011.
- [177] L. A. Robinson, J. S. Berman, and R. A. Neimeyer. Psychotherapy for the treatment of depression: a comprehensive review of controlled outcome research. *Psychological bulletin*, 108(1):30, 1990.
- [178] D. Royer and O. Casula. Quantitative imaging of transient acoustic fields by optical heterodyne interferometry. In , *1994 IEEE Ultrasonics Symposium, 1994. Proceedings*, volume 2, pages 1153–1162 vol.2, 1994.
- [179] M. S, S. S, C. S, and V. JL. History, applications, and mechanisms of deep brain stimulation. *JAMA Neurology*, 70(2):163–171, 2013.
- [180] P. M. Salkovskis. Understanding and treating obsessive—compulsive disorder. *Behaviour Research and Therapy*, 37:S29–S52, 1999.
- [181] J. Sallet, R. B. Mars, M. P. Noonan, F.-X. Neubert, S. Jbabdi, J. X. O’Reilly, N. Filippini, A. G. Thomas, and M. F. Rushworth. The organization of dorsal frontal cortex in humans and macaques. *Journal of Neuroscience*, 33(30):12255–12274, 2013.
- [182] J. H. Sandell and P. H. Schiller. Effect of cooling area 18 on striate cortex cells in the squirrel monkey. *Journal of Neurophysiology*, 48(1):38–48, 1982.
- [183] E. Sassaroli and N. Vykhodtseva. Acoustic neuromodulation from a basic science prospective. *Journal of Therapeutic Ultrasound*, 4:17, 2016.

- [184] J. D. Schall. Neuronal activity related to visually guided saccades in the frontal eye fields of rhesus monkeys: comparison with supplementary eye fields. *Journal of neurophysiology*, 66(2):559–579, 1991.
- [185] J. D. Schall. Visuomotor areas of the frontal lobe. In *Extrastriate cortex in primates*, pages 527–638. Springer, 1997.
- [186] M. Schlag-Rey, N. Amador, H. Sanchez, and J. Schlag. Antisaccade performance predicted by neuronal activity in the supplementary eye field. *Nature*, 390(6658):398, 1997.
- [187] M. C. Schmid, T. Panagiotaropoulos, M. A. Augath, N. K. Logothetis, and S. M. Smirnakis. Visually driven activation in macaque areas v2 and v3 without input from the primary visual cortex. *PLoS One*, 4(5):e5527, 2009.
- [188] S. A. Shah and N. D. Schiff. Central thalamic deep brain stimulation for cognitive neuromodulation—a review of proposed mechanisms and investigational studies. *European Journal of Neuroscience*, 32(7):1135–1144, 2010.
- [189] L.-A. Sieu, A. Bergel, E. Tiran, T. Deffieux, M. Pernot, J.-L. Gennisson, M. Tanter, and I. Cohen. Eeg and functional ultrasound imaging in mobile rats. *Nature methods*, 12(9):831, 2015.
- [190] A. Sillito. The contribution of inhibitory mechanisms to the receptive field properties of neurones in the striate cortex of the cat. *The Journal of physiology*, 250(2):305–329, 1975.
- [191] A. Sillito. The effectiveness of bicuculline as an antagonist of gaba and visually evoked inhibition in the cat’s striate cortex. *The Journal of physiology*, 250(2):287–304, 1975.
- [192] A. M. Sillito, J. Cudeiro, and H. E. Jones. Always returning: feedback and sensory processing in visual cortex and thalamus. *Trends in Neurosciences*, 29(6):307–316, 2006.
- [193] J. Silvanto, N. Lavie, and V. Walsh. Double dissociation of v1 and v5/mt activity in visual awareness. *Cerebral Cortex*, 15(11):1736–1741, 2005.
- [194] L. C. Sincich, K. F. Park, M. J. Wohlgenuth, and J. C. Horton. Bypassing v1: a direct geniculate input to area mt. *Nature neuroscience*, 7(10):1123, 2004.

- [195] J. E. Soneson and E. S. Ebbini. A User-Friendly Software Package for HIFU Simulation. *AIP Conference Proceedings*, 1113(1):165–169, 2009.
- [196] D. J. Stein. Obsessive-compulsive disorder. *The Lancet*, 360(9330):397–405, 2002.
- [197] V. Stuphorn and J. D. Schall. Executive control of countermanding saccades by the supplementary eye field. *Nature neuroscience*, 9(7):925, 2006.
- [198] P. R. Szeszko, D. Robinson, J. M. J. Alvir, R. M. Bilder, T. Lencz, M. Ashtari, H. Wu, and B. Bogerts. Orbital frontal and amygdala volume reductions in obsessive-compulsive disorder. *Archives of general psychiatry*, 56(10):913–919, 1999.
- [199] W. H. Theodore and R. S. Fisher. Brain stimulation for epilepsy. *The Lancet Neurology*, 3(2):111–118, 2004.
- [200] G. Thickbroom, R. Stell, and F. Mastaglia. Transcranial magnetic stimulation of the human frontal eye field. *Journal of the neurological sciences*, 144(1):114–118, 1996.
- [201] W. T. Thomson. Transmission of Elastic Waves through a Stratified Solid Medium. *Journal of Applied Physics*, 21(2):89–93, 1950.
- [202] G. Thut and A. Pascual-Leone. A review of combined tms-eeeg studies to characterize lasting effects of repetitive tms and assess their usefulness in cognitive and clinical neuroscience. *Brain topography*, 22(4):219, 2010.
- [203] P.-H. Tsui, S.-H. Wang, and C.-C. Huang. In vitro effects of ultrasound with different energies on the conduction properties of neural tissue. *Ultrasonics*, 43(7):560–565, 2005.
- [204] Y. Tufail, A. Matyushov, N. Baldwin, M. L. Tauchmann, J. Georges, A. Yoshihiro, S. I. H. Tillery, and W. J. Tyler. Transcranial pulsed ultrasound stimulates intact brain circuits. *Neuron*, 66(5):681–694, 2010.
- [205] Y. Tufail, A. Matyushov, N. Baldwin, M. L. Tauchmann, J. Georges, A. Yoshihiro, S. I. H. Tillery, and W. J. Tyler. Transcranial Pulsed Ultrasound Stimulates Intact Brain Circuits. *Neuron*, 66(5):681–694, 2010.
- [206] Y. Tufail, A. Yoshihiro, S. Pati, M. M. Li, and W. J. Tyler. Ultrasonic neuromodulation by brain stimulation with transcranial ultrasound. *Nature Protocols*, 6(9):1453–1470, 2011.

- [207] W. J. Tyler, Y. Tufail, M. Finsterwald, M. L. Tauchmann, E. J. Olson, and C. Majestic. Remote Excitation of Neuronal Circuits Using Low-Intensity, Low-Frequency Ultrasound. *PLOS ONE*, 3(10):e3511, 2008.
- [208] C. V, S. G, J. F, V. N, and H. K. Focused ultrasound effects on nerve action potential in vitro., Focused ultrasound effects on nerve action potential in vitro. *Ultrasound in medicine & biology*, *Ultrasound in medicine & biology*, 35, 35(10, 10):1737, 1737–1747, 2009.
- [209] N. M. van Gelder and K. a. C. Elliott. Disposition of gamma-aminobutyric acid administered to mammals. *Journal of Neurochemistry*, 3(2):139–143, 1958.
- [210] N. Vykhodtseva and I. Konopatskaya. 6a-4 focused ultrasound potential to initiate spreading depression for disruption of blood brain barrier. In *Ultrasonics Symposium, 2007. IEEE*, pages 428–431, 2007.
- [211] N. I. Vykhodtseva, K. Hynynen, and C. Damianou. Histologic effects of high intensity pulsed ultrasound exposure with subharmonic emission in rabbit brain in vivo. *Ultrasound in Medicine & Biology*, 21(7):969–979, 1995.
- [212] V. Walsh and A. Cowey. Transcranial magnetic stimulation and cognitive neuroscience. *Nature Reviews Neuroscience*, 1(1):73–80, 2000.
- [213] H. Wang, M. Kim, K. P. Normoyle, and D. Llano. Thermal Regulation of the Brain—An Anatomical and Physiological Review for Clinical Neuroscientists. *Frontiers in Neuroscience*, 9, 2016.
- [214] E. M. Wassermann and S. H. Lisanby. Therapeutic application of repetitive transcranial magnetic stimulation: a review. *Clinical Neurophysiology*, 112(8):1367–1377, 2001.
- [215] N. Wattiez, C. Constans, T. Deffieux, P. M. Daye, M. Tanter, J.-F. Aubry, and P. Pouget. Transcranial ultrasonic stimulation modulates single-neuron discharge in macaques performing an antisaccade task. *Brain Stimulation*, 2017.
- [216] D. R. White, H. Q. Woodard, and S. M. Hammond. Average soft-tissue and bone models for use in radiation dosimetry. *The British Journal of Radiology*, 60(717):907–913, 1987.

- [217] S. P. Wise. Forward frontal fields: phylogeny and fundamental function. *Trends in neurosciences*, 31(12):599–608, 2008.
- [218] M. Woolrich. Robust group analysis using outlier inference. *Neuroimage*, 41(2):286–301, 2008.
- [219] M. W. Woolrich, T. E. Behrens, C. F. Beckmann, M. Jenkinson, and S. M. Smith. Multilevel linear modelling for fmri group analysis using bayesian inference. *Neuroimage*, 21(4):1732–1747, 2004.
- [220] F.-Y. Yang, T.-T. Wong, M.-C. Teng, R.-S. Liu, M. Lu, H.-F. Liang, and M.-C. Wei. Focused ultrasound and interleukin-4 receptor-targeted liposomal doxorubicin for enhanced targeted drug delivery and antitumor effect in glioblastoma multiforme. *Journal of controlled release*, 160(3):652–658, 2012.
- [221] P. S. Yang, H. Kim, W. Lee, M. Bohlke, S. Park, T. J. Maher, and S.-S. Yoo. Transcranial Focused Ultrasound to the Thalamus Is Associated with Reduced Extracellular GABA Levels in Rats. *Neuropsychobiology*, 65(3):153–160, 2012.
- [222] P. P. Ye, J. R. Brown, and K. B. Pauly. Frequency Dependence of Ultrasound Neurostimulation in the Mouse Brain. *Ultrasound in Medicine & Biology*, 2016.
- [223] S.-S. Yoo, A. Bystritsky, J.-H. Lee, Y. Zhang, K. Fischer, B.-K. Min, N. J. McDannold, A. Pascual-Leone, and F. A. Jolesz. Focused ultrasound modulates region-specific brain activity. *NeuroImage*, 56(3):1267–1275, 2011.
- [224] S.-S. Yoo, A. Bystritsky, J.-H. Lee, Y. Zhang, K. Fischer, B.-K. Min, N. J. McDannold, A. Pascual-Leone, and F. A. Jolesz. Focused ultrasound modulates region-specific brain activity. *NeuroImage*, 56(3):1267–1275, 2011.
- [225] S.-S. Yoo, H. Kim, B.-K. Min, and S. P. Eric Franck. Transcranial Focused Ultrasound to the Thalamus Alters Anesthesia Time in Rats. *Neuroreport*, 22(15):783–787, 2011.
- [226] K. Yoshida and L. A. Benevento. The projection from the dorsal lateral geniculate nucleus of the thalamus to extrastriate visual association cortex in the macaque monkey. *Neuroscience Letters*, 22(2):103–108, 1981.

- [227] Y. Younan, T. Deffieux, B. Larrat, M. Fink, M. Tanter, and J.-F. Aubry. Influence of the pressure field distribution in transcranial ultrasonic neurostimulation. *Medical Physics*, 40(8):082902, 2013.

Résumé de thèse

Introduction générale

L'histoire de la neuromodulation par ultrasons a commencé dans les années 1960, avec la découverte par William Fry de la possibilité d'initier la décharge neuronale par ultrasons [54]. L'essor de la stimulation ultrasonore a réellement eu lieu dans les années 2000 avec l'élicitation de mouvements sur des rongeurs sans effets secondaires par ultrasons basse fréquence et de faible intensité [204, 225, 227, 101]. Non invasive et peu risquée, capable d'atteindre des structures profondes à des résolutions millimétriques, la technique porte l'espoir d'applications cliniques peu coûteuses, sûres et faciles à mettre en place.

Le mécanisme par lequel les ultrasons induisent l'apparition de potentiels d'action (PA) dans les neurones est à l'heure actuelle mal compris. Il y a cependant consensus sur un effet mécanique prédominant par rapport à un effet thermique [31]. Le rôle des canaux ioniques a également été mis en avant par plusieurs études expérimentales [207]. Plusieurs modèles ont été proposés pour expliquer l'initiation des PA par ultrasons, tous basés sur le modèle électrique d'Hodgkin et Huxley pour la propagation des PA dans un neurone. Le modèle du **soliton** [74], s'appuyant sur les propriétés thermodynamiques et les transitions de phase des lipides constituant la membrane cellulaire, considère le PA comme la propagation d'une impulsion de densité. Comme les constantes élastiques varient sous l'effet de forces mécaniques, ce modèle pourrait expliquer comment les ultrasons peuvent générer un PA. Le **modèle flexoélectrique** [164] fait l'hypothèse que le changement de courbure de la membrane, induit par les ultrasons, modifie proportionnellement le potentiel de la membrane. L'effet inverse pourrait expliquer qualitativement les effets mécaniques observés au cours de la propagation d'un PA; cependant aucune équation ne peut pour l'instant

prédire la naissance d'un PA par cet effet seul. Enfin le modèle d'**excitation neuronale par cavitation intramembranaire** [168] prédit la formation de nanobulles entre les deux feuillets de la membrane sous l'effet des ultrasons. En oscillant, ces nanobulles induiraient un changement de courbure et un courant alternatif à travers la membrane. Incluant ces termes additionnels, l'équation de Hodgkin et Huxley admet une solution qui décrit la génération d'un PA.

Par son action sur le cerveau, la stimulation par ultrasons pourrait avoir des applications dans le traitement des maladies neurodégénératives. Ces maladies sont caractérisées par la mort prématurée des neurones du système nerveux central, entraînant des dysfonctionnements physiologiques, moteurs et/ou mentaux. Etant donné le vieillissement global de la population, ces maladies gravement invalidantes concernent un nombre croissant de personnes et constituent donc un enjeu majeur de la recherche actuelle. Plus d'un million de français en souffrent aujourd'hui (figure 8.1). Plus largement, les troubles neurologiques et psychiatriques impactent 1 milliard de personnes de tous âges dans le monde: l'épilepsie affecte 0.5 à 1% de la population, la dépression 5 à 15%[39], les troubles obsessionnels compulsifs (TOC) 2 à 3% [40].

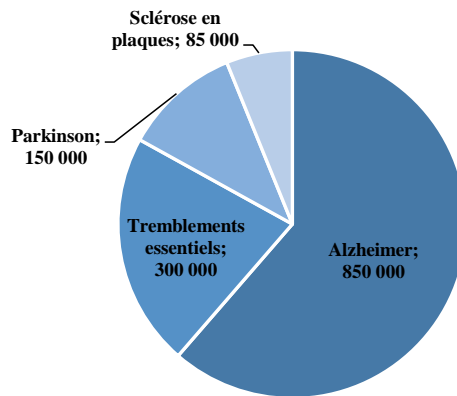


Figure 8.1: Les principales maladies neurodégénératives en France

Pour la plupart des maladies neurodégénératives, le mécanisme et les symptômes sont connus mais la cause est encore mal comprise. Par conséquent, les traitements combattent uniquement les symptômes et il n'existe pas de véritable remède à l'heure actuelle. Certains médicaments permettent le ralentissement de la dégénérescence des neurones dans les cas des maladies d'Alzheimer et de

Parkinson, mais leur action n'est pas efficace sur 100% des patients, limitée dans le temps et leurs effets secondaires peuvent altérer leur tolérabilité. Dans le cas de la dépression, les effets secondaires sont parfois si importants que les patients arrêtent le traitement [158]. Les troubles psychiatriques comme la dépression et les TOC peuvent également être combattus par la psychothérapie dans les cas les moins sévères, et en combinaison avec les médicaments dans les cas les plus graves [160, 177].

La **neurostimulation**, de manière générale, s'est avérée efficace comme traitement de ces maladies, sans que le mécanisme de guérison soit complètement compris. Plusieurs techniques existent pour activer des régions spécifiques du cerveau. La **stimulation cérébrale profonde** est une méthode invasive nécessitant l'implantation d'électrodes dans les régions du cerveau que l'on souhaite exciter. Des impulsions électriques, générées par un stimulateur implanté sous la clavicule, sont ainsi envoyées au cerveau via ces électrodes. Cette technique est utilisée depuis plusieurs décennies, approuvée par la "Food and Drug Administration" américaine depuis 1997 pour le traitement de la maladie de Parkinson. Malgré son efficacité dans un grand nombre de maladies (tremblements essentiels, épilepsie, dépression, TOC, syndrome de Tourette, addictions...), des risques importants restent liés à la chirurgie d'implantation des électrodes [18]. La **stimulation magnétique transcrânienne** repose sur le courant induit dans le cerveau par les variations d'un champ magnétique appliqué près du crâne au moyen d'une bobine. Cette méthode, non invasive, est aussi utilisée dans un grand nombre de maladies neurologiques et ses effets secondaires se limitent à l'inconfort de la procédure mais son efficacité est limitée aux zones corticales. La **stimulation transcrânienne en courant direct**, quant à elle, consiste en l'application d'un courant de faible intensité par des électrodes placées sur la tête. Le courant électrique circule ainsi dans les régions corticales et sous-corticales qui séparent les électrodes. Les problèmes se limitent ici à la chauffe ou irritation de la peau sous les électrodes, et la résolution spatiale est pauvre.

Enfin, la **stimulation par ultrasons focalisés** se révèle comme une alternative prometteuse aux techniques de stimulation électriques, combinant non invasivité, précision spatiale et aptitude à atteindre les structures cérébrales profondes. Cependant, les paramètres ultrasonores doivent être optimisés pour augmenter l'amplitude des effets, comprendre ses mécanismes et assurer la sécurité de la procédure: les effets observés sont à l'heure actuelle limités à quelques minutes

[33, 223], et l'augmentation de température pourrait induire des lésions des tissus [112, 31] si la durée de la stimulation n'est pas correctement ajustée. Dans cette thèse, l'échauffement associés à la neurostimulation ultrasonore et la dépendance en fréquence ont été estimés numériquement et expérimentalement: il est inférieur à 0.01°C pour toutes nos expérimentations. Pour évaluer physiologiquement les effets des ultrasons à l'échelle cellulaire, l'activité de neurones a été mesurée individuellement sur un macaque éveillé pendant une neuromodulation ultrasonore. Afin d'allonger la durée de la modulation, une séquence ultrasonore de 20 secondes a été testée avec succès sur des singes exécutant une tâche oculomotrice. Pour prouver la faisabilité d'étudier la connectivité cérébrale avec les ultrasons, l'IRM fonctionnel a été utilisée après neurostimulation sur singes anesthésiés. Enfin, l'activité visuelle de macaques a été partiellement inhibée par ouverture de barrière hémato-encéphalique par ultrasons et délivrance d'un neurotransmetteur inhibiteur, établissant la preuve de concept pour la délivrance non invasive et localisée de médicaments chez le primates et pour l'étude de la connectivité cérébrale par introduction, sans injection directe, d'agents neuro-actifs dans le cerveau.

Simulations numériques et estimation de l'élévation de température lors d'une stimulation ultrasonore

Paramètres de simulations numériques

La propagation des ultrasons est fortement altérée par les changements abrupts de milieu, comme le passage des tissus mous au crâne. Lors d'une stimulation transcranienne, l'onde ultrasonore va être non seulement atténuée par le crâne mais aussi déformée: le passage du crâne déforme le front d'onde et, de plus, la boîte crânienne forme une cavité dans laquelle apparaissent des interférences constructives et destructives. Comme il est impossible de mesurer expérimentalement le champ de pression dans le cerveau, les simulations numériques constituent un outil de grande valeur pour prédire l'amplitude et la forme du champ de pression derrière le crâne.

Les simulations ont été effectuées avec k-Wave, un code basé sur une méthode pseudo-spectrale. Les cartes en 3D de crâne, tissus et cerveau ont été extraites à partir de scans (μ)CT de rats et singes. Le crâne de rat a été considéré homogène, car les variations de densités sont petites

devant la longueur d'onde des ultrasons, donc l'onde ne les "voit" pas ($\lambda \sim 1$ à 7 mm dans l'os pour les fréquences considérées). En revanche, les crânes de singes présentent de fortes hétérogénéités internes et leur taille est supérieure à la longueur d'onde. Une relation linéaire a donc été utilisée pour traduire les unités Hounsfield des scans en valeurs de densité et vitesse du son dans le cas des primates non humains. L'absorption dépend à la fois du milieu et de la fréquence: $abs = \alpha_0 f^b \Phi^\beta$, où la porosité ϕ est définie par $\Phi = \frac{\rho_{max} - \rho}{\rho_{max} - \rho_{eau}}$ dans le crâne. La transmission à travers le morceau de crâne dans l'eau, à quatre fréquences différentes et en différents points, a été relevée. En parallèle, des simulations de la propagation aux mêmes fréquences ont été effectuées à partir du scan de ce même morceau de crâne. En ajustant les paramètres $\rho_{max}, c_{max}, \beta, \alpha_0$ et b lors des simulations pour retrouver les résultats expérimentaux, un optimum a été trouvé, indiquant les valeurs les plus adaptées au crâne de singe pour ces paramètres. Les tissus mous, quant à eux, présentent peu de variations et ont été considérés homogènes chez le rat et chez le singe. La propagation ultrasonore a été simulée depuis le transducteur (une coupole sphérique) jusqu'à la tête en passant par un cône d'eau, pendant une durée suffisante pour atteindre l'état stationnaire.

Code thermique

Une fois obtenu le champ de pression après simulation de la propagation ultrasonore, il est possible de calculer l'élévation de température à partir de l'équation de la chaleur en milieu biologique:

$$\rho C \frac{\partial T}{\partial t} = \kappa \nabla^2 T + q + w \rho_s C_s (T - T_a)$$

où T, ρ, C, κ et q sont respectivement la température, la densité, la capacité calorifique, la conductivité thermique et le taux de production de chaleur défini comme $q = \alpha \frac{P^2}{2\rho C}$, α étant l'absorption et P l'amplitude de pression. Le dernier terme correspond à la perfusion, w, ρ_s, C_s et T_a étant respectivement le taux de perfusion dans le sang, la masse volumique du sang, la capacité calorifique du sang et la température ambiante sanguine. La dose thermique, qui permet d'évaluer les dommages infligés au tissu lors d'un stress thermique, est donnée par

$$DT = \int R^{43-T} dt$$

où $R = 0.25$ si $T < 43$ et $R = 0.5$ si $T > 43$ [38]. Son unité est le CEM (cumulative equivalent

minutes at $43^{\circ}C$).

Afin de le valider, ce modèle thermique a été comparé au simulateur HIFU (High Intensity Focused Ultrasound) proposé par la FDA pour estimer l'élévation de température en milieu homogène. En faisant tourner les mêmes simulations avec les 2 modèles (à 0.5 MHz, 1 MHz et 1.5 MHz dans un tissu absorbant), la déviation maximale entre les résultats était inférieure à 9%.

Estimation rétrospective de l'élévation de température: sept études chez le rongeurs

Devant l'augmentation progressive des doses ultrasonores employées (en puissance et/ou en durée de stimulation) dans la littérature, nous avons jugé utile d'estimer les élévations de température et doses thermiques afin, d'une part, d'éviter les lésions dans la peau et le cerveau, et d'autre part, d'exclure le mécanisme thermique du mode d'action des ultrasons (un effet thermique pourrait fausser les interprétations de résultat lors de la recherche de paramètres optimaux).

Les paramètres du code thermique (taille du transducteur, durée et puissance de la stimulation) ont été adaptés à sept différentes configurations précédemment publiées (Younan *et al*, Kamimura *et al*, Li *et al*, Yang *et al*, Ye *et al*) (table 8.1). Pour six d'entre eux, la prédiction d'élévation de température est inférieure à $0.01^{\circ}C$, donc négligeable. En revanche, la dernière stimulation (Kamimura *et al* [96]), d'une durée de 20 secondes avec un rapport cyclique de 50% et une pression de 1.9 MPa dans le cerveau, entraînerait une augmentation de $7^{\circ}C$ dans le cerveau (figure 8.2), correspondant à une dose thermique de 15 CEM (en comparaison, les seuils de dose thermique reportés dans la littérature pour les lésions dans le cerveau varient entre 17.5 et 25 CEM). Ces résultats ont été corroborés par des mesures de température sous-cutanée sur la tête souris à l'aide d'un thermocouple, durant deux stimulations différentes, une "faible" (Ye *et al*) et une "forte" (Kamimura *et al*) (figure 8.3).

Des simulations supplémentaires ont montré que pour éviter une telle augmentation de température, il est possible de réduire uniquement le rapport cyclique tout en gardant une amplitude de pression identique afin de conserver l'efficacité de la stimulation. En gardant la même configuration "stimulation forte" mais avec un rapport cyclique de 25% au lieu de 50%, la variation de température est

Table 8.1: Paramètres et résultats dans le cerveau et au point focal. La température de base est $37^{\circ}C$.

Setup #	Groupe	f_0	Temps de cycle	longueur du tir (ms)	Temps total de tir	Pression maximale dans le cerveau (MPa)	Temperature au point focal (Elevation de température $\Delta T(^{\circ}C)$)	Température maximale dans le cerveau (Elevation de température $\Delta T(^{\circ}C)$)
1	Younan et al	320 kHz	50 %	0.23	250ms	0.95	37.01 ($\Delta T = 0.01$)	37.06 ($\Delta T = 0.06$)
2		500 kHz				0.3	37.001 ($\Delta T = 0.001$)	37.007 ($\Delta T = 0.007$)
3	Ye et al	1.4 MHz	100%	80	80ms	0.3	37.002 ($\Delta T = 0.002$)	37.02 ($\Delta T = 0.02$)
4		1.9 MHz				1.6	37.07 ($\Delta T = 0.07$)	37.8 ($\Delta T = 0.8$)
5	Li et al	1 MHz	50%	0.5	300ms	0.12	37.0005 ($\Delta T = 0.0005$)	37.006 ($\Delta T = 0.006$)
6		5 MHz				0.16	37.003 ($\Delta T = 0.003$)	37.07 ($\Delta T = 0.07$)
7	Yang et al	650 kHz	5%	0.5	20min	0.45	37.03 ($\Delta T = 0.03$)	37.07 ($\Delta T = 0.07$)
8	Kamimura et al	1.9 MHz	50%	0.5	20s 1s on, 1s off	1.9	38.3 ($\Delta T = 1.3$)	44 ($\Delta T = 7.0$)

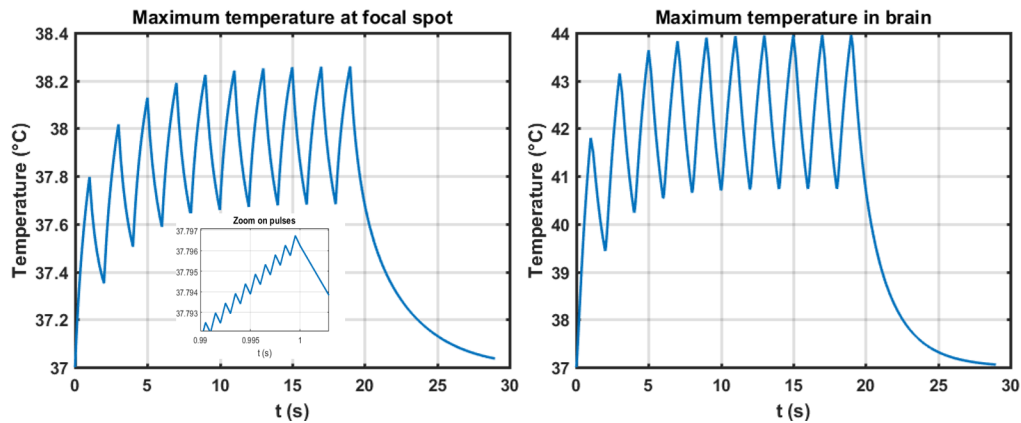


Figure 8.2: Estimation de l'élévation de température à 1.9 MHz, 1.9 MPa [96]

divisée par 2. En conclusion, la température est un élément à prendre en compte lors de la conception des expériences de neurostimulation ultrasonore et peut être facilement évaluée par simulations numériques. En plus de supprimer les risques de lésions, restreindre l'élévation thermique permet de ne pas faire interférer les effets mécaniques et les effets thermiques dans la compréhension du

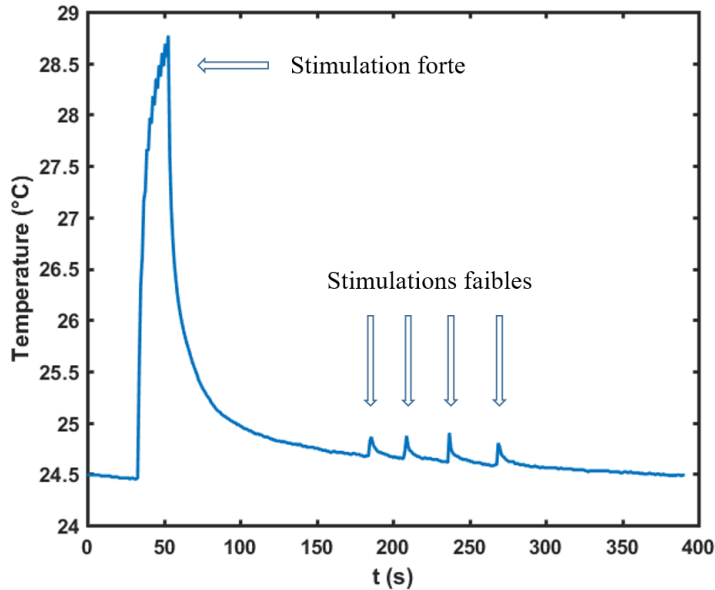


Figure 8.3: Mesure de température dans la peau d’une souris au niveau du crâne durant deux séquences ultrasonores différentes: stimulation forte (Kamimura et al) et faible (Ye et al)

mécanisme de neurostimulation. En effet, bien que les effets thermiques sont communément reconnus comme négligeables dans ce phénomène, une forte élévation de température affecte néanmoins les neurones (ne serait-ce que les propriétés physiques de la membrane cellulaire), jusqu’à décharger 1.1 impulsion/s/°C supplémentaire [23]. Dans une démarche d’investigation du mécanisme de la création et des potentiels d’action par les ultrasons, il est donc nécessaire de s’affranchir de tels effets parasites.

Vers une stimulation ultrasonore multifréquentielle

L’aptitude des ultrasons à déclencher des potentiels d’action a été démontrée, par différents groupes, entre 320 kHz et 1.9 MHz. D’après le modèle théorique de cavitation intramembranaire (Plaksin et al. 2014), le seuil d’activation en intensité ultrasonore pour la neurostimulation ne dépend pas de la fréquence. Cependant, il est difficile de comparer entre elles des études effectuées par différents groupes et avec différents transducteurs: pour vérifier l’hypothèse de Plaksin et al., il faudrait une étude multifréquentielle réalisée sur le même animal, dans les mêmes conditions. Cela permettrait également de trouver la fréquence la plus efficace: il existe un équilibre à trouver

entre les basses fréquences, de faible résolution spatiale ($\lambda=7.5\text{mm}$ dans l'eau à 1380 kHz) mais peu atténuées par le crâne, et les hautes fréquences plus fines ($\lambda=1\text{mm}$ dans l'eau à 200 kHz) mais très absorbées sur leur passage. Nous proposons ici d'utiliser un transducteur quadri-bande pour effectuer de telles mesures sur une large bande de fréquence. Nous modélisons le champ de pression à chaque fréquence dans le cerveau d'un rat et de deux singes (un mâle et une femelle) grâce au modèle numérique. Après calibration du transducteur dans l'eau aux quatre fréquences (200 kHz, 320 kHz, 850 kHz, 1380 kHz), les simulations ont été mises à l'échelle des puissances maximales obtenues.

Les résultats chez le rat (figure 8.4, 1ère ligne) montrent qu'à basses fréquences apparaissent des interférences si prononcées que la notion de tâche focale disparaît et une grande partie du cerveau est sous influence des ultrasons. Le crâne de rat forme une cavité particulièrement efficace, avec un rapport d'onde stationnaire (défini comme le maximum d'un ventre de pression sur le minimum du noeud de pression adjacent, le long de l'axe de propagation) atteignant 3.67 à 200 kHz. A haute fréquence en revanche, la forme de la tâche focale paraît peu affectée par le crâne: le rapport d'onde stationnaire est très proche de 1. Le crâne de rat étant très fin, l'absorption, bien que présente, ne semble pas suffisante pour altérer l'efficacité de la neurostimulation: la pression peut atteindre 6 MPa à 850 kHz et 1380 kHz.

Chez le singe (figure 8.4, 2ème et 3ème ligne), la cavité formée par le crâne est bien plus grande devant la longueur d'onde et le crâne est nettement plus épais, surtout chez le singe mâle. Par conséquent, peu d'ondes stationnaires apparaissent à basses fréquences et les hautes fréquences sont drastiquement atténuées: chez le mâle, la pression est de seulement 1.1 MPa à 1380 kHz, équivalent à un facteur de transmission de 13%. Il est intéressant de noter ici que malgré leur appartenance à la même espèce, la différence de géométrie entre les crânes des deux singes entraîne une grande variation de transmission de l'onde ultrasonore. A titre d'exemple, à 1380 kHz, la transmission est de 13% chez le mâle et 61% chez la femelle. L'épaisseur du crâne y joue un grand rôle, d'une part par son absorption qui en dépend exponentiellement, mais aussi par les phénomènes complexes de réflexions multiples ayant lieu dans l'os et dont l'issue (constructive ou destructive) dépend de l'écart entre l'épaisseur et un multiple de $\lambda/4$.

Cette étude souligne l'importance de la géométrie du crâne de l'animal dans la propagation de l'onde ultrasonore: l'effet sur l'atténuation et la forme du champ de pression, notamment

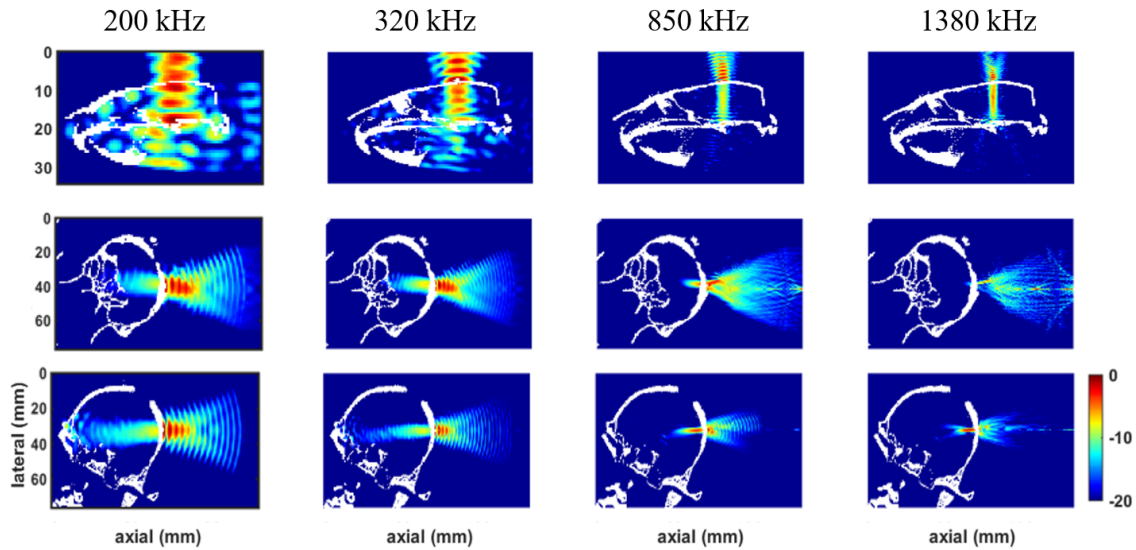


Figure 8.4: Résultats de simulations chez le rat (1ère ligne), le singe mâle (2ème ligne) et le singe femelle (3ème ligne)

l'apparition d'ondes stationnaires, ne peut pas être prédit sur la simple base de l'épaisseur du crâne ni même de l'espèce animale. Les simulations numériques sont nécessaires pour comprendre l'action précise des ultrasons sur le cerveau lors d'une stimulation et ainsi optimiser les paramètres ultrasonores en fonction du sujet.

Stimulation ultrasonore transcranienne pour la modulation de la décharge d'un unique neurone chez le macaque lors d'une tâche antisaccade

Dans l'optique de mieux comprendre les mécanismes physiologiques à l'oeuvre lors d'une neurostimulation ultrasonore, nous démontrons ici la faisabilité d'enregistrer l'activité d'un neurone unique pendant une stimulation chez le primate non-humain éveillé au cours d'une tâche d'antisaccade. Pendant cette tâche, très étudiée dans le cadre de la maladie de Parkinson car elle implique des mécanismes de prédiction et de mémoire altérés chez les patients concernés [5, 50, 6], l'animal est entraîné à diriger son regard à l'opposé d'une cible apparaissant périodiquement sur un écran. Les

impulsions ultrasonores ont été envoyées dans l'aire oculomotrice frontale (Frontal Eye Field, FEF) tandis que les enregistrements électrophysiologiques avaient lieu dans aire oculomotrice frontale supplémentaire (Supplementary Eye Field, SEF) au moyen d'une électrode. Ces deux régions étant sollicitées lors de la tâche anti-saccade et fortement interconnectées, cette configuration permet de détecter le changement d'activité liée à la stimulation sans souffrir d'éventuelles interférences directes entre les ultrasons et l'électrode. Deux macaques ont participé à cette étude. Des simulations numériques, basées sur leurs scans respectifs, ont été réalisées afin de prédire l'amplitude de pression dans le cerveau. Les mesures électrophysiologiques ont détecté une perturbation significative ($p < 0.01$) de l'activité pour 40% des neurones lors de la stimulation par rapport à la condition sans stimulation. Environ la moitié ont eu une activité réduite, l'autre moitié une activité accrue (exemple figure 8.5).

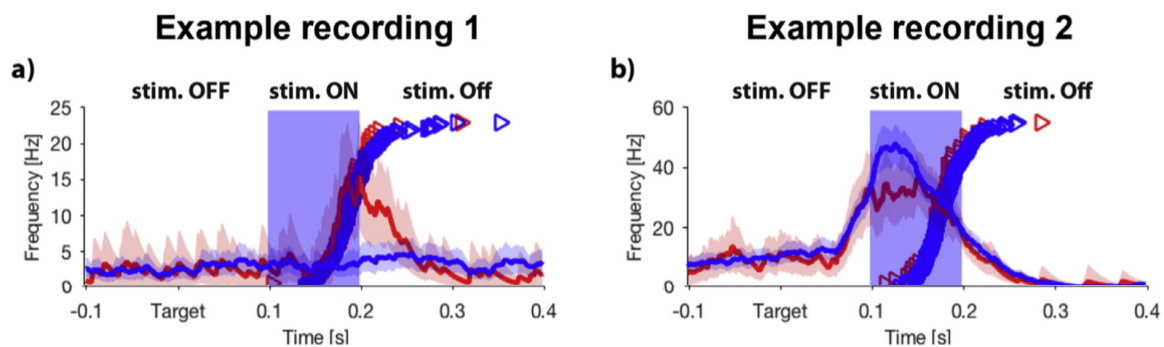


Figure 8.5: Fréquence de décharge neuronale avec (ligne rouge) ou sans (ligne bleue) simulation ultrasonore pour 2 neurones pris comme exemples: l'un présentant une activité accrue (gauche), l'autre une activité diminuée (droite) par les ultrasons. La surface bleutée représente l'intervalle de tir ultrasonore. Les triangles représentent les latences cumulées d'antisaccade.

Ce taux de sensibilité des neurones aux ultrasons de 40% peut s'expliquer par le fait que malgré la forte connexion entre le SEF et le FEF, tous les neurones du SEF ne sont pas sujets à des projections du FEF. Des mesures contrôles ont été effectuées avec l'enregistrement toujours dans le SEF, mais la région de stimulation dans le cortex visuel (beaucoup moins connecté au FEF). Dans ces conditions, seul un neurone sur 20 a eu une activité significativement perturbée. En montrant la possibilité d'étudier directement l'activité des neurones, cette technique ouvre la voie à des études d'optimisation des paramètres ultrasonores pour la neurostimulation, qui permettraient de mieux comprendre les mécanismes électrophysiologiques en jeu.

Stimulation Ultrasonore Transcranienne répétée

Malgré tous les avantages compétitifs que présente la neurostimulation ultrasonore (non invasive, sûre, précise et capable d'atteindre des zones profondes) par rapport aux autres techniques comme la stimulation cérébrale profonde, la stimulation magnétique transcranienne ou la stimulation transcranienne à courant direct, la faible durée de ses effets apparaît comme un facteur limitant dès lors que l'on s'intéresse à ses applications thérapeutiques. Jusqu'à récemment, ainsi que dans l'étude précédente, les effets reportés étaient limités à quelques centaines de millisecondes. Dallapiazza et al. (2017) ont ensuite réussi à étendre l'inhibition des neurones du thalamus à 10 minutes. Nous présentons ici les effets d'une stimulation ultrasonore transcranienne répétée sur le cortex oculomoteur de macaques au cours de tâches anti-saccades. Les ultrasons, à la fréquence de 320 kHz, ont été émis pendant 20s avec un rapport cyclique de 30% (impulsions de 30 ms à une fréquence de répétition de 10 Hz). La puissance envoyée correspondait à une amplitude de pression de 0.76 MPa dans l'eau, et environ 0.44 MPa dans le cerveau d'après une estimation de la transmission à travers le crâne de 58%. La cible était, selon la séance, le FEF, le SEF, le cortex moteur (région contrôle) ou le cortex visuel (région contrôle), étant donné que le SEF et le FEF sont fortement sollicités lors de la tâche anti-saccade.

L'analyse des résultats s'est basée sur la mesure du temps de latence: durée entre l'apparition de la cible et le mouvement oculaire de l'animal, dans la direction opposée à la cible. La moyenne des temps de latence pendant une séance post-stimulation a été comparée avec celle d'une séance non précédée de stimulation. Les résultats montrent qu'une diminution significative des temps de latence du FEF et SEF a lieu sur les mouvements ipsilatéraux (figure 8.6), jusqu'à 25 minutes après la stimulation. En revanche sur les sessions contrôle, où la stimulation a lieu au niveau du cortex moteur ou du cortex visuel, aucune modulation significative des temps de latence n'apparaît.

Cette étude démontre la possibilité de prolonger dans le temps les effets modulateurs des ultrasons sur le cerveau, et apporte ainsi l'espoir de développer des applications thérapeutiques pour le traitement de maladies neurodégénératives et de troubles neurologiques.

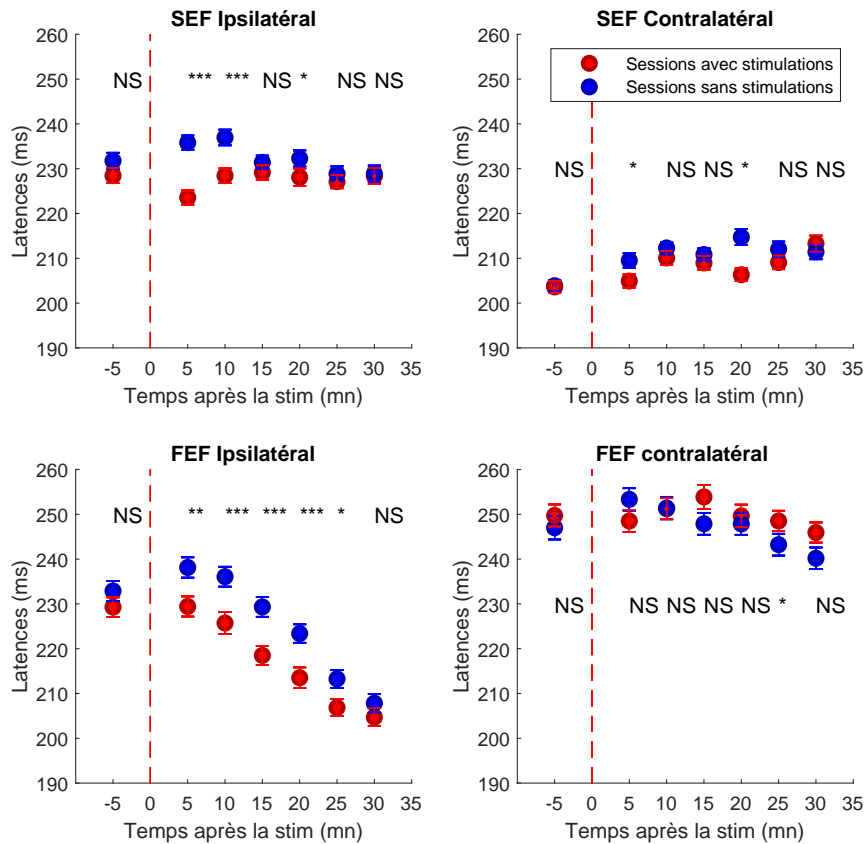


Figure 8.6: Moyenne des temps de latence (en ms), dans les conditions SEF et FEF (haut et bas, respectivement) et en fonction de la direction du mouvement (ipsilatéral (gauche) et contralatéral (droite)). Les données ont été moyennées sur toutes les sessions. Les barres d'erreurs représentent l'écart-type normalisé. Les astérisques indiquent la significativité affectée aux latences avec stimulation par rapport à la baseline (NS: non significatif; * $p < 0.05$; ** $p < 0.01$; *** $p < 0.001$)

IRM fonctionnelle et neurostimulation

La possibilité d'induire des effets prolongés par rTUS nous a encouragé à chercher à imager l'activité cérébrale après stimulation, par IRM fonctionnelle. L'IRM fonctionnelle calcule la corrélation entre l'activité de différentes zones, permettant ainsi de distinguer quelles régions sont connectées entre elles. Comme il faut typiquement 1 à 2h pour réaliser une telle étude sur le primate, nous avons porté à 40s la durée de stimulation rTUS. Nous avons ici stimulé par ultrasons à basse fréquence (200 kHz) le cortex préfrontal au niveau de la preSMA, puis étudié l'évolution de la connectivité des différentes aires cérébrales par rapport à la preSMA entre la séance sans stimulation ('base-

line') et avec stimulation ('preSMA stim'). Les résultats sont affichés sous forme de carte sur la figure 8.7: à gauche, sont indiquées en rouge les régions dont la connectivité avec la preSMA est accrue après la stimulation et à droite en bleu, les régions où la connectivité avec la preSMA a diminué. L'IRM fonctionnelle montre ici que certaines régions du cerveau ont une activité significativement plus corrélée à la zone stimulée, en moyenne pendant la durée de l'imagerie, démontrant ainsi l'effet long-terme de la stimulation répétée. Ces résultats préliminaires pourraient avoir des répercussions importantes en neurosciences, montrant la possibilité de modifier hors ligne la connectivité cérébrale par ultrasons focalisés tout en imageant l'impact correspondant à l'échelle du cerveau entier par IRM, dans un environnement sans ultrasons.

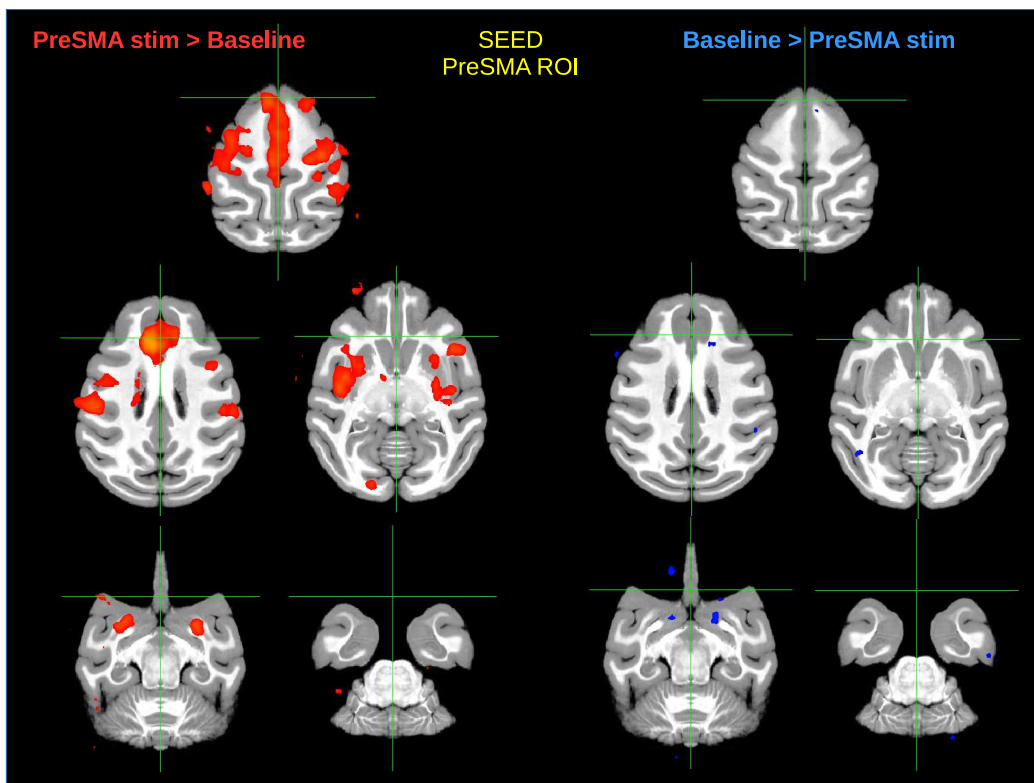


Figure 8.7: Les tâches rouges et bleues représentent les régions où la connectivité relative à la preSMA est plus élevée ou plus faible, respectivement, après la stimulation ultrasonore de la preSMA comparée à la baseline.

Neuromodulation induite par GABA chez le primate non-humain

Nous avons cherché à étendre le spectre des interactions potentielles des ultrasons avec l'activité cérébrale en combinant les ultrasons avec l'injection d'un agent neuromodulateur, dont l'entrée dans le cerveau se fait grâce à l'ouverture de la barrière hémato-encéphalique (BHE). Cette barrière naturelle est formée par les cellules endothéliales du réseau cardiovasculaire dans le cerveau: leurs jonctions étanches permettent uniquement le passage de molécules lipophiles de taille inférieure à 400-500 Da par diffusion passive, ainsi que le passage sélectif d'éléments indispensables au fonctionnement du cerveau comme le glucose et les acides aminés. La BHE, ayant pour fonction de bloquer les agents neurotoxiques et les virus, empêchent également le passage de la plupart des médicaments et agents neuromodulateurs dans le cerveau. Des solutions chimiques ont été développées (lipophilisation ou recherche de molécules ressemblant au glucose) mais elles ne sont pas applicables systématiquement. Une autre approche consiste à lever temporairement la BHE afin de permettre le passage de molécules lipophobes ou de grande taille, ce qui est possible par injection de protéines particulières (agents inflammatoires, certaines hormones et neurotransmetteurs) ou d'une solution hypertonique. Cependant, tant les solutions chimiques que la levée de BHE induisent une assimilation de la molécule généralisée dans tout le cerveau, posant d'éventuels problèmes de sécurité et empêchant le ciblage d'une région particulière du cerveau.

Les ultrasons focalisés, couplés à l'injection intraveineuse d'agents de contraste ultrasonore (ACU), constituent une technique relativement récente permettant l'ouverture non-invasive, ciblée et temporaire de la BHE [105, 159]. Les ACU sont des microbulles de gaz qui, sous l'action des ultrasons, oscillent dans les vaisseaux sanguins du cerveau et entraînent la rupture des jonctions des cellules endothéliales. Avec un transducteur mono-élément à 245 kHz, nous avons ainsi fait parvenir un neurotransmetteur inhibiteur, l'acide γ -Aminobutyrique (GABA), dans le cortex visuel V1 de primates non-humains anesthésiés. La réponse harmonique des microbulles était contrôlée en temps réel: l'expression de la sous-harmonique, qui caractérise l'oscillation non-linéaire stable des microbulles, est un indicateur d'efficacité tandis que le niveau de bruit large bande, symptôme de cavitation inertielle et donc d'implosion des bulles, est à surveiller pour éviter des lésions tissulaires. L'inhibition des neurones de cette région a été mesurée à partir de la réponse visuelle à des

stimuli lumineux en champ complet. Des acquisitions IRM ont également confirmé l'ouverture de la BHE dans V1.

La réponse visuelle aux PEV a été enregistrée sous plusieurs conditions afin de distinguer les différents facteurs d'inhibition: condition de référence (avant toute procédure), après ultrasons seuls envoyés dans V1, après ouverture de BHE (ultrasons couplés à l'injection d'ACU), et enfin après ouverture de BHE et injection de GABA. L'effet inhibiteur du GABA apparaît comme nettement prédominant, cependant les ultrasons seuls et l'ouverture de BHE ont également un effet neuromodulateur. Les mécanismes à l'oeuvre semblent différents selon les cas, car leurs effets interviennent en décalé après l'apparition du stimulus: le GABA inhibe particulièrement la réponse primaire (entre 0 et 100 ms après le stimulus) tandis que les ultrasons seuls et les ultrasons + ACU influent plutôt sur les boucles de réponse, plus de 100ms après l'apparition du flash lumineux (figure 8.8).

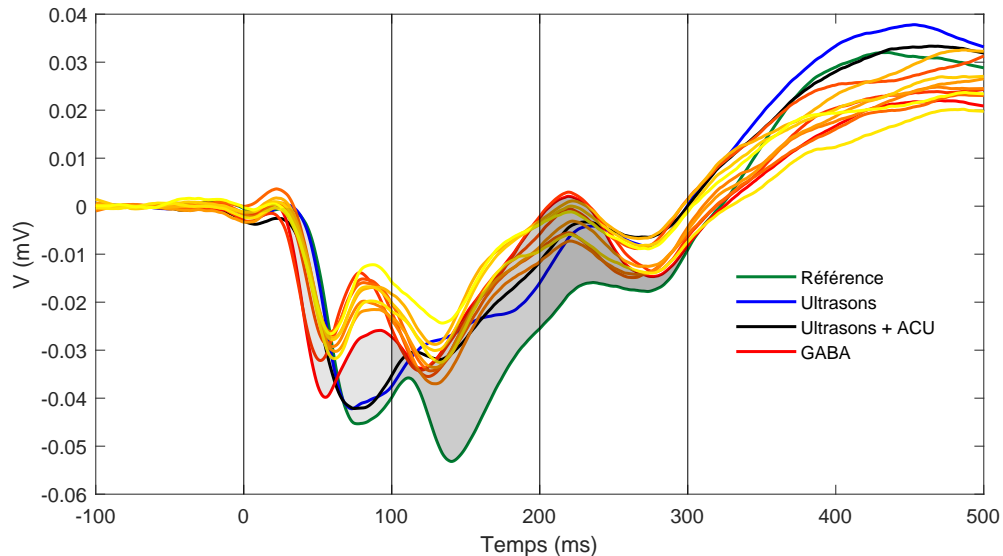


Figure 8.8: Moyenne des réponses visuelles aux différents instants de la session: référence (vert), ultrasons seuls (bleu), ultrasons + ACU (noir), ouverture de BHE et injection de GABA (rouge à jaune). Chaque courbe est la moyenne des 200 réponses visuelles constituant un bloc. Les différentes courbes "GABA" représentent les blocs successifs après l'injection du GABA, chacun durant environ 5 mn. Le stimulus visuel apparaît au temps 0. La quantification de l'inhibition se base sur l'amplitude du premier pic négatif et le calcul de l'aire sous chaque courbe et la référence sur une plage de temps donné (par exemple, les zones grisées représentent l'inhibition de "GABA 1" (en rouge) par rapport à la référence sur les plages 0-100ms, 100-200ms et 200-300ms).

Le GABA n'ayant jamais été administré de cette manière à un primate auparavant, une étude de dose a également été réalisée: les doses de GABA ont été progressivement augmentées de 1 mg/kg à 6 mg/kg. Les effets augmentent linéairement jusqu'à 6 mg/kg (figure 8.9).

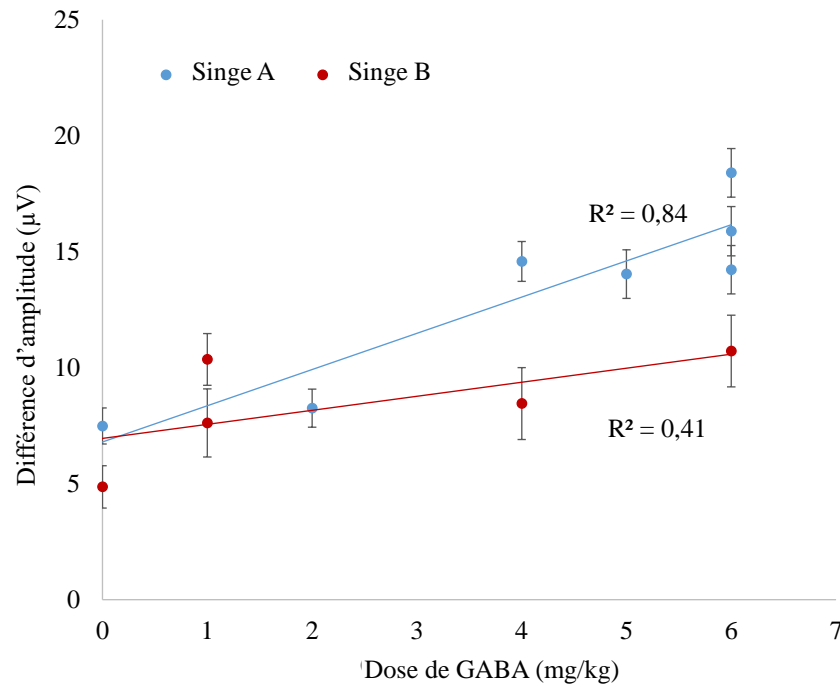


Figure 8.9: Décroissance de l'amplitude des réponses visuelles après injection de GABA, en fonction de la dose de GABA.

Nous avons ici démontré la possibilité d'une neuromodulation durable et forte par l'action combinée des ultrasons, de microbulles et d'un agent neuro-actif. Cette technique contrôlable en temps réel et facile à mettre en place ouvre la voie à des traitements neurologiques non-invasifs, ciblés, sûrs. Elle offre également la possibilité d'étudier fonctionnellement le cerveau par l'inhibition de régions spécifiques, grâce à un ciblage précis, modulable par l'application des ultrasons, et capable d'atteindre des zones profondes du cerveau.

Conclusion

L'objectif général de ce manuscrit était d'étudier le potentiel des ultrasons focalisés pour la neuromodulation. Les deux principaux axes de cette thèse étaient: premièrement, l'optimisation des paramètres ultrasonores, et deuxièmement, le développement de nouvelles techniques pour l'étude de la connectivité cérébrale. Les simulations numériques donnent la distribution du champ de pression dans le cerveau, et donc l'amplitude de pression et la forme d'éventuelles interférences à différentes fréquences, pour chaque modèle animal. Cela s'est avéré utile pour choisir les meilleurs paramètres (fréquence, puissance) pour chaque étude. L'estimation de l'élévation de température permet ensuite de régler la durée de la stimulation et le rapport cyclique afin de ne pas provoquer de lésions ou induire d'éventuels effets thermiques sur les neurones. Les résultats numériques montrent ici que dans des études précédentes réalisées par d'autres groupes de recherche, la variation de température a pu s'approcher dangereusement du seuil de lésion dans le cerveau, soulignant l'importance d'une surveillance systématique de cet effet. Les simulations sur rat et sur singes ont prouvé l'influence de la géométrie du crâne sur la propagation de l'onde: la considération de l'épaisseur du crâne ou de l'espèce animale seulement ne suffit pas à prédire le champ de pression. Ici, les phénomènes complexes d'interférences dans l'os et dans la cavité formée par le crâne ont été pris en considération numériquement.

L'expérimentation sur singes a permis de développer des méthodes d'amélioration des performances de la neuromodulation ultrasonore et de la compréhension du mécanisme physiologique sous-jacent. Tout d'abord, l'enregistrement direct de l'activité d'un neurone pendant une stimulation ultrasonore chez le singe éveillé est un pas en avant pour l'étude de l'effet des ultrasons sur les neurones. Ensuite, les essais de neurostimulation ultrasonore répétée se sont révélés concluants: une perturbation significative de l'activité a été mesurée jusqu'à 25 minutes après la stimulation chez le primate non humain, contre quelques centaines de millisecondes dans les études précédentes. Ce travail a été poursuivi par une stimulation non invasive suivie par IRM fonctionnel de l'activité cérébrale dans un environnement sans ultrasons. Enfin, les derniers travaux sur le couplage entre ultrasons et injection d'agent inhibiteur par ouverture de la barrière hémato-encéphalique mettent en évidence le potentiel de la neuromodulation non invasive et durable d'une région spécifique du cerveau avec l'efficacité d'un neurotransmetteur. La neuromodulation localisée et non invasive, avec ou sans agent neuroactif, combinée avec l'imagerie non invasive du cerveau entier, ouvre de

nouvelles opportunités dans l'étude de la connectivité cérébrale.

De nombreuses suites de projet peuvent être envisagées, basées sur le travail présenté ici. Nos travaux sur l'IRM fonctionnel hors ligne après neuromodulation ultrasonore pourront être continués pour étudier la connectivité à long-terme dans le cerveau entier de n'importe quel modèle animal et potentiellement de l'humain. Par ailleurs, une nouvelle technique développée au laboratoire, l'imagerie fonctionnelle par ultrasons, a fourni des cartes de l'activité cérébrale chez le rongeur avec une grande précision spatiale et temporelle. La neurostimulation ultrasonore combinée avec l'imagerie fonctionnelle par ultrasons pourra donner de précieuses informations sur les effets de neuromodulation au niveau cortical et sous-cortical. Enfin, la spécificité des effets des ultrasons en fonction du rapport cyclique sur les différents types de neurones pourra être exploitée pour activer sélectivement un type de cellule donné. La sélectivité pourrait être poussée encore plus loin grâce à la délivrance, par ouverture de barrière hémato-encéphalique, de molécules amenées à se fixer sur des récepteurs spécifiques. Les propriétés non-invasives, réversibles et locales de l'ouverture de BHE par ultrasons, combinées aux techniques d'imagerie, de biologie moléculaire et de la génétique pourraient ainsi mener à un large champ d'applications non seulement dans le domaine biomédical mais aussi en recherche en neurosciences.

Scientific output

Publications in peer-reviewed journals

Published

C. Constans, T. Deffieux, P. Pouget, M. Tanter, J-F. Aubry. **A 200 - 1380 kHz Quadrifrequency Focused Ultrasound Transducer For Neurostimulation In Rodents And Primates: Transcranial In Vitro Calibration And Numerical Study Of The Influence Of Skull Cavity.** *IEEE Transactions on Ultrasonics, Ferroelectrics, and Frequency Control*. 2017.

N. Wattiez, C. Constans, T. Deffieux, P.M. Daye, M. Tanter, J-F. Aubry, P. Pouget. **Transcranial ultrasonic stimulation modulates single-neuron discharge in macaques performing an antisaccade task.** *Brain Stimulation*. 2017.

C. Constans, P. Mateo, M. Tanter, J-F. Aubry. **Potential impact of thermal effects during ultrasonic neurostimulation: retrospective numerical estimation of temperature elevation in seven rodent setups.** *Physics in Medicine & Biology*. 2018.

Submitted

C. Constans, H. Ahnine, M. Santin, S. Lehericy, M. Tanter, P. Pouget, J-F. Aubry. **Non-invasive ultrasonic modulation of visual evoked response by GABA delivery through the blood brain barrier.** *In review, eLife*.

H. Ahnine, C. Constans, N. Wattiez, M. Tanter, J-F. Aubry and P. Pouget. **Sustained modulation of antisaccade latencies by repetitive focused transcranial ultrasound stimulation of frontal cortex in non-human primates.** *In review, Brain Stimulation*.

L. Verhagen, C. Gallea, D. Folloni, C. Constans, D. Jensen, H. Ahnine, M. Santin, S. Lehericy, B. Ahmed, M. Klein-Flugge, K. Krug, R. Mars, M. Rushworth, P. Pouget, J-F Aubry, J. Sallet. **Offline impact of transcranial focused ultrasound on cortical activation in macaques.** *In review, eLife.*

D. Folloni, L. Verhagen, R. Mars, E. Fouragnan, C. Constans, J-F Aubry, M. Rushworth, J. Sallet. **Manipulation of subcortical and deep cortical activity in the primate brain using transcranial focused ultrasound stimulation.** *In review, Neuron.*

Z. Csaba , T. Vitalis , C. Charriaud-Marlangue , I. Margaille , B. Coqueran , P-L. Leger , I. Parente , L. Titomanlio , C. Constans , M. Santin , S. Lehericy , C. Demene , S. AUVIN , M. Tanter , J-F. Aubry , P. Gressens **A novel, simple and highly sensitive approach for detection of blood-brain barrier permeability using ligand-induced G protein-coupled receptor internalization.** *Submitted, Nature Communications.*

Presentations

C. Constans*, T. Deffieux, M. Tanter, J-F. Aubry. **A 200kHz-1380kHz multifrequency focused ultrasound transducer for neuromodulation in rodents: numerical study and transcranial in-vitro calibration.** *Oral presentation, ISTU 2016, Tel Aviv, Israel.*

C. Constans*, T. Deffieux, N. Wattiez, P. Pouget, M. Tanter, J-F. Aubry. **Multifrequency focused ultrasound transducer for neurostimulation in rodents and primates** *Poster presentation, IEEE IUS 2016, Tours, France.*

C. Constans*, M. Tanter, J-F. Aubry. **Estimation of thermal rise during ultrasonic neuro-modulation in rodents: retrospective analysis of five recent studies** *Poster presentation, ISTU 2017, Nanjing, China.*

H. Ahnine, C. Constans*, N. Wattiez, M. Tanter, J-F. Aubry, P. Pouget. **Long-lasting modulation of visuomotor activity by repetitive focused ultrasound stimulation of frontal cortex** *Oral presentation, ISTU 2018, Nashville, USA.*

C. Constans*, P. Mateo, M. Tanter, J-F. Aubry. **Thermal rise during ultrasonic neurostim-**

ulation: retrospective numerical estimation in seven published rodent setups and ex vivo measurements *Poster presentation, ISTU 2018, Nashville, USA.*

Devant l'impact des maladies neurodégénératives sur la société, les thérapies par ultrasons focalisés apparaissent comme des techniques prometteuses combinant non invasivité, précision spatiale millimétrique et capacité d'atteindre les structures profondes du cerveau. Cependant, des travaux sont encore nécessaires pour renforcer les effets de la neuromodulation, comprendre les mécanismes sous-jacents et contrôler la sûreté de la technique avant d'entreprendre des essais cliniques. Dans cette thèse, la propagation des ultrasons dans le cerveau de rongeurs et de singes a été étudiée numériquement afin d'estimer l'intensité acoustique dans le cerveau, la répartition spatiale des ondes dans la boîte crânienne et l'élévation de température. Afin d'évaluer physiologiquement les effets des ultrasons à l'échelle cellulaire, l'activité de neurones uniques a été mesurée sur des macaques éveillés pendant une neuromodulation ultrasonore. Puis, la durée de l'effet de modulation a été augmentée grâce à une prolongation du tir sur des singes exécutant une tâche visuelle. L'imagerie fonctionnelle par IRM a ensuite permis de faire ressortir des changements de connectivité entre l'aire stimulée et des régions du cerveau éloignées. Enfin, les avantages de la neurostimulation par ultrasons ont été combinés avec l'efficacité d'un agent neuroactif. En utilisant des microbulles conjointement aux ultrasons, la barrière hémato-encéphalique a été ouverte localement et réversiblement dans le cortex visuel de macaques anesthésiés pour permettre le passage d'un neurotransmetteur inhibiteur dans le cerveau. La baisse d'amplitude des réponses EEG du cortex visuel à des stimuli démontre la faisabilité de la délivrance locale et non invasive de neuromodulateurs dans le cerveau. Ainsi, les paramètres ultrasonores ont été optimisés grâce aux simulations numériques et à des expériences *in vivo* pour renforcer les effets de neuromodulation tout en contrôlant les effets indésirables, avec l'objectif de se diriger vers des applications thérapeutiques et proposer de nouveaux outils pour des études de connectivité cérébrale.

Considering the extent of neurodegenerative diseases consequences on the society, focused ultrasound appears as a promising technique combining non-invasiveness, millimetric spatial accuracy and ability to reach deep brain structures. However, efforts still need to be made to amplify the effects of focused ultrasound neuromodulation, understand its mechanism and control the safety of the technique before moving towards human trials. The ultrasound propagation inside the brain of rodents and monkeys was first studied numerically to estimate the maximum intensity in the brain, the pressure distribution in the skull cavity and the thermal rise. To evaluate physiologically the ultrasound effects at the cellular level, the activity of individual neurons was measured on awake macaques during ultrasonic neuromodulation. To further increase the duration of the modulation, a longer sonication was tested successfully on macaques performing a visual task. Functional MRI was then used to highlight the connectivity changes between the stimulated area and distant cerebral regions. Finally, the advantages of ultrasound neurostimulation were combined with the efficiency of a neuroactive agent (GABA). Using microbubbles and ultrasound, the blood brain barrier was opened locally and reversibly in the visual cortex of anesthetized macaques to deliver an inhibitory neurotransmitter in the brain. The amplitude of the EEG response of the visual cortex to stimuli decreased after GABA injection, demonstrating the feasibility of delivering neuroactive drugs non-invasively and locally to any brain region. Overall, ultrasound parameters were optimized with both numerical tools and *in vivo* experiments to amplify neuromodulation effects while controlling the safety. This work opens the way to the development of novel therapeutic applications and new tools for connectivity studies.